Master's Thesis

Computational modeling approach for determining the bending strength of glued laminated timber beams taking into account knot groups and quasi-brittle material failure

submitted in satisfaction of the requirements for the degree of

Diplom-Ingenieur

of the TU Wien, Faculty of Civil Engineering

Diplomarbeit

Computergestützter Modellierungsansatz zur Bestimmung der Biegefestigkeit von Brettschichtholzträgern unter Berücksichtigung von Astgruppen und quasi-sprödem Materialversagen

ausgeführt zum Zwecke der Erlangung des akademischen Grades eines

Diplom-Ingenieurs

eingereicht an der Technischen Universität Wien, Fakultät für Bauingenieurwesen

von

Christoffer Vida, BSc

Matr.Nr.: 01228926

unter der Anleitung von

Univ.Ass. Dipl.-Ing. Dr.techn. **Markus Lukacevic**

Univ.Ass. Dipl.-Ing. **Sebastian Pech**, BSc

Associate Prof. Dipl.-Ing. Dr.techn. **Josef Füssl**

Institut für Mechanik der Werkstoffe und Strukturen
Forschungsbereich für Werkstoff- und Struktursimulation (FB 202-02)
Technische Universität Wien
Karlsplatz 13/202, 1040 Wien, Österreich

Wien, im September 2020

Danksagung

Mein Dank richtet sich an all jene Personen, die mich während meines Studiums und des Abfassens meiner Diplomarbeit unterstützt haben. Besonders bedanke ich mich bei allen Betreuern meiner Diplomarbeit für die fachliche Heranführung an nicht-lineare computergestütze Berechnungsmodelle, die für mich sehr lehrreichen Diskussionen sowie für ihr herausragendes Engagement bei der Betreuung.

Im Speziellen bedanke ich mich bei Herrn Univ.Ass. Dipl.-Ing. Dr.techn. Markus Lukacevic für seine konstruktiven Anmerkungen und sorgfältigen Korrekturen in der Ausarbeitungsphase. Bei Herrn Univ.Ass. Dipl.-Ing. Sebastian Pech, BSc bedanke ich mich für seine Unterstützung bei der Umsetzung von Programmierungen. Herrn Associate Prof. Dipl.-Ing. Dr.techn. Josef Füssl danke ich für die Möglichkeit meine Diplomarbeit am Forschungsbereich für Werkstoff- und Struktursimulation abzufassen und mich auch weiterhin an der Forschung in diesem Bereich am Institut für Mechanik der Werkstoffe und Strukturen (IMWS) beteiligen zu können. Die Zusammenarbeit hat mir stets Freude bereitet und steigerte mein Wissen in diesem Themengebiet maßgebend.

Bei Herrn Univ.Prof. Dipl.-Ing. Dr.techn. Bernhard Pichler bedanke ich mich für die bereits im Bachelorstudium ermöglichten ersten Einblicke in Forschung und Lehre am IMWS sowie für die Unterstützung im weiteren Studium.

Herrn Assistant Prof. Dipl.-Ing. Dr.techn. Christian Schranz, MSc danke ich für meine Aufnahme während des Studiums im EDV-Labor Bauingenieurwesen und herzlichst für seine Begleitung als Mentor.

Während meiner Studienzeit entwickelten sich zu Kommilitoninnen und Kommilitonen neue und festigten sich bereits bestehende Freundschaften, für eure Freundschaft und euren Rückhalt bin ich euch sehr dankbar.

An meine Familie, im Besonderen an meine Mutter Ingrid, richte ich meinen herzlichen Dank für ihre immerwährende Unterstützung und Motivation. Kiitän rakasta Matildaani koko sydämestäni hänen avustaan ja tuestaan.

Abstract

The mechanical behavior of glued laminated timber (GLT) beams strongly depends on natural growth characteristics of wood. For this reason, the wooden boards are sorted according to strength classes before the beams are manufactured. Sorting is mainly based on morphology data of knots, which nowadays is gained by laser scanning exploiting the tracheid effect. Then, in accordance with current standards, each board is assigned a strength grade. However, the further manufacturing process does not take into account the detailed information about the morphology of knots. Current standards regulate the assembly of the sorted boards to beams, where length limitations are overcome by finger-jointing the individual boards, resulting in continuous lamellas. The obtained beams are then assigned a strength class, regardless of the location of the weak points, such as knots and finger joints.

Current research focuses on exploiting this detailed morphology data. An automated three-dimensional reconstruction process uses the data of the individual boards to successfully determine the position and orientation of the knots. The modeled knots in combination with a reconstructed fiber course are the basis to derive individual stiffness profiles. The morphology data are else used as basis for selected indicating parameters (IPs) for the derivation of strength profiles. In a previous study, laser-scanned boards were processed into GLT beams, covering three beam sizes and two strength classes. The use of boards without finger joints ensured the focus on knots as weak points. The beams with well-known knot morphology were subjected to static four-point bending tests until failure, some of which showed non-linear behavior in the load-displacement curve. This motivated the development of an approach to model failure mechanisms.

In this thesis, a computational modeling approach is developed to determine the bending strength as well as failure mechanisms of GLT beams. The approach considers the knot morphology with section-wise constant effective material properties from the stiffness and strength profiles without using a predefined grid. Stress and strain fields are accessed by using a linear elastic material model within the framework of the non-linear finite element method (FEM). The description of vertical cracks is realized with the use of the extended finite element method (XFEM). Horizontal cracks are implemented in a simplified way as delamination between adjacent timber boards. This allows horizontal crack propagation and the merging of two vertical cracks with a horizontal distance in adjacent boards. Without this implementation the predicted load-bearing capacity would be overestimated. Delamination, introduced to describe horizontal cracking in a simplified way, is not intended to depict failure in the adhesive joint and, therefore, does not use material properties of an adhesive. For both cracking mechanisms (orientations) modified traction-separation laws are used to model quasi-brittle material failure. Global failure will occur after a defined load drop in the load-displacement curve, where additionally the compliance with two energy criteria is necessary. This approach covers a nonlinear load-displacement curve and progressive failure.

The computational modeling approach is able to determine both the bending strength and failure mechanisms in a reliable way. Simulation accuracy was found to be sufficient by using three finite elements per board height. With two different beam sizes, the so-called size effect could be successfully covered for both strength classes of GLT beams. The experimentally observed positions of fracture in the outermost board on the tensile side could be successfully predicted by simulations in more than 75 % of the beams.

Kurzfassung

Das mechanische Verhalten von Brettschichtholzträgern (BSH-Trägern) hängt stark von den natürlichen Wachstumseigenschaften von Holz ab. Aus diesem Grund werden die Holzbretter vor der Trägerherstellung nach Festigkeitsklassen sortiert. Die Sortierung basiert hauptsächlich auf Morphologiedaten von Ästen, die heutzutage durch Laserscanning unter Ausnutzung des Tracheid-Effekts gewonnen werden. Anschließend wird in Übereinstimmung mit den aktuellen Normen jedem Brett eine Festigkeitsklasse zugewiesen. Der weitere Herstellungsprozess berücksichtigt jedoch nicht die detaillierten Informationen über die Morphologie von Ästen. Aktuelle Normen regeln die Zusammensetzung der sortierten Bretter zu Trägern, wobei Längenbegrenzungen durch Keilzinkenverbindungen der einzelnen Bretter und die dadurch entstehenden durchgehenden Lamellen überwunden werden. Die erhaltenen Träger sind anschließend einer Festigkeitsklasse zugeordnet, unabhängig von der Lage der Schwachstellen, wie etwa Ästen und Keilzinkenverbindungen.

Die aktuelle Forschung konzentriert sich auf die Nutzung dieser detaillierten Morphologiedaten. Ein automatisierter dreidimensionaler Rekonstruktionsprozess verwendet die Daten der einzelnen Bretter, um erfolgreich Position und Orientierung der Äste zu bestimmen. Die modellierten Äste in Verbindung mit einem rekonstruierten Faserverlauf bilden die Grundlage zur Ableitung individueller Steifigkeitsprofile. Die Morphologiedaten dienen weiter als Grundlage für ausgewählte Sortierparameter zur Ableitung von Festigkeitsprofilen. In einer früheren Studie wurden die laser-gescannten Bretter zu BSH-Trägern verarbeitet, wobei drei Trägergrößen und zwei Festigkeitsklassen abgedeckt wurden. Die Verwendung von Brettern ohne Keilzinkenverbindungen sicherte die Fokussierung auf Äste als Schwachstellen. Die Träger mit bekannter Astmorphologie wurden statischen Vier-Punkt-Biegeversuchen bis zum Versagen unterzogen, bei dem einige ein nichtlineares Verhalten in der Last-Verschiebungskurve zeigten. Dies motivierte die Entwicklung von einem Rechenmodell zur Modellierung von Versagensmechanismen.

In dieser Arbeit wird ein computergestützter Modellierungsansatz entwickelt, um sowohl die Biegefestigkeit als auch die Versagensmechanismen von BSH-Trägern zu bestimmen. Der Ansatz berücksichtigt die Astmorphologie mit abschnittsweise konstanten effektiven Materialeigenschaften mittels den Steifigkeits- und Festigkeitsprofilen ohne Verwendung eines vordefinierten Rasters. Spannungs- und Dehnungsfelder werden durch die Verwendung eines linear elastischen Materialmodells im Rahmen der nichtlinearen Finite-Elemente-Methode (*finite element method* FEM) beschrieben. Die Beschreibung von vertikalen Rissen wird mit der Anwendung der erweiterten Finite-Elemente-Methode (*extended finite element method* XFEM) realisiert. Horizontale Risse werden auf vereinfachte Weise als Delamination zwischen benachbarten Holzbrettern implementiert. Dies ermöglicht eine horizontale Rissausbreitung und die Vereinigung von zwei vertikalen Rissen mit einem horizontalen Abstand in benachbarten Brettern. Ohne diese Implementierung würde die prognostizierte Traglast überschätzt werden. Die Delamination, die zur vereinfachten Beschreibung von horizontalen Rissen eingeführt wurde, soll kein Versagen in der Klebefuge darstellen und verwendet daher nicht die Materialeigenschaften eines Klebstoffs. Für beide Rissmechanismen (bzw. -orientierungen) werden modifizierte Spannungs-Separations-Gesetze (*modified traction-separation laws*) verwendet, um ein quasi-sprödes Materialversagen zu modellieren. Das globale Versagen tritt nach einem definierten Abfall der Belastung in der Last-Verschiebungskurve

ein, wobei zusätzlich die Einhaltung von zwei Energie-Kriterien notwendig ist. Dieser Ansatz bildet eine nichtlineare Last-Verschiebungskurve und progressives Versagen ab.

Der computergestützte Modellierungsansatz ist in der Lage, sowohl die Biegefestigkeit als auch Versagensmechanismen auf zuverlässige Art und Weise zu bestimmen. Die Simulationsgenauigkeit erwies sich bei Verwendung von drei finiten Elementen pro Bretthöhe als ausreichend. Bei zwei verschiedenen Trägergrößen konnte der sogenannte Größeneffekt erfolgreich für zwei Festigkeitsklassen von BSH-Trägern abgedeckt werden. Die experimentell beobachteten Bruchpositionen im äußersten Brett auf der Zugseite konnten durch Simulationen bei mehr als 75 % der Träger erfolgreich prognostiziert werden.

Contents

Chapter 1

Introduction

GLT beams even further advance the excellent mechanical properties of timber and overcome restrictions in regard to dimension with requirements regulated by DIN EN 14080:2013-09 [14]. The superiority of timber over other commonly used building materials is demonstrated by a comparison of the ratio of mechanical properties to mass, where the timber properties are considered in fiber direction. For example, the characteristic strength-to-mass ratio for timber is more than four times better than for steel and about five times better than for concrete in regard to tensile and compressive strength, respectively. The mean stiffness-to-mass ratio of timber is even ten and twenty times better than that of steel and concrete, respectively. However, the natural growth process of timber leads to a quite sophisticated morphological structure that causes also a rather sophisticated mechanical behavior. The assembly of timber boards to GLT beams creates indeed a homogenization on a large scale but still keeps the sophisticated morphology on a small scale and introduces further relations between the timber boards. Nevertheless, failure is related mainly to two aspects: the allocation of knots and weakening due to finger joints. With a better understanding of the mechanical mechanisms a much better prediction of the load-bearing capacity is to be expected.

A large number of studies can be found in literature that investigate the load-bearing capacity and failure mechanisms of GLT beams subjected to four-point bending tests. Conceptually, researchers pursued two approaches: conducting experimental studies that cover a significant sample size or applying a developed computational simulation model that is verified with experiments. The latter requires a significantly lower number of real experiments while at the same time increasing easily the number of results through computational simulations.

In the 1990s numerous experimental studies [54, 12, 20, 30, 29, 55] were conducted to examine the empirical relation between the characteristic tensile strength of individual timber boards and the resulting characteristic bending strength of the whole beam. A description and comparison of those results can be found in Brandner and Schickhofer [7]. Over time, exclusively experimental investigations to derive such empirical models became rare. The reasons for this are the great effort involved in manufacturing and testing a sufficient sample size of GLT beams, possible testing limitations regarding beam dimensions, and the inability of experimental studies to distinguish mechanical from stochastic effects. However, the transition was only possible due to the ongoing development of computational simulation models that allow effective analysis of a wide range of GLT beam configurations. Selected simulation models are briefly described in the following paragraphs.

Already in 1980 Foschi and Barrett [25] proposed a simulation model for GLT beams in conjunction with stochastic methods. The model divided all used timber boards into 15 cm long cells and assigned them an individual clear wood density and knot size. Subsequently, in correlation to those, the modulus of elasticity and tensile strength of each cell were determined and assigned. Consideration of the finger joints, which connected the individual timber board sections, was not implemented. The determination of the predicted load-bearing capacity assumed brittle failure that was realized with a weakest link failure criterion, thus the simulation was

completed when the first tensile strength was reached. The study used a finite element (FE) approach with linear elastic material behavior to analyze the beam strength and stiffness, with a Monte Carlo simulation being used to gain probability distributions.

The so-called *Prolam model* was proposed by Hernandez et al. [34] as a further development of the model from Bender et al. [4]. The model consisted of GLT beams built up with finger-jointed timber boards. The modulus of elasticity and the tensile strength were assigned in 61 cm long cells in accordance to the model proposed by Taylor and Bender [61]. Unlike the previous model the material properties were simulated directly instead of modifying clear wood properties due to knot characteristics. The finger joint modulus of elasticity as well as tensile strength were considered in accordance to the models developed by Burk and Bender [9]. The model used the transformed section method that determined for each transformed cross section the ultimate moment-carrying capacity in accordance to its weakest timber board. The model considered progressive failures and therefore allowed individual timber boards or finger joints to fail until the GLT beam reached its ultimate capacity.

The so-called *Karlsruher calculation model* was originally proposed by Ehlbeck et al. [17, 18, 19] and further developed by Colling [11] or more recently by Frese [26] and Blaß et al. [6]. The model is quite similar to the presented model from Foschi and Barrett [25]. The timber boards were also divided into 15 cm cells with assigned dry density and tKAR (total knot-area-ratio) values. Timber board parts had individual constant dry densities and allocated knots in accordance to [32], which were finger-jointed together to lamellas. Both parameters were assigned in accordance to a modified beta distribution. Based on those assignments the modulus of elasticity, tensile, and compression strength were defined for the timber board cells and finger joints in accordance to models of Glos [31] and Ehlbeck et al. [17]. The used material model applied orthotropic properties with linear elastic behavior in areas of tension and linear elastic and ideal plastic behavior in areas of compression. The analysis was realized with an FE model that determined the load-bearing capacity when the first finite element reached the tensile strength in the outermost lamella of the beam, for all other lamellas progressing failure was allowed. Based on such a model empirical relations between the characteristic tensile strength of lamellas and resulting characteristic bending strength of the beam were established [27, 28].

Fink [21] proposed a GLT beam model that consisted of finger-jointed timber boards, which were subdivided into clear wood and weak sections of 15 cm length. The distance between weak sections, the tKAR value, and dynamic modulus of elasticity are determined in accordance to a shifted gamma, a truncated log-normal, and a log-normal distribution, respectively. A linear regression model with an error term determined the material properties, which are further used to derive the finger joint properties. The modulus of elasticity for finger joints was chosen as the mean value of the two adjacent clear wood sections and the finger joint tensile strength was equal to a weak section with a fictive tKAR value from 0.2 to 0.3. For the beam's material model isotropic and linear elastic behavior was chosen. The FE model used a finite element height corresponding to the timber board thickness. Progressive failure was considered with an iterative scheme: When the tensile strength in one finite element was reached, the element's stiffness was set to zero and the analysis was repeated. For each iteration the bending strength and the bending stiffness of the GLT beam were evaluated. Global failure of the beam was reached when the bending stiffness decreased by 1 %, compared to the first iteration. In order to account for the error term of the material properties a Monte Carlo simulation of one GLT beam was performed and the mean values gave the final results. The predicted final results were the bending strength as the maximum bending strength of all iterations, the system bending stiffness as bending stiffness of the first iteration, and the type of failure in the last increment, which could either be failure in a clear wood, a weak section, or failure of a finger joint. A peculiarity was the validation of the model with an experimental study on GLT beams with well-known

knot morphology, where the error term was covered with 100 realizations of each beam. A total of 24 beams were tested, which had all the same size and corresponded to two strength classes.

The previous model was expanded by Blank et al. [5] to consider quasi-brittle material behavior with a linear softening law. The softening law was used for the timber boards as well as the finger joints with a constant fracture energy of $10 \, \mathrm{N \, mm/mm^2}$. The finite element height was unchanged and corresponded to the timber board thickness. For different beam sizes, this model led to more accurate predictions of their bending strength.

Kandler et al. [37] used the information of well-known knot morphology of specific GLT beams to predict their material-related effective modulus of elasticity and compared the results with experimental tests. For the experimental testing the allocation of the timber boards with the well-known knot morphology was traced throughout the whole manufacturing process. A total of 50 beams was tested, having only continuous boards without finger joints. The study included three beam sizes and two strength classes. For the prediction, each timber board had two individual stiffness profiles in length direction, which were derived from either empirical dynamic stiffness measurements or fiber angle data in conjunction with a micromechanical multiscale model. An FE approach predicted on basis of those profiles two material-related effective moduli of elasticity for each beam. Kandler et al. [39] also used the detailed morphology data of the GLT beams to predict the bending strength. On basis of the detailed information the knot geometry was reconstructed in a three-dimensional model to derive individual section-wise constant effective stiffness and strength profiles for each board. An FE modeling approach was proposed that used those material property profiles. Failure was determined by a Tsai-Wu criterion in conjunction with a mean stress approach in accordance to [57]. They successfully predicted the trend and suggested to develop approaches that consider mechanical failure mechanisms.

The previous approach was also extended to a stochastic engineering framework by Kandler et al. [41]. The profiles were analyzed for this purpose to create a random process for stiffness and strength profiles to consider random material fluctuations. Additionally, the failure criterion was adjusted to cover progressive failure in accordance to the implementation in [17, 21]. The present thesis uses the experimental study from [37, 39] (Section 2.1) and the corresponding available data of the stiffness and strength profiles from [41] (Section 2.2).

Another quasi-brittle modeling approach was pursued by Tapia Camú and Aicher [60], who applied XFEM to account for failure within timber boards or failure of finger joints. Both cases of failure were considered with different constant fracture energies. First the timber board parameters were generated, which were modulus of elasticity, tensile strength, compression strength, and length. All parameter values were selected from respective known statistical distributions and the first three parameters considered their cross-correlation. Subsequently, the allocation of the parameters within a board was determined by an autoregressive model in accordance to Kline et al. [43] and Taylor and Bender [61]. The parameters were finally assigned to timber board cells of $10 \, \mathrm{cm}$ length with the inherited cross-correlation. The properties of the finger joints depended on the corresponding timber boards. The fracture energy of the timber boards was chosen to be $10 \, \mathrm{N \, mm/mm^2}$, in accordance to Blank et al. [5]. The fracture energy of finger joints was initially set to $5 \, \mathrm{N \, mm/mm^2}$ [56, 59], which was the result of a conversion from a realistic crack path in the finger joint to a vertical crack. However, appropriate results of the bending strengths were achieved by finally using a fracture energy of finger joints of $25 \, \mathrm{N \, mm/mm^2}$. The predicted load-bearing capacity was reached when the load decreased by $2 \, \%$ in the load displacement diagram. The authors examined three beam sizes with at least 250 simulations each.

None of the presented studies used a quasi-brittle modeling approach with discrete cracks to investigation failure mechanisms of specific reconstructed GLT beams. Fink [21] and Kandler et al. [39] reconstructed GLT beams under consideration of their knot morphology for bending

strength predictions, however, they did not compare the mechanical failure mechanisms to the results of the corresponding experiments (except for the distinction of timber or finger joint failure [21]). Furthermore, all presented modeling approaches used two-dimensional models as simplifications. This is reasonable for the applied studies, however, for future investigations on GLT beams with local reinforcements, when studying the influence of pith locations or for an extension of the model to cross-laminated timber, information about the three-dimensional strain and stress fields is necessary.

This motivates the presented development of a three-dimensional approach that considers failure mechanisms and lays the foundation for future investigations. The approach aims at virtually reconstructing the experimental setup of the study described in Kandler et al. [37] and Kandler et al. [39]. In an effort to clearly link failure mechanisms to the presence of knots and knot groups no finger joints are implemented. A future extension to additionally consider finger joints is easily possible. With this approach GLT beams are assembled under consideration of the well-known knot morphology of each timber board. The section-wise constant effective property profiles of the timber boards were gained from previous research [39, 41] and serve as input to the approach. The allocation of material properties depends entirely on the knot morphology and does not follow a predefined grid pattern.

The modeling approach covers quasi-brittle behavior by considering a fracture process zone with a modified traction-separation law in accordance with non-linear fracture mechanics [5]. The fracture process zone is introduced by vertical discrete cracks that are realized with XFEM. The computational model is realized with the commercial FE software Abaqus 2019 (from Dassault Systèmes, Vélizy-Villacoublay, France) and its implementation of XFEM. This approach associates the used tensile strength with the initiation of vertical discrete cracks. Other crack orientations would require corresponding data about tensile strength and fracture energy, which is not available. Furthermore, the assignment of the fracture energy depending on the crack orientation is not yet implemented in Abaqus. However, this means that vertical cracks could never deviate in horizontal direction even over several lamellas. Also, vertical cracks that occur simultaneously in different lamellas, but which are located at different positions in horizontal direction, could never merge in horizontal direction. Therefore, the delamination of timber boards is additionally allowed by introducing cohesive surface properties in the glue lines with a modified traction-separation law, which finally result in horizontal discrete cracks. It must be emphasized that in this way it is not the glue line itself that should be modeled, but rather the horizontal cracks in lamellas should be taken into account in a simplified way. Therefore, material properties selected later cannot be compared with those of adhesives. Both crack implementations use maximum stress criteria for the initiation and the propagation of a crack, the evolution is then controlled with a constant fracture energy.

The approach uses the non-linear FEM with an incremental-iterative method. Progressive failure is covered by a global failure criterion that determines the predicted load-bearing capacity when the load drops by 3 % in the load-displacement curve. Additionally, the predicted load-bearing capacity needs to obey two energy criteria. The timber board material is described by a linear elastic, orthotropic material model. Last but not least the approach uses a displacement controlled loading that considers the experimental loading setup to distribute the applied displacement with a load distribution construction.

The aim of this work is to develop a computational modeling approach for GLT beams to determine their bending strength as well as mechanical failure mechanisms taking into account knot groups and quasi-brittle material failure and, furthermore, research mesh dependency and parameter sensitivity. To this end the present thesis is structured as follows: Chapter 2 presents the setup and results of an experimental study on GLT beams with well-known knot morphology subjected to a four-point bending test and the method to derive effective material properties

along each used timber board from the available data. Chapter 3 describes the realization of a three-dimensional quasi-brittle FE modeling approach with linear elastic material behavior that considers the well-known knot morphology to cover progressing failure with discrete cracks and is able to reproduce non-linear behavior in the load-displacement relation. Results in regard to mesh size dependency, verification of the modeling approach with mechanical failure mechanisms, and sensitivity of selected material parameters are presented and discussed in Chapter 4. Finally, Chapter 5 contains conclusions and an outlook on future improvements and investigations.

Chapter 2

Previous research on GLT beams with well-known knot morphology

2.1 Experimental study

Kandler et al. [37] and Kandler et al. [39] examined the mechanical behavior of 50 GLT beams that were subjected to a four-point bending test. Five beam types (A/T14-4 corresponds to type A with 4 lamelllas of strength grade T14, B/T22-4, C/T22-7, D/T14-10, and E/T22-10), with ten beams of each type, were tested. The beam types covered three beam sizes and two timber board strength grades that corresponded to strength classes of GLT beams. The used strength grades T14 (LS15) and T22 (LS22) resulted in strength classes GL 24h and GL 30h with homogeneous GLT beam setups, respectively, in accordance to DIN EN 14080:2013-09 [14]. Table 2.1 gives an overview and the measurements of the beam types and Fig. 2.1 illustrates the dimensions of the three beam sizes. In order to examine the mechanical behavior of knot groups, the study used continuous timber boards without finger joints. Thus, the knot groups are the main source of weak points.

The GLT beams were manufactured from timber boards of Norway Spruce, which were delivered by a sawmill from Töreboda, Sweden. The original timber boards had dimensions of 35 mm height, 95 mm width, and 5 400 mm length. The boards were planed from 35 mm to a height of 33 mm, in preparation for the gluing process. After gluing with an MUF adhesive the beams were planed to their final width of 90 mm. The outermost timber boards were oriented such that their pith location would be situated beneath or above the beam, which was in accordance to the Swedish standards of GLT production. Prior to manufacturing, all timber boards were laser scanned and marked with a unique identification number to trace them throughout the manufacturing process that enable the later virtual reconstruction of the beam with its individual

Tab. 2.1: Beam type properties, with charasteristic lamella tensile strength in longitudinal direction $f_{t,0,k}$, beam's bending strength $f_{m,k}$ (both according to DIN EN 14080:2013-09 [14]), number of lamellas n, and notation of beam dimensions are according to Fig. 2.1.

| | Details of the beam type[a] | | | | | Measurements[b] | | | | |
Group	Strength grade	$f_{t,0,k}$ [N/mm²]	Strength class	$f_{m,k}$ [N/mm²]	n	$\ell_{span} = 2\,\ell_2 + \ell_3$ [mm]	ℓ_1 [mm]	ℓ_2 [mm]	ℓ_3 [mm]	h [mm]
A	T14	14.0	GL 24h	24.0	4	2 340	180	780	780	132
B	T22	22.0	GL 30h	30.0	4	2 340	180	780	780	132
C	T22	22.0	GL 30h	30.0	7	4 140	1 260	1 380	1 380	231
D	T14	14.0	GL 24h	24.0	10	5 200	100	1 610	1 980	330
E	T22	22.0	GL 30h	30.0	10	5 200	100	1 610	1 980	330

[a] Each beam type consisted of ten individual beams.
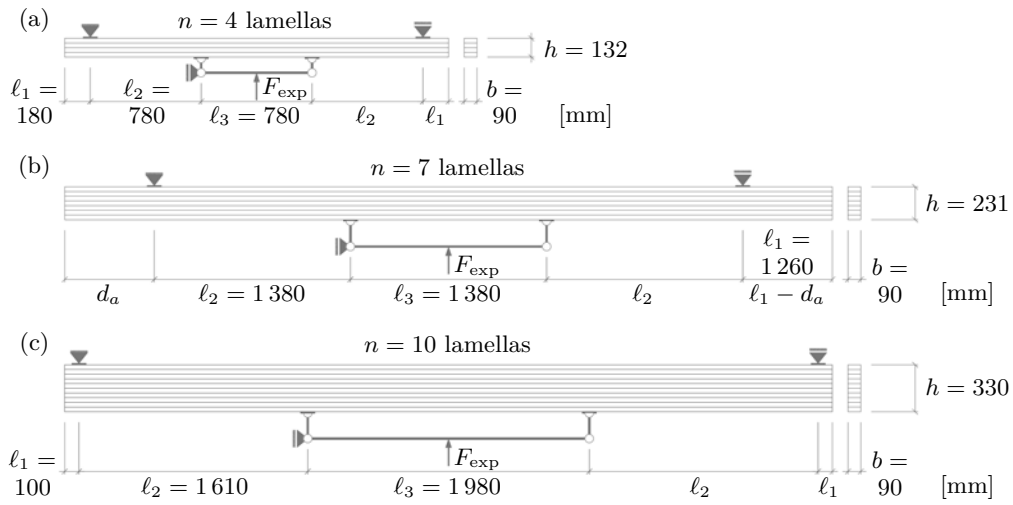[b] All beams had a width of $b = 90$ mm.

Fig. 2.1: Measurements and experimental setup with the applied load F_{exp} of beam types: (a) A/T14-4 and B/T22-4, (b) C/T22-7 with the length d_a to shift a knot group in the top timber board (tensile side) as close as possible to the center, and (c) D/T14-10 and E/T22-10 (modified from [39]).

boards and well-known knot morphology. The virtual reconstruction process of the knot groups and their determination of stiffness and strength properties follows in Section 2.2.

The study comprised a quasi-static four-point bending test of all beams in accordance to the test setup and procedure described in DIN EN 408:2010-12 [16]. The load was applied at an approximate rate of $5\,\text{kN/min}$ until failure occurred and the displacement w_{exp} was measured at the bottom middle of the beam, which corresponded to the compression side. Figure 2.1 illustrates the experimental setup with the applied load F_{exp} of the three beam sizes. In the present thesis relevant documented results are the load-bearing capacity, the system-related stiffness, and the manually recorded geometry of all occurred cracks on all beam surfaces. The data was further processed to define a bending strength and a material-related effective modulus of elasticity.

The experimental load-bearing capacity F_{exp}^*, defined as the maximum load, was translated to the bending strength $f_{\text{b,exp}}$. The system-related stiffness k was computed from a linear regression of the load-displacement curve in the range of $10\,\%$ and $40\,\%$ of F_{exp}^*, which reads as $k_{\text{exp}} = \Delta F_{\text{exp}}/\Delta w_{\text{exp}}$, and is used to determine the material-related effective modulus of elasticity $E_{\text{GLT,exp}}$. The translations were in accordance to DIN EN 408:2010-12 [16] and read as:

$$f_{\text{b,exp}} = \frac{3\,\ell_2\,F_{\text{exp}}^*}{bh^2} \qquad \text{and} \qquad E_{\text{GLT,exp}} = \frac{3\,\ell_2\,\ell_{\text{span}}^2 - 4\,\ell_2^3}{2\,bh^3\left(\frac{2}{k_{\text{exp}}} - \frac{6\,\ell_2}{5\,G\,bh}\right)}, \tag{2.1}$$

where all dimensions ℓ_{span}, ℓ_2, h, and b can be found in Table 2.1 and Fig. 2.1 and G denotes the elastic shear modulus that was assumed to be constant with $G = 650\,\text{N/mm}^2$ according to DIN EN 408:2010-12 [16]. This assumption was based on the findings presented by Kandler et al. [37] and more recently by Balduzzi et al. [2].

It is important to point out that the translation in Eq. (2.1)$_1$ keeps the system character of the load-bearing capacity F_{exp}^* in the bending strength $f_{\text{b,exp}}$. The system character is kept mainly based on two assumptions of the translation, besides only considering the strain and stress in longitudinal direction. First, it assumes a homogeneous material with a linear stress distribution

over the cross-section height in accordance to the theory of linear elasticity and second that failure is encountered when the maximum stress reaches the bending strength in accordance to a perfectly brittle material. However, a GLT beam has significant inhomogeneities due to fluctuation of the timber board stiffness properties. Further, the load-displacement curve may show non-linear behavior until the load-bearing capacity is reached (see Fig. 2.2), which results from either plastification in the compression area or small cracks in the tension area. All this leads to a stress distribution that is different than the assumed one. Thus, the so determined bending strength has to be considered as system parameter. Nevertheless, the translation is still useful for comparisons, e.g. to examine different beam sizes. This follows the conception of the experimental study [39] and the remarks made in [5].

Figure 2.2 shows the measured load-displacement curves and the experimental results of load-bearing capacity and system-related stiffness. In total, 12 beams showed non-linear behavior in the load-displacement curves before reaching the load-bearing capacity (see Figs. 2.2a, 2.2c, and 2.2e). The difference between the two strength classes can clearly be noticed when looking at the system-related stiffness values (see Figs. 2.2b and 2.2f). Figure 2.3a shows the measured data of load-bearing capacity and system-related stiffness, whereas Fig. 2.3b shows the bending strength and material-related effective modulus of elasticity in accordance to Eq. (2.1). Additionally, Table 2.2 gives the measured load-bearing capacity and the system-related stiffness and Table 2.3 the bending strength and the material-related effective modulus of elasticity, corresponding to Figs. 2.3a and 2.3b, respectively. The coefficient of determination between the bending strength and the material-related effective modulus of elasticity shows no significant relation with a value of about 0.48.

The so-called size effect is apparent in the comparison of the two beam sizes, those with $n = 4$ and $n = 10$ lamellas, in Table 2.3, where the bending strengths of the larger beams were recognizably smaller for both strength classes. The effect is related to the weakest link theory for brittle materials, where the enlargement of the stressed volume increases the probability of defects or weak points that lead to failure [63].

Finally, Fig. 2.4 exemplarily shows the recorded crack patterns. The detailed recording is available in the online supplementary material of [39].

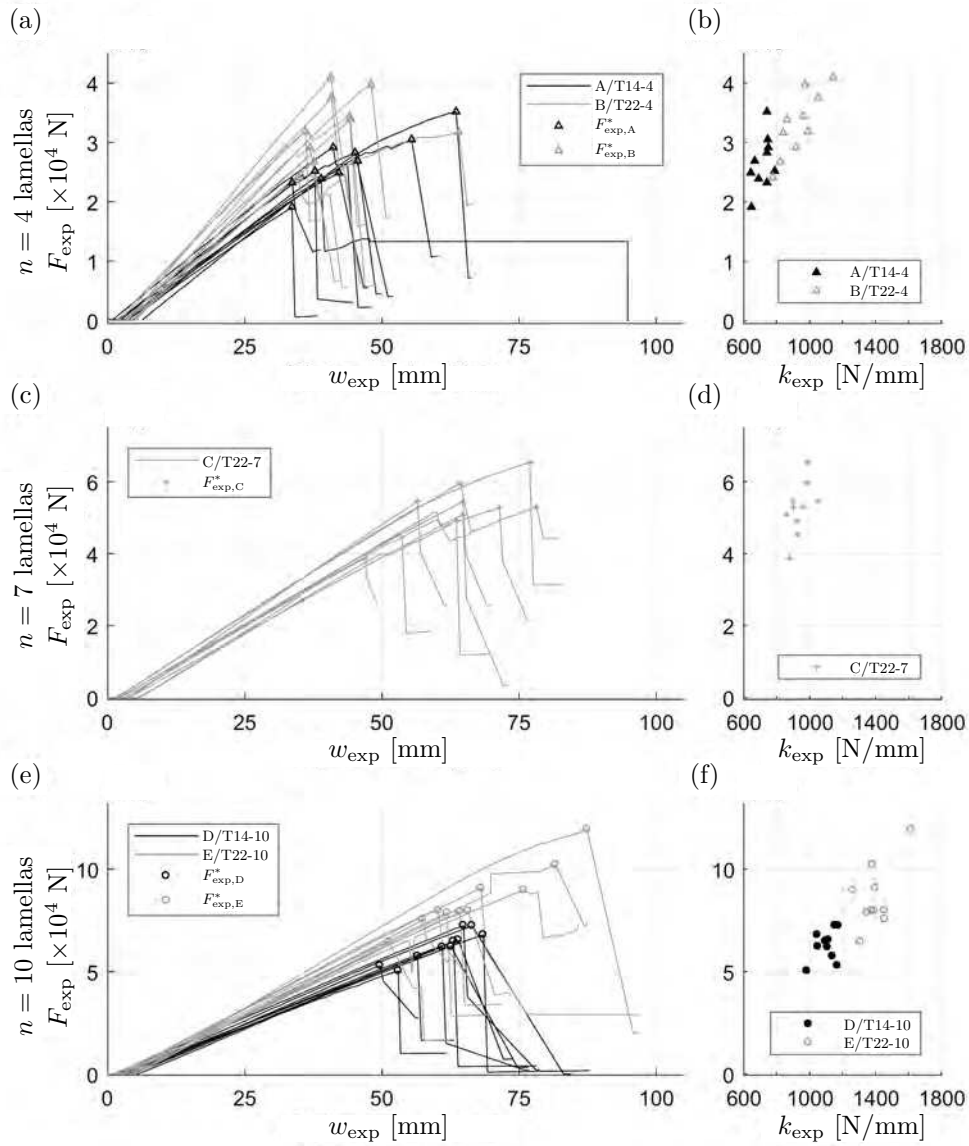**Fig. 2.2:** Experimental load-displacement curve ($F_{\exp}$-$w_{\exp}$-curve) and experimental load-bearing capacity $F_{\exp}^*$ vs. the experimental system stiffness $k_{\exp}$ for beam types: (a,b) A/T14-4 and B/T22-4, (c,d) C/T22-7, and (e,f) D/T14-10 and E/T22-10, respectively (modified from [39]).
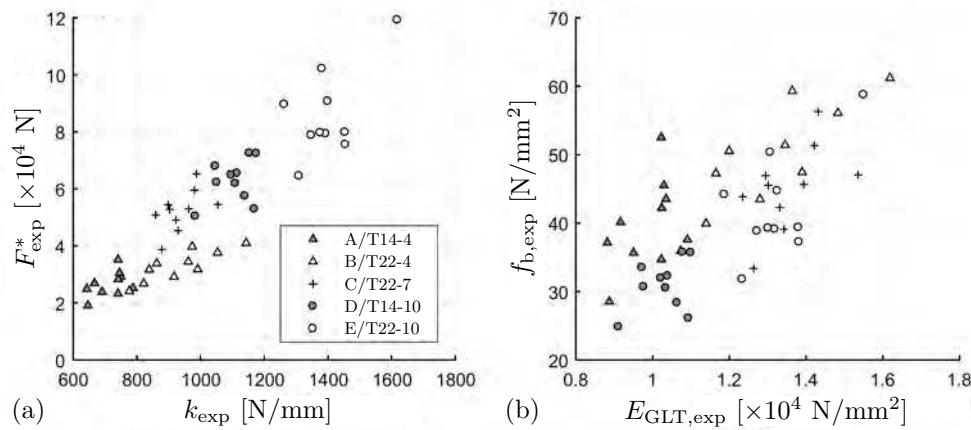
Fig. 2.3: Experimental results: (a) load-bearing capacity F_{exp}^* vs. system-related stiffness k_{exp} and (b) bending strength $f_{\text{b,exp}}$ vs. material-related effective modulus of elasticity $E_{\text{GLT,exp}}$ (modified from [39]).

Tab. 2.2: Load-bearing capacity F_{exp}^* and system-related stiffness k_{exp} for all beam types and all experiments, with minimum, arithmetic mean, maximum value, coefficient of variation CV, and coefficient of determination R^2 between F_{exp}^* and k_{exp}.

Beam Type	Load-bearing capacity F_{exp}^*				System stiffness k_{exp}				R^2
	Min [N]	Mean [N]	Max [N]	CV	Min [N/mm]	Mean [N/mm]	Max [N/mm]	CV	
A/T14-4	19 108	26 635	35 191	0.16	643	715	788	0.07	0.238
B/T22-4	24 075	33 008	41 009	0.16	776	934	1 143	0.12	0.708
C/T22-7	38 720	52 360	65 295	0.13	859	938	1 055	0.06	0.313
D/T14-10	50 379	62 818	72 507	0.11	984	1 104	1 175	0.05	0.145
E/T22-10	64 499	85 943	119 218	0.17	1 263	1 400	1 618	0.07	0.360
All	19 108	52 153	119 218	0.44	643	1 018	1 618	0.24	0.820

Tab. 2.3: Bending strength $f_{\text{b,exp}}$ and material-related effective modulus of elasticity $E_{\text{GLT,exp}}$ for all beam types and all experiments, with minimum, arithmetic mean, maximum value, coefficient of variation CV, and coefficient of determination R^2 between $f_{\text{b,exp}}$ and $E_{\text{GLT,exp}}$.

Beam Type	Bending strength $f_{\text{b,exp}}$				Material stiffness $E_{\text{GLT,exp}}$				R^2
	Min [N/mm²]	Mean [N/mm²]	Max [N/mm²]	CV	Min [N/mm²]	Mean [N/mm²]	Max [N/mm²]	CV	
A/T14-4	28.5	39.7	52.5	0.16	8 818	9 860	10 908	0.07	0.238
B/T22-4	35.9	49.3	61.2	0.16	10 735	13 059	16 190	0.12	0.707
C/T22-7	33.4	45.1	56.3	0.13	12 351	13 553	15 359	0.06	0.312
D/T14-10	24.8	31.0	35.7	0.11	9 109	10 290	10 995	0.06	0.144
E/T22-10	31.8	42.4	58.8	0.17	11 870	13 258	15 502	0.07	0.363
All	24.8	41.5	61.2	0.21	8 818	12 004	16 190	0.16	0.475
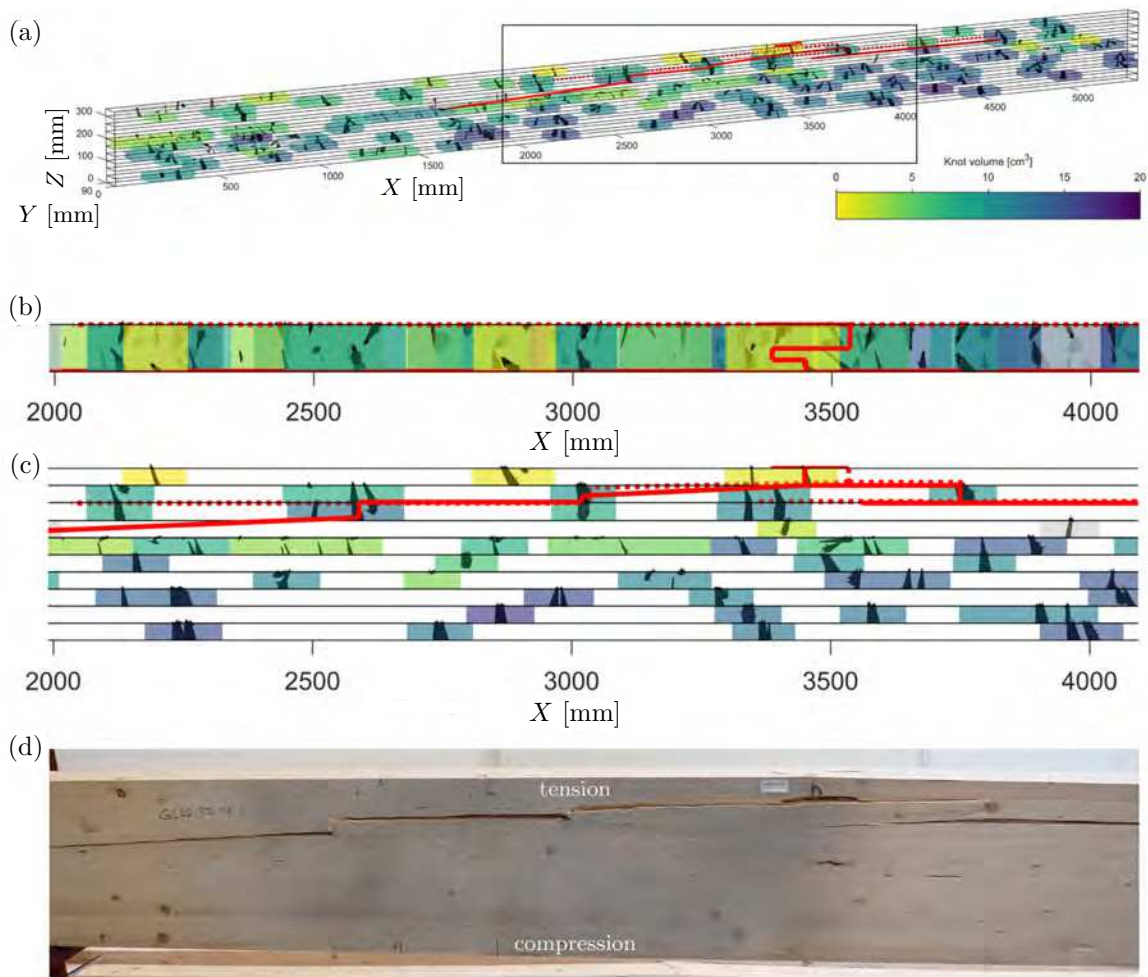
Fig. 2.4: Depiction of automatically reconstructed three-dimensional knots with manual crack recording
on all surfaces: (a) overview of a whole GLT beam, (b) top view, (c) front view of an enlargement,
and (d) the corresponding photo from the experiment (modified from [39]).

2.2 Determination of material properties

The present thesis uses effective material properties of timber board sections on basis of well-
known knot morphology, which were determined by Kandler et al. [41]. Each individual timber
board was subjected to the following four steps:

- an automated three-dimensional reconstruction of the knot geometry that was proposed by
  Kandler et al. [38, 40] and was based on data sets that were gained by surface laser scans
  (see Figs. 2.5a to 2.5c),
- selecting the knots and grouping them into knot groups with respect to their expected
  significance on the mechanical behavior [41] (see Fig. 2.5d),
- deriving a stiffness profile using a micromechanical multiscale model proposed by Hofstetter
  et al. [35] and applying a three-dimensional FE approach with the fiber course derived from
  the selected knot groups as described by Hackspiel et al. [33] and Lukacevic and Füssl [47]
  (see Figs. 2.5e and 2.5f), and
- using IPs for the knot group sections in order to determine strength profiles [41] (see
  Fig. 2.5g).

The procedures of each step are explained in more detail in the following four paragraphs.
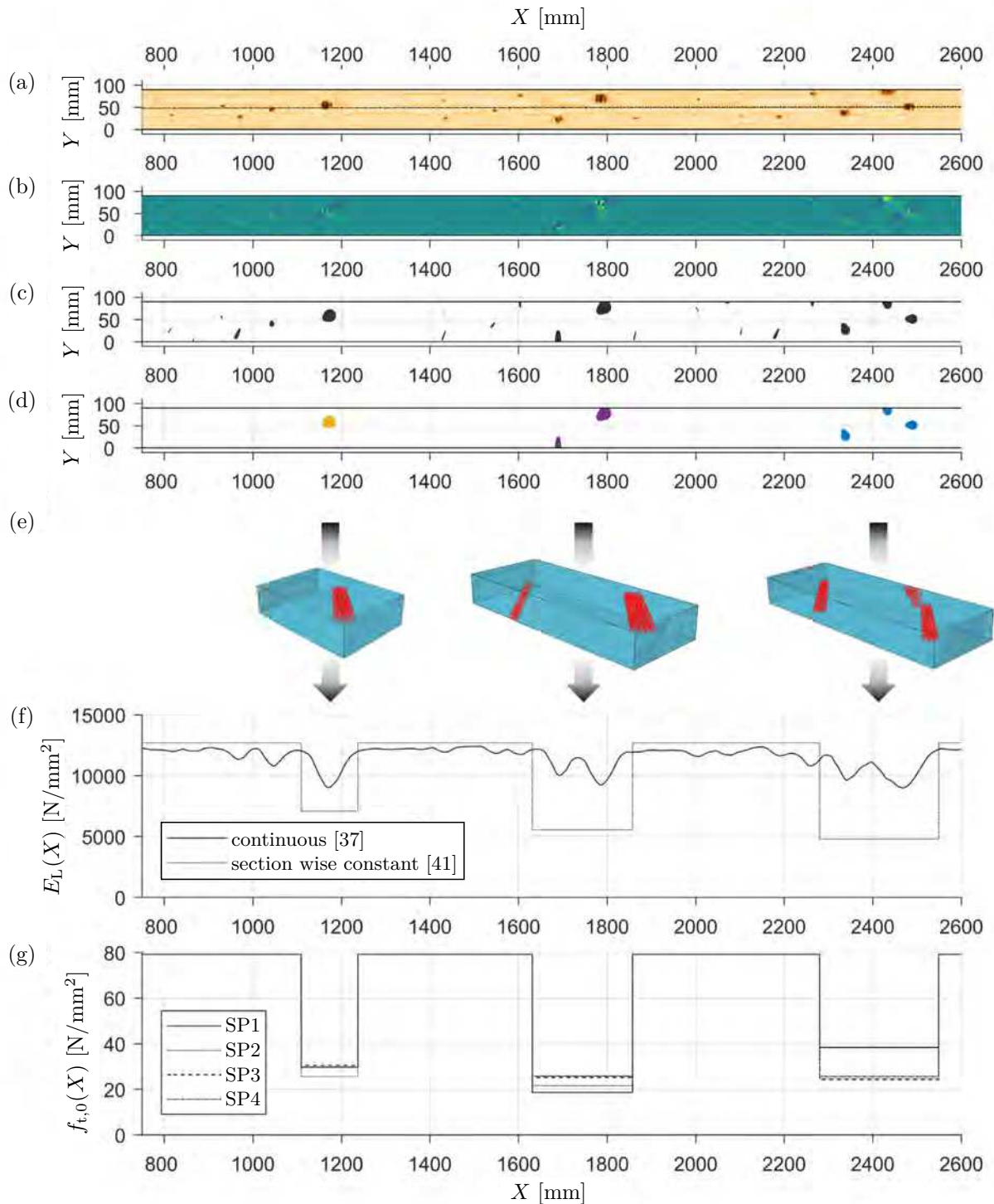
Fig. 2.5: Determination of stiffness and strength profiles. Each timber board (a) is laser scanned during the grading process and (b) results in fiber angle measurements, which are then used to (c) automatically reconstruct the knot geometry and (d) identify knots on its own or in interacting groups with assumed relevance. Each knot group is used in (e) a three-dimensional FE approach that derives (f) section-wise constant stiffness profile. Each knot group leads to (g) four section-wise constant strengths that define strength profiles. (modified from [41]).

In the first step, the local longitudinal fiber directions were determined by surface laser scans (see Fig. 2.5a) using the so-called tracheid effect [65, 52, 36], which uses the more pronounced light propagation in direction parallel to the wood fiber. An originally circular laser dot spreads to an elliptical shape on the wood surface. The major axis of the ellipse constitutes the in-plane angle φ_{in} and the ratio of minor to major axis was mapped to the corresponding out-of-plane angle φ_{out}. A possible sensitivity of the mapped out-of-plane angle to the roughness and the color of the wood surface was detected and remarked by Briggert et al. [8]. Together the two angles defined the three-dimensional fiber angle estimate φ, which was used to derive the knot area on the wood surface (see Fig. 2.5b). Additionally, the location of the pith was estimated by the approach presented by Lukacevic [46] and Olsson and Oscarsson [53]. This was done by using the arithmetic means of the center points of multiple circles fitted to the year rings of photographs of both cross section ends and their linear connection. Each geometry of a knot was represented by a rotationally symmetric cone defined by a cone apex, a cone axis vector, and an opening angle α. An assumption placed the cone apex on the defined pith. The cone axis vector was computed from information of the pith location and the knot areas. In this process each knot reconstruction had either a pith location inside or outside of the timber board and a single or multiple corresponding knot areas. Next, the cone opening angle of a knot was determined by fitting the intersected cone areas with the wood surface and the estimated knot areas in a least-square sense [41]. Finally, an optimization scheme was applied. The data set used in [41] was based on a resolution of the laser scans of approximately 1 mm in longitudinal and 4 mm in lateral direction, which was sufficient to reconstruct small knots with opening angles of α smaller than 1.5°. However, in [41] such small knots led to discretization problems during meshing in the subsequent step of applying the three-dimensional FE approach and were omitted without expecting to impair the credibility of the material behavior. Finally, the three-dimensional knot geometry was established by the initial data set of laser scans (see Fig. 2.5c).

In the second step, the mechanical behavior of timber boards was assumed to be only influenced by large knots or the interaction of multiple knots [41]. The knot size was quantified by the visible knot area, which was defined as the sum of all intersected areas of a knot with the surface of the timber board. Large knots were then all knots with a visible knot area above the 70 %-quantile of the individual timber board. Each large knot initiated a knot group in the model. The interaction between knots was determined by setting a threshold distance in longitudinal direction X. The threshold distances for large and small knots were 200 mm and 40 mm, respectively. If an interaction was detected, knot groups were merged or small knots were added to a knot group. An exception applies to knot groups that exceed a maximum length of 300 mm, these groups were split between corresponding knots with the mutually greatest X-distance. This limitation resulted from the calibration of the IPs in [48]. At this point knot groups with significance on the material behavior were identified (see Fig. 2.5d).

In the third step, the knot groups were used to establish the three-dimensional fiber course with the so-called flow-grain analogy [24]. It was assumed that the fiber course in the LT-plane followed a laminar flow with elliptical obstacles representing knots and that the fiber directions in the LR-plane could be represented by polynomials, which were fitted to year ring characteristics in photographs [49]. Thus, when the knot geometries were known, the local material directions could be calculated in each integration point. Additionally, for each board the clear wood stiffness tensor was calculated by a micromechanical multiscale model [35], where mass density and moisture content served as the main input. The three-dimensional FE approach models each knot group under consideration of the reconstructed three-dimensional knot geometry, the determined three-dimensional fiber course, and the clear wood stiffness tensor (see Fig. 2.5e). Each knot group model was loaded in a displacement controlled manner and resulted in an effective longitudinal stiffness.Stiffness profiles combined the results of knot groups and clear

wood for each board. This led to section-wise constant values for an effective longitudinal stiffness $E_L(X)$ that defined the stiffness tensor at the position X along the board by being substituted into the clear wood tensor [41]. Figure 2.5f shows two stiffness profiles with the used section-wise constant properties [41] and continuous properties proposed by Kandler et al. [37].

In the final step the strength for the clear wood was scaled according to its density and the strength of knot groups was estimated by different parameter sets [41]. The following parameters were considered:

- knot-area-ratio (KAR), which was the knot area of all knots within a knot group projected to the cross section divided by the cross section area,
- knot area, which was the visible knot area on board surfaces,
- weighted knot area, which additionally distinguished between the knot area of the parallel sides
- knot volume,
- interface, which was the total area of the knot surface in contact with the clear wood, and
- foley-area-ratio (FAR), which was—in analogy to KAR—the area that showed a deviating fiber course in the vicinity of knots.

Four strength profiles (SP1 to SP4) were defined, where each profile used a different IP to determine the knot group strengths:

- SP1: IP 1 ∼ KAR + weighted knot area + knot volume + interface + FAR + interaction terms,
- SP2: IP 2 ∼ KAR + knot area + knot volume + interface,
- SP3: IP 3 ∼ KAR, and
- SP4: IP 4 ∼ KAR + knot area + knot volume.

The strength profiles combined the computed strengths of the clear wood as well as the knot groups. This led to section-wise constant values for the tensile strength in longitudinal direction $f_{t,0}(X)$ at the position X along the board. Figure 2.5g shows all four strength profiles of a timber board, which were presented by Kandler et al. [39] and Kandler et al. [41].

Further on, the plausibility of the strength profiles is discussed. As described in Section 2.1 the experimental study was conducted considering two strength grades T14 and T22 (see Table 2.1). The predicted material properties gained by the previously described determination process is available for a total of 140 and 138 timber boards of strength grades T14 and T22, respectively. The strength for each profile and timber board is determined by the lowest strength value in the strength profile in the range of the corresponding beam length. Figure 2.6 shows the frequency distribution of the timber board strength in longitudinal direction $f_{t,0,\mathrm{sim}}$, for both strength grades. Table 2.4 gives the corresponding data for the characteristic lamella tensile strength in longitudinal direction $f_{t,0,k}$ according to DIN EN 14080:2013-09 [14], the 5 %-quantile and 50 %-quantile lamella tensile strength in longitudinal direction, $f_{t,0,05,\mathrm{sim}}$ and $f_{t,0,05,\mathrm{sim}}$, respectively. Strength profiles SP1 and SP2 do not show a suitable distributions with too low 5 %-quantile values compared to the corresponding characteristic values for both strength grades. All 5 %-quantile values of strength profiles SP1 and SP2 are the global minimum of all strength profiles with a value of $10\,\mathrm{N/mm^2}$. Strength profiles SP3 and SP4 show a better agreement of the distributions with comparison of their 5 %-quantile values with the corresponding characteristic values for both strength grades. Hence, only strength profiles SP3 and SP4 are further considered. No predicted value is greater than $40\,\mathrm{N/mm^2}$. The greatest coefficient of variation occurs in strength grade T14 of SP3 and is 0.24. Strength grade T22 of SP3 shows the absolute minimum underestimation of $4.96\,\mathrm{N/mm^2}$, which corresponds also to the relative minimum underestimation of about 23 %. An overestimation is only observed for strength grade T14 of SP4 with a value of $2.70\,\mathrm{N/mm^2}$, which is a relative overestimation of about 19 %.

The effective stiffness and strength profiles are perfectly suited to pass on the necessary information of the timber morphology to a computational model. However, as mentioned in the previous paragraph the data of the timber board profiles is limited. The stiffness and strength profiles are available for all boards used by beam types A/T14-4, B/T22-4, and D/T14-10 with ten beams each, whereas only 8 beams of type E/T22-10 are available.

Tab. 2.4: Strength profiles, with charasteristic lamella tensile strength in longitudinal direction $f_{t,0,k}$ according to DIN EN 14080:2013-09 [14], 5 %-quantile and 50 %-quantile of the predicted lamella tensile strength in longitudinal direction, $f_{t,0,05,sim}$ and $f_{t,0,50,sim}$, respectively, and coefficient of variation CV.

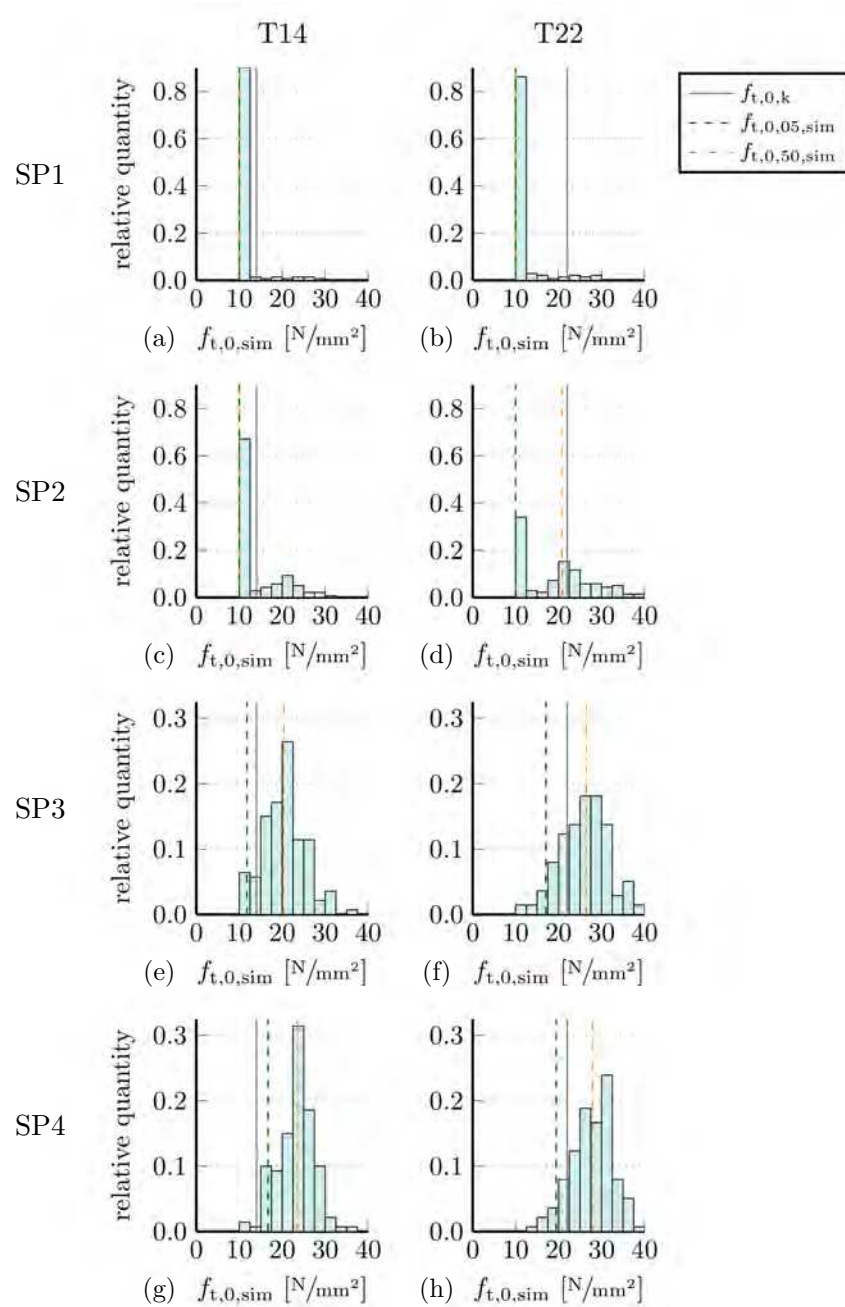| Strength profile	Strength grade	$f_{t,0,k}$ [N/mm²]	$f_{t,0,50,sim}$ [N/mm²]	$f_{t,0,05,sim}$ [N/mm²]	CV
SP1	T14	14.0	10.00	10.00	0.52
	T22	22.0	10.00	10.00	0.42
SP2	T14	14.0	10.00	10.00	0.44
	T22	22.0	20.80	10.00	0.48
SP3	T14	14.0	20.37	11.79	0.24
	T22	22.0	26.44	17.04	0.21
SP4	T14	14.0	23.51	16.70	0.18
	T22	22.0	27.90	19.45	0.17

Fig. 2.6: Frequency distribution of the predicted tensile strength in longitudinal direction $f_{t,0,sim}$ with the quantity relative to the total quantity of timber boards for: (a,b) SP1, (c,d) SP2, (e,f) SP3, and (g,h) SP4 and strength grades T14 and T22, respectively, with drawn values in accordance to Table 2.4.

Chapter 3

Computational modeling approach

A three-dimensional computational modeling approach is developed to predict the load-bearing capacity as well as failure mechanisms of GLT beams subjected to four-point bending tests until failure. Knot groups are implemented with the presented section-wise constant effective stiffness and strength profiles (Section 2.2) that supply the material properties without following a predefined grid of each individual timber board that is used in the virtualized GLT beam setup. Quasi-brittle material failure is considered for the modeled failure mechanisms. Vertical discrete cracks are realized with XFEM and delamination between timber boards, describing horizontal discrete cracks, is realized with cohesive surfaces. Both crack orientations use a modified traction-separation law to describe the crack evolution. The delamination is a simplified way to consider horizontal crack propagation, it is not intended to model failure in the glue lines. Additionally, the horizontal merging between vertical cracks at different horizontal positions in adjacent boards is enabled by the implementation of delamination. The load is applied in a displacement controlled manner. The benefit of a three-dimensional approach is the easy adaption for future research, where three-dimensional strain and stress fields are necessary. The modeling approach is realized with the commercial FE software Abaqus 2019.

The geometric basic parts that build up the experimental setup are the timber boards of the GLT beam, the construction for the load distribution, and two bearing plates (see Fig. 3.1). The is defined using the following global right-handed coordinates: X in longitudinal direction of the beam, Y in width direction of the beam, and Z in direction of the applied displacement w_{load}. The displacement directions u, v, and w correspond, respectively, to the global coordinate directions (see Fig. 3.1). The displacement w_{sim} was measured at the bottom middle of the beam, which corresponded to the compression side (see Fig. 3.1).
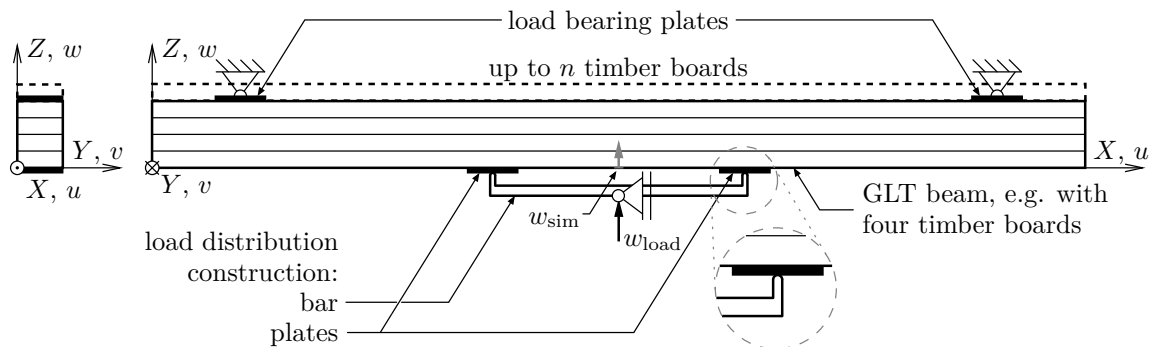

Fig. 3.1: Geometric parts, load direction, and global coordinates of modeling approach.

3.1 Fundamental methods

The theory of linear elasticity is a mathematical description of the mechanical behavior of solid objects under certain loads, e.g. an applied load or displacement. It consists of three fundamental equations for an arbitrary point $\mathbf{x}$ within the volume V or on the surface S of an solid object for the exemplary load cases [50]:

- Description of the relation between the displacement vector $\mathbf{u}(\mathbf{x})$ and strain tensor $\boldsymbol{\varepsilon}(\mathbf{x})$ by the kinematic equation:

$$\boldsymbol{\varepsilon}(\mathbf{x}) = \frac{1}{2}\left[\left(\frac{\partial \mathbf{u}}{\partial \mathbf{x}}\right)^{\mathrm{T}} + \frac{\partial \mathbf{u}}{\partial \mathbf{x}}\right] = \nabla^{\mathrm{s}}\mathbf{u}(\mathbf{x}) \qquad \forall \mathbf{x} \in \{V, S\} \ , \tag{3.1}$$

  where ∇^{s} denotes the symmetric gradient.

- Formulation of an equilibrium regarding stress tensor $\boldsymbol{\sigma}(\mathbf{x})$, volume force vector $\mathbf{f}(\mathbf{x})$, and the consideration of a static scenario with $\overline{\mathbf{b}} = 0$:

$$\operatorname{div}\boldsymbol{\sigma}(\mathbf{x}) + \mathbf{f}(\mathbf{x}) = \rho\,\overline{\mathbf{b}}(\mathbf{x}) = 0 \qquad \forall \mathbf{x} \in \{V, S\} \ . \tag{3.2}$$

- Establishing the interaction of the stain tensor $\boldsymbol{\varepsilon}(\mathbf{x})$ and the stress tensor $\boldsymbol{\sigma}(\mathbf{x})$ with the constitutive equation in accordance to Hooke's law:

$$\boldsymbol{\sigma}(\mathbf{x}) = \mathbb{C}(\mathbf{x}) : \boldsymbol{\varepsilon}(\mathbf{x}) = \mathbb{C}(\mathbf{x}) : \nabla^{\mathrm{s}}\mathbf{u}(\mathbf{x}) \qquad \forall \mathbf{x} \in \{V, S\} \ , \tag{3.3}$$

  where $\mathbb{C}(\mathbf{x})$ denotes the elasticity tensor.

Consequently, an analytical solution is obtained when those three fundamental equations (3.1) to (3.3) obey all initial and boundary conditions for all arbitrary points at every time. Such a solution is not available for a GLT beam model that considers all the aspects in the present case.

In order to obtain an approximate solution, the infinite number of points is reduced to a finite one with the use of FEM and discrete cracks are realized with the use of XFEM. The non-linearity of the approximate solution is considered by using an incremental-iterative method, where the load is applied in increments and the incremental solution is found by iteration.

3.1.1 Finite element method

A common and widespread method to obtain an approximate solution of the mechanical behavior is to describe the solid objects with a discrete system FEM is used [50]. The discrete system is build up by finite elements, which are defined by nodes and are arranged by an FE mesh (see Fig. 3.2). This method uses the discrete system to obtain approximations of the strain tensor $\boldsymbol{\varepsilon}(\mathbf{x})$ and stress tensor $\boldsymbol{\sigma}(\mathbf{x})$ within a finite element and consists of the following key points:

- representing the displacement within a single finite element,
- selecting the nodal degrees of freedom of an element from all system degrees of freedom,
- using the principal of virtual power to derive constitutive equations on system level, and
- postprocessing for the evaluation of strain and stress.

The displacement at an arbitrary point $\mathbf{x}$ in an element e with the volume V_e and the surface S_e is described by the displacement vector $\mathbf{u}^e(\mathbf{x})$, which reads as:

$$\mathbf{u}^e(\mathbf{x}) = \mathbf{N}^e(\mathbf{x}) \cdot \mathbf{q}^e \qquad \forall \mathbf{x} \in \{V_e, S_e\} \ , \tag{3.4}$$

where $\mathbf{N}^e(\mathbf{x})$ describes the interpolation function matrix and $\mathbf{q}^e$ the nodal degrees of freedom vector. The interpolation function matrix $\mathbf{N}^e(\mathbf{x})$ contains polynomial functions of a certain order, the so-called shape functions, which prescribe the displacement behavior within the element e for $\mathbf{x} \in \{V_e, S_e\}$.

The nodal degrees of freedom vector $\mathbf{q}^e$ of an element e is selected from the system degrees of freedom vector $\mathbf{q}$, which contains all degrees of freedom of the system, by the corresponding assembling matrix $\mathbf{a}^e$, which reads as:

$$\mathbf{q}^e = \mathbf{a}^e \cdot \mathbf{q}. \tag{3.5}$$

Equation (3.5) provides access to the individual elements from perspective of the system.

The use of the principle of virtual power in conjunction with the fundamental equations (3.1) to (3.3) boundary conditions—first applied on a single element and second on the system with Eq. (3.5) for the localization of elements—leads to the significant equation on level of the system:

$$\mathbf{p} = \widetilde{\mathbf{K}} \cdot \mathbf{q} \quad \Rightarrow \quad \mathbf{q} = \widetilde{\mathbf{K}}^{-1} \cdot \mathbf{p}, \tag{3.6}$$

where $\widetilde{\mathbf{K}}$ describes the system stiffness matrix, which needs to be positive definite for the inversion, $\mathbf{q}$ the system nodal degrees of freedom vector, and $\mathbf{p}$ the system nodal load vector. Constraints can be related to degrees of freedom in the system nodal degrees of freedom vector $\mathbf{q}$ or loads in the system nodal load vector $\mathbf{p}$.

Finally, postprocessing leads to the strain tensor $\boldsymbol{\varepsilon}^e(\mathbf{x})$ and stress tensor $\boldsymbol{\sigma}^e(\mathbf{x})$ of the element e. Therefore, the displacement vector (3.4) is specified with Eqs. (3.5) and (3.6) to use the result in the fundamental equations (3.1) and (3.3), which read as, respectively:

$$\boldsymbol{\varepsilon}^e(\mathbf{x}) = \nabla^{\mathrm{s}}\mathbf{u}^e(\mathbf{x}), \quad \boldsymbol{\sigma}^e(\mathbf{x}) = \mathbb{C}(\mathbf{x}) : \boldsymbol{\varepsilon}^e(\mathbf{x}). \tag{3.7}$$

3.1.2 Extended finite element method

Belytschko and Black [3] presented a method to describe elastic crack propagation in finite elements known as XFEM. The method exploits the partition of unity to enable the local inclusion of a priori knowledge, which was introduced by Melenk and Babuška [51]. The present approach uses the implementation of XFEM in Abaqus 2019 to initiate and propagate cracks along an arbitrary, solution-depending crack path with minimal restrictions to the discretization of the system [1] (see Fig. 3.2a). The used FE software utilizes an extension of the equivalent polynomial methodology by Ventura and Benvenuti [62] for the evaluation of the stiffness matrix of a cracked element. This method describes a crack that splits a single finite elements into two parts and uses a damage formulation to govern the interaction until complete separation of the two parts comes into effect at full damage. It consists of the following key points:

- extending the displacement formulation (3.4), which represents the enrichment of a finite element with so-called phantom nodes that enable a single element to split into two parts,
- determining the crack position by the level-set method, and
- formulating the interaction of the two parts with the cohesive-segment method until complete separation.

The extension of Eq. (3.4) gains the enriched displacement vector $\mathbf{u}^{\tilde{e}}(\mathbf{x})$ at an arbitrary point $\mathbf{x}$ within the volume $V_{\tilde{e}}$ or on the surface $S_{\tilde{e}}$ of an enriched element $\tilde{e}$, which reads as:

$$\mathbf{u}^{\tilde{e}}(\mathbf{x}) = \mathbf{N}^e(\mathbf{x}) \cdot \left(\mathbf{q}^e + H(\mathbf{x})\,\mathbf{q}^{\tilde{e}} \right) \qquad \forall \mathbf{x} \in \{V_{\tilde{e}}, S_{\tilde{e}}\}, \tag{3.8}$$

where $H(\mathbf{x})$ describes the associated discontinuous jump function and $\mathbf{q}^{\tilde{e}}$ the enriched degrees of freedom vector. If an enriched element $\tilde{e}$ experiences a crack, the associated discontinuous jump function $H(\mathbf{x})$ introduces the enriched degrees of freedom $\mathbf{q}^{\tilde{e}}$. The additional degrees of freedom are considered as phantom nodes that initially superpose the real nodes. The formulation of a discontinuity across the whole enriched element avoids the consideration of crack-tip singularities. Consequently two element parts are created, where each part consists of real and phantom nodes (see Fig. 3.2b).

The level-set method is used to describe the position of the occurring crack and enables an arbitrary crack path without remeshing. The implemented discontinuity across the whole enriched element is responsible for the fact that only one level-set in each node is sufficient to describe the position of the crack. The crack of an enriched element defines the shape of the two parts. Both the level-set method and the formulation of an enriched element in accordance to Eq. (3.8) describe the initiation and propagation of a crack.

The cohesive-segment method describes the interaction between the two parts by using a cohesive material law, such as a traction-separation law. The initiation of a crack and therefore an introduced discontinuity in an enriched element allows the phantom nodes to move apart from the corresponding real nodes. Such a discontinuity is considered as implemented progressing damage that governs the interaction of the two parts. A modified traction-separation law is used to describe this evolution of damage. When full damage is reached, the phantom nodes move independently from the corresponding real nodes and the two parts are completely separated.

(a)   (b)
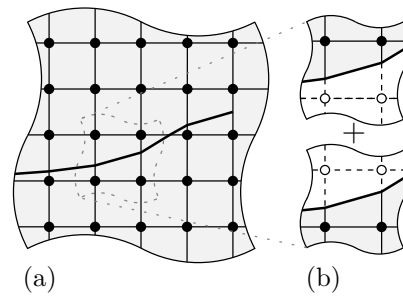
Fig. 3.2: Schematic of an FE mesh of enriched nodes with (a) an arbitrary, solution-depending crack path and the detail of (b) both element parts composing an enriched element that consists of real and phantom nodes; full and hollow circles denote real and phantom nodes, respectively (redrawn with modifications from [45, 58]).

3.1.3 Incremental-iterative method

The model approach is expected to behave non-linearly due to discrete cracks, delamination, and the modeling of the load introduction and bearing plates, which makes it necessary to use a suitable method to obtain the approximate solution. An incremental-iterative method is used commonly in FE software [64]. This method combines two approaches, application of the load in increments and striving for convergence of each load increment with an iterative method. Abaqus implements this method by introducing a fictitious time scale for the incrementation, reaching from the initial state to the fully applied load state and using the Newton-Raphson method for the iteration [1]. In the present thesis the fictitious time scale consists of time increments that apply the load in increments. The size of the time increments and therefore the size of the load increments is defined during the solution process according to an empirical algorithm, e.g. the size may be reduced if no convergence was observed within certain iterations of an increment or may be increased if the last two increments showed convergence within only a few iterations.

Convergence in an iteration is achieved, when the external and internal forces on each node are in equilibrium or at least comply with a given tolerance. The number of iterations depends on the solution history, convergence behavior, and prescribed threshold values. The proceeding of iterations in an increment of the incremental-iterative method is exemplary given in the sequel.

The Newton-Raphson method evaluates the system stiffness tangent K_{i-1}^k in each iteration i of an increment k. The determination of the current load P^k is only done once for each increment by adding the applied load increment ΔP^k to the previous load P^{k-1}. The intersection of the system stiffness tangent K_{i-1}^k and the current load P^k determines the displacement u_i^k. The convergence behavior is determined on basis of the force residual R_i^k, which is an equilibrium formulation obtained by the difference of the current load P^k and the internal nodal forces I_i^k. Additionally, the convergence is judged on the displacement correction d_i^k, which is the difference of the displacement of the iteration i and the displacement of the previous iteration $i-1$. Figure 3.3 exemplarily shows the specific iterations of increment k that leads to the a priory unknown load-displacement curve (P-u-curve): First the current load P^k is determined. Afterwards the first iteration $i=1$ starts by evaluating the tangent of the system stiffness K_0^k and the force residual R_1^k. The force residual R_1^k or the displacement correction d_1^k exceeds the convergence tolerance and the second iteration $i=2$ starts. This is repeated until the force residual R_3^k and the displacement correction d_3^k obey a certain convergence tolerance in the third iteration $i=3$.
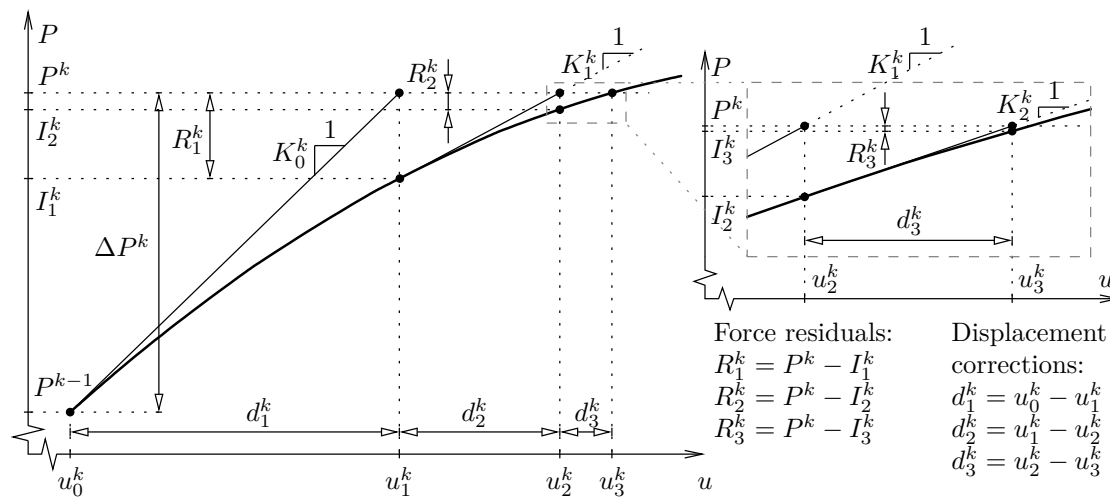
Fig. 3.3: Increment-iteration method of the increment k with three iterations, where P denotes the load and u the displacement and the a priory unknown P-u-curve is illustrated for better understanding (redrawn with modifications from [1]).

3.2 Constitutive material models

The material in the present approach is assumed to be section-wise homogeneous and to comply with the theory of linear elasticity, which leads to the use of the generalized Hooke's law. This constitutive law relates the Cauchy stress tensor $\boldsymbol{\sigma}(\mathbf{x})$ and the linearized strain tensor $\boldsymbol{\varepsilon}(\mathbf{x})$ at an arbitrary point $\mathbf{x}$ within the volume V_s or on the surface S_s of a timber board section or a non-timber components, both detonated with s, which reads as:

$$\boldsymbol{\sigma}(\mathbf{x}) = \mathbb{C}_s : \boldsymbol{\varepsilon}(\mathbf{x}) \qquad \forall \mathbf{x} \in \{V_s, S_s\} \;, \tag{3.9}$$

where $\mathbb{C}_s$ describes the elasticity tensor. Further on, two material models are distinguished for timber boards and non-timber components. The orientation of those material models is depicted in Figs. 3.4a and 3.4b, respectively.
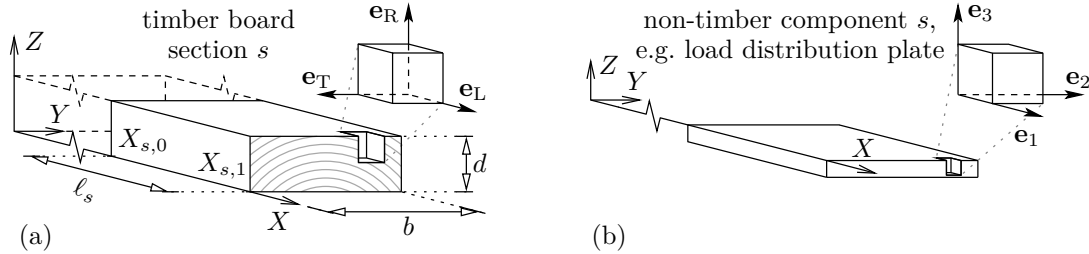
Fig. 3.4: Orientation of the constitutive material model for (a) a timber board section with the definition of their dimensions and (b) a non-timber component with general arbitrary orientation due to isotropic properties.

3.2.1 Timber boards

Keylwerth [42] and Kollmann [44] described the mechanical behavior of wood with the generalized Hooke's law from Eq. (3.9). The timber boards inherit their orthotropic properties from the morphology of wood, which is defined due to the natural growth process. Figure 3.4a shows the three main material directions with the unit vectors $\mathbf{e}_\mathrm{L}$ in longitudinal direction, $\mathbf{e}_\mathrm{R}$ radial direction, and $\mathbf{e}_\mathrm{T}$ tangential direction, which are aligned in X-direction, opposed to Y-direction, and in Z-direction of the model, respectively. A timber board section s has dimensions that correspond to the total thickness d and width b of a timber board. The length ℓ_s is measured in longitudinal direction X with the start and end position, $X_{s,0}$ and $X_{s,1}$, respectively (see Fig. 3.4a). The start and end are in accordance to the jump discontinuity of the stiffness profile (see Fig. 2.5f). Exploiting the symmetry characteristics of an orthotropic material that is described by Hooke's law (3.9) leads to six remaining equations and reduces the independent components of the elasticity tensor $\mathbb{C}_s$ from 81 to nine, which in Mandel notation reads as:

$$
\begin{bmatrix}
\sigma_\mathrm{LL} \\
\sigma_\mathrm{RR} \\
\sigma_\mathrm{TT} \\
\sqrt{2}\,\sigma_\mathrm{LR} \\
\sqrt{2}\,\sigma_\mathrm{LT} \\
\sqrt{2}\,\sigma_\mathrm{RT}
\end{bmatrix}
=
\begin{bmatrix}
C_\mathrm{LLLL} & C_\mathrm{LLRR} & C_\mathrm{LLTT} & 0 & 0 & 0 \\
 & C_\mathrm{RRRR} & C_\mathrm{RRTT} & 0 & 0 & 0 \\
 & & C_\mathrm{TTTT} & 0 & 0 & 0 \\
 & & & 2\,C_\mathrm{LRLR} & 0 & 0 \\
 & \text{symm.} & & & 2\,C_\mathrm{LTLT} & 0 \\
 & & & & & 2\,C_\mathrm{RTRT}
\end{bmatrix}
\cdot
\begin{bmatrix}
\varepsilon_\mathrm{LL} \\
\varepsilon_\mathrm{RR} \\
\varepsilon_\mathrm{TT} \\
\sqrt{2}\,\varepsilon_\mathrm{LR} \\
\sqrt{2}\,\varepsilon_\mathrm{LT} \\
\sqrt{2}\,\varepsilon_\mathrm{RT}
\end{bmatrix}.
\tag{3.10}
$$

In the present thesis the elasticity tensor $\mathbb{C}_s$ is defined as described in Section 2.2 with the presented stiffness profiles.

3.2.2 Non-timber components

The load distribution construction and the bearing plates are assumed to be quasi-rigid. Their material behavior is still described by Hook's law (3.9), however this time with isotropic properties. Therefore, the orientation of unit vectors $\mathbf{e}_1$, $\mathbf{e}_2$, and $\mathbf{e}_3$ is arbitrary. Figure 3.4b shows an example of the material orientation corresponding to the model coordinates. The material model has identical constant properties within all non-timber components s. Exploiting the symmetry characteristics of an isotropic material that is described by Hooke's law (3.9) leads to six remaining

equations and reduces the independent coefficients of the elasticity tensor $\mathbb{C}_s$ from 81 to three with only two independent material parameters, which in Mandel notation reads as:

$$
\begin{bmatrix}
\sigma_{11} \\
\sigma_{22} \\
\sigma_{33} \\
\sqrt{2}\,\sigma_{12} \\
\sqrt{2}\,\sigma_{13} \\
\sqrt{2}\,\sigma_{23}
\end{bmatrix}
=
\frac{1}{1+\nu}
\begin{bmatrix}
\frac{(1-\nu)\,E}{1-2\,\nu} & \frac{\nu\,E}{1-2\,\nu} & \frac{\nu\,E}{1-2\,\nu} & 0 & 0 & 0 \\
 & \frac{(1-\nu)\,E}{1-2\,\nu} & \frac{\nu\,E}{1-2\,\nu} & 0 & 0 & 0 \\
 & & \frac{(1-\nu)\,E}{1-2\,\nu} & 0 & 0 & 0 \\
 & & & E & 0 & 0 \\
 & \text{symm.} & & & E & 0 \\
 & & & & & E
\end{bmatrix}
\cdot
\begin{bmatrix}
\varepsilon_{11} \\
\varepsilon_{22} \\
\varepsilon_{33} \\
\sqrt{2}\,\varepsilon_{12} \\
\sqrt{2}\,\varepsilon_{13} \\
\sqrt{2}\,\varepsilon_{23}
\end{bmatrix},
\tag{3.11}
$$

where E describes the modulus of elasticity and ν the Poisson's ratio as the only two independent material parameters. Specification of Eq. (3.11) for $E \to \infty$ and $\nu \in (-1, 0.5)$ leads to a quasi-rigid component.

3.3 Modified traction-separation law

The presented computational modeling approach is designed to account for discrete cracks in finite elements of timber boards, which develop crack planes with normal vector in X-direction, and delamination between timber boards, which consequently form crack planes with normal vector in Z-direction. A discrete crack or the delamination is realized by the initiation of damage, which weakens the traction between the two corresponding crack planes and evolves until no traction is transmitted. As a result the two corresponding crack planes move independently from each other. The following paragraphs elaborate on the assumed fracture behavior before discussing the general cohesive material behavior and its modifications to model damage in a finite element or a contact constraint point at the occurrence of discrete cracks or delamination, respectively. In this work the fracture realization consists of:

- the initiation of damage that is determined by a maximum nominal stress criterion,
- the evolution of damage that is described by a damage evolution law that degrades the nominal traction stress vector of a linear elastic traction-separation law until it becomes a zero-vector, and
- a stabilization scheme that is implemented to overcome or at least reduce severe convergence difficulties due to the damage initiation, which is realized by applying viscous regularization to the constitutive equations of the traction-separation law.

Further on, the initial and damaged material behavior of discrete cracks and delamination are discussed in Sections 3.3.1 and 3.3.2, respectively.

The implemented cohesive material behavior of discrete cracks leads to a quasi-brittle system behavior, which was demonstrated by Blank et al. [5] with a comparison of an FE approach in conjunction with a traction-separation law and an analytical approach of predicted bending strength of GLT beams. The initiated damage represents a fracture process zone that accounts for all weakening, e.g. micro-cracking that initiates softening of a fracture process zone in the framework of non-linear fracture mechanics. The contrary is a brittle behavior, which would not consider damage evolution (softening) and immediately lead to no transmitted traction. The assumption of a crack plane with a normal vector parallel to X-direction is justified by the fact that the main stress direction is mainly aligned to this direction in the range of the maximum bending moment. However, experimental results show indeed pronounced horizontal crack propagation [23, 39] (see Fig. 2.4d), but practically no delamination of timber boards. The difference between the crack path in reality and the model needs to be considered by adjusted fracture energy and strength values. Nevertheless the delamination is implemented to enable

in a simplified way that vertical cracks in adjacent timber boards, which are not at the same position in X-direction, are allowed to merge.

The cohesive material behavior governs the separation and stress transmission between the two opposite surfaces of a crack plane. The separation is described by a separation vector $\boldsymbol{\delta}$ with the components δ_n, δ_p, and δ_q, which reads as:

$$\boldsymbol{\delta} = \delta_\mathrm{n}\,\mathbf{e}_\mathrm{n} + \delta_\mathrm{p}\,\mathbf{e}_\mathrm{p} + \delta_\mathrm{q}\,\mathbf{e}_\mathrm{q}\,, \tag{3.12}$$

and corresponds to the stress transmission with the energetically conjugated nominal traction stress vector $\mathbf{t}$ with the components t_n, t_p, and t_q, which reads as:

$$\mathbf{t} = t_\mathrm{n}\,\mathbf{e}_\mathrm{n} + t_\mathrm{p}\,\mathbf{e}_\mathrm{p} + t_\mathrm{q}\,\mathbf{e}_\mathrm{q}\,, \tag{3.13}$$

where $\mathbf{e}_\mathrm{n}$, $\mathbf{e}_\mathrm{p}$, and $\mathbf{e}_\mathrm{q}$ stand for the unit vectors. In Eqs. (3.12) and (3.13) the unit vector $\mathbf{e}_\mathrm{n}$ is aligned in direction of the normal vector $\mathbf{n}$ of the crack plane and the two remaining unit vectors $\mathbf{e}_\mathrm{p}$ and $\mathbf{e}_\mathrm{q}$ lie in the crack plane. The nominal traction stress components t_n, t_p, and t_q depend only on the corresponding separation component δ_n, δ_p, and δ_q, respectively, which is described by the uncoupled cohesive stiffness tensor $\mathbf{K}$, which reads as:

$$\mathbf{K} = \begin{bmatrix} K_\mathrm{nn} & 0 & 0 \\ 0 & K_\mathrm{pp} & 0 \\ 0 & 0 & K_\mathrm{qq} \end{bmatrix}\,. \tag{3.14}$$

Finally, the linear elastic traction-separation law describes the constitutive relation of the nominal traction stress vector $\mathbf{t}$ and the separation vector $\boldsymbol{\delta}$ with the uncoupled cohesive stiffness tensor $\mathbf{K}$ from (3.14), which reads as:

$$\mathbf{t} = \mathbf{K} \cdot \boldsymbol{\delta}\,. \tag{3.15}$$

The damage initiation criterion f_init follows a maximum nominal stress criterion for the components of the nominal traction stress vector and reads as:

$$f_\mathrm{init} = \max\left\{ \frac{\langle t_\mathrm{n}\rangle}{t_\mathrm{n}^*}\,,\ \frac{t_\mathrm{p}}{t_\mathrm{p}^*}\,,\ \frac{t_\mathrm{q}}{t_\mathrm{q}^*} \right\} \geq 1\,, \tag{3.16}$$

where the angled brackets $\langle \cdot \rangle$ represent the Macaulay brackets and the superscript $*$ denotes the ultimate nominal stress component. The Macaulay brackets return non-zero values only in case of an inserted value greater or equal to zero, where a crack initiation is only considered for a nominal tensile stress t_n greater or equal to zero. The general formulation of the Macaulay brackets is:

$$\langle x \rangle = \begin{cases} x < 0: & 0 \\ x \geq 0: & x \end{cases}\,. \tag{3.17}$$

The damage evolution is governed by an energy based linear damage evolution law to define a degraded nominal traction stress vector $\bar{\mathbf{t}}$. Camanho and Dávila [10] describe the evolution of damage by an effective separation δ_m, which reads as:

$$\delta_\mathrm{m} = \sqrt{\langle \delta_\mathrm{n}\rangle^2 + \delta_\mathrm{p}^2 + \delta_\mathrm{q}^2}\,. \tag{3.18}$$

Equation (3.18) represents a modified norm of Eq. (3.12) and analog to that definition an effective nominal traction stress t_{m} and a degraded effective nominal traction stress $\bar{t}_{\mathrm{m}}$, as modified norms of Eq. (3.13), are defined, respectively:

$$t_{\mathrm{m}} = \sqrt{\langle t_{\mathrm{n}} \rangle^2 + t_{\mathrm{p}}^2 + t_{\mathrm{q}}^2}, \quad \bar{t}_{\mathrm{m}} = \sqrt{\langle \bar{t}_{\mathrm{n}} \rangle^2 + \bar{t}_{\mathrm{p}}^2 + \bar{t}_{\mathrm{q}}^2}. \tag{3.19}$$

Thereby a scalar damage variable D expresses the overall damage and degradation progress by taking the value zero at the initiation of damage and increasing monotonically until reaching one at the fully evolved damage, which is the end of stress transmission:

$$D \in [0,1] \quad \text{with} \quad D(k_0) = 0, \ D(k_{\mathrm{f}}) = 1 \quad \text{and} \quad \forall k \in \mathcal{I} : \ D(k) \leq D(k+1), \tag{3.20}$$

where k_0 and k_{f} stand for the load increment of damage initiation and fully evolved damage, respectively, $\mathcal{I}$ for the set of all load increments, and k for a specific load increment. The fracture energy G_{f} defines the linear behavior of the degradation and represents the dissipated energy in the damage progress, which corresponds to the area under the δ_{m}-$\bar{t}_{\mathrm{m}}$-curve (see Fig. 3.5). The δ_{m}-$\bar{t}_{\mathrm{m}}$-curves in Fig. 3.5 include the scalars $\delta_{\mathrm{m}}^{\circ}$ and t_{m}°, which denote the values of Eqs. (3.18) and (3.19)$_1$, respectively, at the increment of damage initiation. Depending on the modeling case whether discrete cracks or delamination is described with the traction-separation law (3.15) the δ_{m}-$\bar{t}_{\mathrm{m}}$-curve has a linear or bi-linear course, respectively (see Fig. 3.5a). The effective separation at fully evolved damage $\delta_{\mathrm{m,f}}$ is defined for both modeling cases by:

$$\delta_{\mathrm{m,f}} = \frac{2\,t_{\mathrm{m}}^{\circ}}{G_{\mathrm{f}}}. \tag{3.21}$$

The damage variable D is a function of the maximum effective separation $\delta_{\mathrm{m,max}}$, occurred up to the current load increment, which is different for each modeling case, where the general notation reads as:

$$D = f(\delta_{\mathrm{m,max}}). \tag{3.22}$$

In order to implement damage in the traction-separation law (3.15) a capacity matrix $\boldsymbol{C}$ is defined, which reads as:

$$\boldsymbol{C} = \begin{bmatrix} (1 - \widetilde{D}) & 0 & 0 \\ 0 & (1 - D) & 0 \\ 0 & 0 & (1 - D) \end{bmatrix} \quad \text{with} \quad \widetilde{D} = \begin{cases} t_{\mathrm{n}} < 0 : & 0 \\ t_{\mathrm{n}} \geq 0 : & D \end{cases}, \tag{3.23}$$

where $\widetilde{D}$ only accounts for damage in n-direction when t_{n} greater or equal to zero, with t_{n} from (3.13). The capacity matrix (3.23) gets multiplied to the left side of the traction-separation law (3.15), which leads to the degraded nominal traction stress vector $\bar{\mathbf{t}}$ and reads as:

$$\bar{\mathbf{t}} = \boldsymbol{C} \cdot \mathbf{t} = \boldsymbol{C} \cdot \mathbf{K} \cdot \boldsymbol{\delta}. \tag{3.24}$$

The stabilization scheme uses a viscous regularization of the damage variable D from (3.22) to encounter occurring convergence difficulties by permitting a higher degraded nominal traction stress vector than from Eq. (3.24). This achieves a positive tangential stiffness matrix of the degraded cohesive material for sufficiently small time increments. For this purpose a viscous damage variable D_{v} is defined as a function of a viscosity parameter μ and the damage variable D from (3.22). The rate of the viscous damage variable $\dot{D}_{\mathrm{v}}$ is defined as:

$$\dot{D}_{\mathrm{v}} = \frac{1}{\mu} \left(D - D_{\mathrm{v}} \right). \tag{3.25}$$
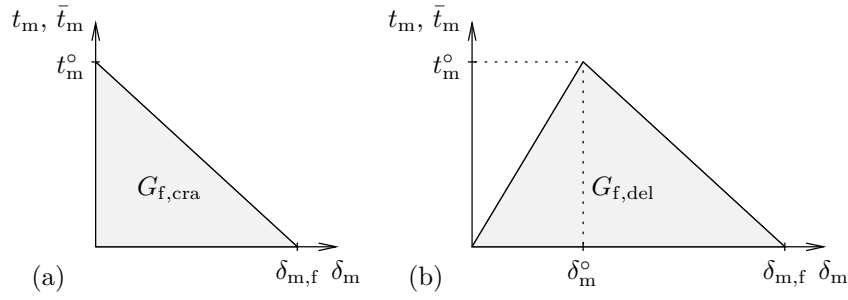
Fig. 3.5: Fracture energy G_f of traction-separation law with effective separation δ_m and effective nominal traction stress $\bar{t}_\mathrm{m}$ for (a) discrete cracks with and (b) delamination (redrawn with adapted notation from [1]).

The solution of the first order inhomogeneous linear differential equation (3.25) reads as:

$$D_\mathrm{v} = D \left[1 - \exp\left(-\frac{t}{\mu} \right) \right] , \tag{3.26}$$

where t stands for the accumulation of the time increments, which define the load increments, after the damage initiation. Equation (3.26) indicates that the viscosity parameter μ needs to be small compared to the current time increments in order to have an viscous effect on D. The response of the viscous system relaxes for $t/\mu \to \infty$ to the same as the inviscid response. The viscous capacity matrix $\boldsymbol{C}_\mathrm{v}$ is defined analog to the capacity matrix $\boldsymbol{C}$ from (3.23) and reads as:

$$\boldsymbol{C}_\mathrm{v} = \begin{bmatrix} (1 - \widetilde{D}_\mathrm{v}) & 0 & 0 \\ 0 & (1 - D_\mathrm{v}) & 0 \\ 0 & 0 & (1 - D_\mathrm{v}) \end{bmatrix} \quad \text{with} \quad \widetilde{D}_\mathrm{v} = \begin{cases} t_\mathrm{n} < 0: & 0 \\ t_\mathrm{n} \geq 0: & D_\mathrm{v} \end{cases} . \tag{3.27}$$

The modified traction-separation law accounts for stiffness degradation by a viscous capacity matrix $\boldsymbol{C}_\mathrm{v}$ from (3.27) that gets multiplied to the left side of the traction-separation law (3.15), which leads to the viscous degraded nominal traction stress vector $\bar{\mathbf{t}}_\mathrm{v}$ and reads as:

$$\bar{\mathbf{t}}_\mathrm{v} = \boldsymbol{C}_\mathrm{v} \cdot \mathbf{t} = \boldsymbol{C}_\mathrm{v} \cdot \mathbf{K} \cdot \boldsymbol{\delta} . \tag{3.28}$$

3.3.1 Discrete cracks

The material behavior of a finite element prior to damage initiation is determined by the constitutive material model of timber boards (see Section 3.2.1). A discrete crack starts or propagates with the initiation of damage within a region r that uses enriched finite elements in accordance to XFEM. Thereby each discrete crack origins from crack initiation and propagates due to crack growth. The evolution of damage is governed by the modified traction-separation law from (3.28) in accordance to the cohesive-segment method. The coefficients K_nn, K_pp, and K_qq of the uncoupled cohesive stiffness tensor $\mathbf{K}$ from (3.15) get calculated by Abaqus [1] from the material properties of the assigned elasticity tensor $\mathbb{C}_s$ from (3.10) of a section s. A region can be a part of a section or contain multiple parts of different sections up to multiple entire sections.

The initiation of damage is controlled by a user damage initiation subroutine, the so-called `udmgini`, which holds a modified damage initiation criterion of (3.16) and the direction assignment of the normal vector $\mathbf{n}$ of the crack plane. The modified damage initiation criterion f^*_init verifies for each enriched finite element $\tilde{e}$ the arithmetic mean value of all integration point stress

values $\mathrm{mean}\big(\sigma_{\mathrm{LL}}^{\tilde{e}}\big)$ and sets it in relation to a prescribed tensile strength $f_{\mathrm{t},0,s}$ of the corresponding timber board section s, both stress and strength have an orientation aligned in direction of the unit vector $\mathbf{e}_{\mathrm{L}}$ in fiber longitudinal direction, which reads as:

$$f_{\mathrm{init}}^* = \frac{\mathrm{mean}\big(\sigma_{\mathrm{LL}}^{\tilde{e}}\big)}{f_{\mathrm{t},0,s}} \geq 1\,, \tag{3.29}$$

additionally, the normal vector $\mathbf{n}$ of the crack plane is aligned in direction of the unit vector $\mathbf{e}_{\mathrm{L}}$ in fiber longitudinal direction, which ensures a crack plane perpendicular to the longitudinal X-direction of the GLT beam. Criterion (3.29) accounts for the crack initiation and crack growth in conjunction with the tolerance f_{tol} and $f_{\mathrm{tol,g}}$, respectively. If the criterion (3.29) is satisfied in a region r, the load increment size gets reduced until for all enriched finite elements the criterion is within the corresponding tolerance f_{tol} or $f_{\mathrm{tol,g}}$. The increment size reduction is iterative and is aborted after a given number of iterations, at which the tolerance is ignored and crack initiation or propagation occurs in all elements that still satisfy criterion (3.29).

The crack initiation is only possible in a region without an initiated damage or a still evolving damage. In other words, the initiation of a discrete crack in a region requires no initiated damage in that region at all or a damage variable of one for all enriched finite elements with initiated damage. If criterion (3.29) is satisfied for at least a single enriched finite element within a region and obeys the tolerance f_{tol}:

$$1.0 \leq f_{\mathrm{init}}^* \leq 1.0 + f_{\mathrm{tol}} \quad \text{with} \quad f_{\mathrm{tol}} = 0.1\,\text{\textperthousand}\,, \tag{3.30}$$

or the number of reduction iterations is exceeded, a crack initiation occurs. The initiation of multiple cracks at once is possible, hence the tolerance f_{tol} is quite small compared to one. It is preferred to have a crack initiation only in a single enriched finite element within one region rather than in multiple finite elements, because the crack growth may lead to numerical difficulties.

The crack growth is only possible in crack direction of an already initiated crack within a region. In other words, enriched finite elements of a region that are directly adjacent to an edge of the initiated crack in this region have the possibility to experience crack growth. If the criterion (3.29) is satisfied for at least a single enriched finite element within a region and obeys the tolerance $f_{\mathrm{tol,g}}$:

$$1.0 \leq f_{\mathrm{init}}^* \leq 1.0 + f_{\mathrm{tol,g}} \quad \text{with} \quad f_{\mathrm{tol,g}} = 0.3\,\%\,, \tag{3.31}$$

or the number of reduction iterations is exceeded, crack growth occurs.

The evolution of damage is governed by the damage variable D according to the effective separation at fully evolved damage $\delta_{\mathrm{m,f}}$ from (3.21) with the specified fracture energy $G_{\mathrm{f},r}$ and the linear course of the corresponding δ_{m}-$\bar{t}_{\mathrm{m}}$-curve (see Fig. 3.5a). The function of the damage variable D is not given in the documentation of Abaqus [1] but it is a function of the maximum effective separation $\delta_{\mathrm{m,max}}$, as given in Eq. (3.22). The fracture energy $G_{\mathrm{f,cra},r}$ inherits the elastic energy of a strain experiencing element at the crack initiation, which may lead to the so-called snap-back phenomenon with convergence difficulties, where the separation and traction would both decrease. The viscous stabilization scheme is realized by the damage variable D_v from (3.26) that uses the viscosity parameter μ_r.

Finally, the behavior of a discrete crack within a region is described by the crack initiation carried out under consideration of Eq. (3.29) and tolerance criterion (3.30), the crack growth according to Eq. (3.29) and growth tolerance criterion (3.31), and the viscous damage evolution of a crack by the modified traction-separation law (3.28). Necessary parameters that need to be specified for discrete cracks are the elasticity tensor $\mathbb{C}_s$, tensile strength $f_{\mathrm{t},0,s}$, fracture energy $G_{\mathrm{f,cra},r}$, and viscosity parameter μ_r.

3.3.2 Delamination

The cohesive material behavior of a contact constraint point is defined by the modified traction-separation law (3.28) for behavior prior and post the damage initiation. The delamination joint originates from a damage initiation and propagates due to damage evolution. The coefficients K_{nn}, K_{pp}, and K_{qq} of the uncoupled cohesive stiffness tensor $\mathbf{K}$ from (3.15) are the default contact penalty values of Abaqus [1] based on the assigned elasticity tensor $\mathbb{C}_s$ from (3.10) of a section s.

The damage initiation is according to criterion (3.16), with strengths t_n^*, t_p^* and t_q^*, in direction of the corresponding unit vector $\mathbf{e}_n$, $\mathbf{e}_p$, and $\mathbf{e}_q$, respectively, where $\mathbf{e}_n$ is aligned in direction of the normal vector $\mathbf{n}$ of the crack plane and the remaining two unit vectors lie in the crack plane.

The damage evolution is governed by the function of the damage variable D according to the effective separation at fully evolved damage $\delta_{m,f}$ from (3.21) with the specified fracture energy $G_{f,del}$ and the bi-linear course of the corresponding δ_m-$\bar{t}_m$-curve (see Fig. 3.5b). The function of the damage variable D with $\delta_{m,f}$ from (3.21) and the dependency of the maximum effective separation $\delta_{m,max}$, occurred up to the current load increment, reads as:

$$D = \frac{\delta_{m,f}\ (\delta_{m,max} - \delta_m^\circ)}{\delta_{m,max}\ (\delta_{m,f} - \delta_m^\circ)}\,, \tag{3.32}$$

where δ_m° stands for the effective separation at the increment of damage initiation. The viscous stabilization scheme is realized by the damage variable D_v from (3.26) that uses the viscosity parameter μ.

Finally, the behavior of the delamination joint between timber boards is described by the damage initiation according to criterion (3.16) and the damage evolution by the modified traction-separation law (3.28). Necessary parameters that need to be specified for delamination are the elasticity tensor $\mathbb{C}_s$, the strengths t_n^*, t_p^*, and t_q^*, fracture energy $G_{f,del}$, and viscosity parameter μ.

3.4 Model setup

The previously described methods and properties as well as the experimental setup (see Fig. 3.1) are now implemented in the following section. To determine the load-bearing capacity with failure mechanisms while taking into account knot groups and quasi-brittle material failure, the computational modeling approach requires the definition of:

- geometry and assignment of constitutive models,
- fracture and delamination models,
- boundary conditions,
- solver settings, and
- a postprocessing approach to obtain the load-bearing capacity.

3.4.1 Geometry and assignment of constitutive models

Figure 3.6a shows the model, which consists of the GLT beam, the load distribution construction and the two bearing plates. Dimensions and positions of all model parts are shown in the sketch. The timber board thickness d is constant, thus, the number of timber boards n defines the total height h of the GLT beam. The lengths ℓ_1, ℓ_2, and ℓ_3 define the position of the bearings and the load application. The bearing plates have a length $\ell_p = 100\,\text{mm}$ and the width corresponds to the GLT beam width b. The effective strength properties of knot and clear wood sections are defined as section-wise constant through the use of the strength profiles, thus, each such section should be assigned its own enrichment region. As the number of enriched sections for XFEM is limited (see Section 3.4.2), the region to which the enrichment properties are assigned cannot

Fig. 3.6: Assembled geometry with (a) definition of measurements, (b) exemplary effective enriched volume and (c) exemplary individual mechanical properties for timber board sections, and (d) symmetry characteristics.

cover the entire GLT beam. Therefore, the region is defined as shown in Fig. 3.6a with height h_{e}, width b and length ℓ_{e}, which is an extension of the region with constant bending moment by length e.

To correctly reproduce the experiments, the beams' morphological characteristics must be properly considered during the assembly. Thus, the position of the individual boards with previously determined clear wood and knot sections (see Section 2.2) is defined by the experimental setup. Figure 3.6b shows an exemplary section arrangement illustrating that the effective enriched volume always exceeds the specified one and Fig. 3.6c shows the varying local material properties. The material model of those sections was described in Section 3.2.1. The load distribution construction consists of a bar, which is tied to two load distribution plates via two line connections, allowing the connection to freely rotate about the Y-axis. The material properties of the load distribution construction and the bearing plates, respectively, were defined in Section 3.2.2.

While the geometry is symmetric in both X- and Y-directions, the distribution of material properties is symmetric only in Y-direction. Thus, symmetry characteristics can only be utilized in Y-direction by considering one half of the experimental setup (half the thickness), which is described in more detail in Section 3.4.3.

3.4.2 Fracture and delamination models

The discretization generates an FE mesh that reduces the infinite number of points within the volume or on the surface of the model to the number of the integration points within each finite element. The approach uses eight-node brick elements with eight integration points. Full integration is used to avoid zero energy modes of enriched elements that experience fracture. The used version of Abaqus is limited to linear shape functions for eight-node brick elements in conjunction with the application of XFEM [1]. A shape function of linear order describes the strain field of an element by tri-linear functions and generally leads to the need of a finer discretization than the use of a shape function with higher order. As preparation predefined lines are integrated in the FE mesh to later on assign interaction and boundary conditions to the nodes along the lines. This concerns the lines of contact between the load distribution plates and the bar of the load distribution construction (see *Line a* in Fig. 3.7). Further lines parallel to the Y-direction are prepared to prescribe boundary conditions at the bottom middle of the load distribution bar, in the middle of the first bearing plate in X-direction at the timber board surface, and on the top middle of the bearing plates (see *Lines b*, *c*, and *d* in Fig. 3.7, respectively).

Discrete cracks in a region r are realized by applying XFEM in conjunction with the cohesive-segment method, which was described in Section 3.3.1. The used version of Abaqus 2019 is limited to a maximum total number of 100 regions [1]. Each region is limited to experience active cracks only due to the instant crack initiation in one load increment. This means that after a crack initiation within a region, all cracked elements need to have fully evolved damage, expressed by the viscous damage variable D_v from Eq. (3.26) equaling one. In the present thesis the dimensions of an enriched region are identical to the corresponding timber board section s. Due to the mentioned limited number of regions, not each section is necessarily an enriched region. All sections within or intersecting the specified enriched volume are enriched regions (see Fig. 3.6a) and form the effective enriched volume (see Fig. 3.6b). A fully cracked finite element may enable the two independently moving parts to encounter contact again, therefore a pressure-overclosure relation is assigned to the crack surfaces with hard contact characteristics. The formulation of contact is in accordance to the small-sliding formulation of Abaqus [1], where it is assumed that all separated nodes only get back in contact within a small surface area around their initial position. The formulation is enforced by the augmented Lagrange method.

Delamination of adjacent boards is realized by defining cohesive interaction properties, which was described in Section 3.3.2. The corresponding surfaces are denoted in Fig. 3.7 as *Surface Type 1*. A surface-to-surface discretization with a small-sliding formulation from Abaqus [1] is used, which was briefly described in the previous paragraph. The primary surface is always assigned to the bottom timber board. Timber boards that experienced full delamination of their surfaces may encounter contact again, therefore hard contact characteristics are modeled analogous to the previous paragraph.

The interaction between the timber boards and the plates is defined by a surface-to-surface discretization with a finite-sliding formulation from Abaqus [1], where arbitrary motion between nodes of initial contact is allowed. The corresponding surfaces are marked in Fig. 3.7 as *Surface Type 2*. The primary surface is always assigned to the timber board. The contact properties are defined as pressure-overclosure relation with hard contact characteristics, which are enforced by the augmented Lagrange method, for interactions perpendicular to the surfaces and as frictionless for interactions in plane of the surfaces.
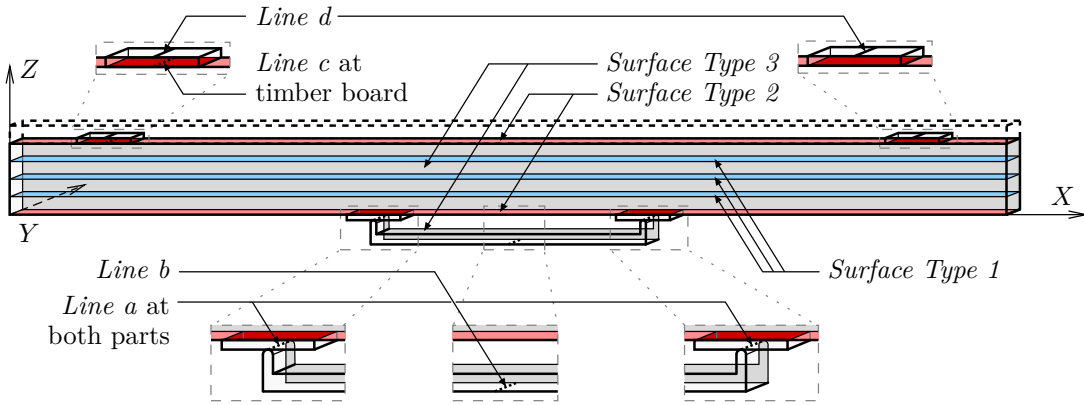
Fig. 3.7: Definition of *Line a* to *d* to prescribe boundary conditions, *Surface Type 1* and *2* to implement interactions, and *Surface Type 3* to prescribe boundary conditions due to exploitation of symmetry.

3.4.3 Boundary conditions

Constraints prescribe the relation or displacement of nodes created by the discretization. They account for the load, bearing, exploitation of symmetry characteristics, and tying.

The model is loaded in a displacement controlled manner with a load distribution construction. The corresponding distribution bar is tied to the two distribution plates along the nodes at the prepared *Line a* (see Fig. 3.7). An applied displacement represents the load and is prescribed along the nodes at the prepared *Line b* at the bottom of the load distribution construction (see Fig. 3.7). In order to cover non-linear behavior the applied displacement is applied in displacement increments, analogous to the load increments from Section 3.1.3. The vertical displacement w is controlled by the displacement of the initial increment k_0 and the total applied displacement increment k_e, which both read as:

$$w(k_0) = 0, \quad w(k_\mathrm{e}) = w^*_\mathrm{load}, \tag{3.33}$$

where w^*_load denotes the total applied displacement. Additionally, these nodes have the constant longitudinal displacement u, defined for the two increments k_0 and k_e, which reads as:

$$u(k_0) = 0, \quad u(k_\mathrm{e}) = 0. \tag{3.34}$$

The bearing is provided by constraining the displacement of the GLT beam in longitudinal direction u and in vertical direction w, those constraints stay constant during the loading and are defined for the two displacement increments k_0 and k_e. The displacement u is prescribed at one bearing along the prepared nodes of *Line c* on the top timber board in the middle of the first bearing plate in X-direction (see Fig. 3.7), which reads as:

$$u(k_0) = u(k_\mathrm{e}) = 0. \tag{3.35}$$

The displacements u, v, and w is prescribed at both bearings along the prepared nodes of *Line d* on top of the bearing plates (see Fig. 3.7), which read as:

$$u(k_0) = u(k_\mathrm{e}) = 0, \quad v(k_0) = v(k_\mathrm{e}) = 0, \quad \text{and} \quad w(k_0) = w(k_\mathrm{e}) = 0, \tag{3.36}$$

thus each baring plate is able to rotate around the Y-axis at the constrained nodes.

The exploitation of the symmetry characteristics has two requirements. First, the displacement in cross direction v of nodes in the plane of symmetry needs to be constrained, Fig. 3.7 shows the constrained *Surface Type 3* corresponding to the GLT beam and at the load distribution bar. Second, the constraints need to be constant, which is achieved by defining the two displacement increments k_0 and k_e, which reads as:

$$v(k_0) = v(k_e) = 0 \,. \tag{3.37}$$

The distribution plates of the load distribution construction inherit the constraints from (3.37) due to the tying along *Line a* (see Fig. 3.7). Together with the prescribed constraints of the applied displacement from (3.33) and (3.34) the distribution of the applied displacement is realized, whereby each plate is able to tilt around the Y-axis at the tied nodes.

3.4.4 Solver settings

The computational model describes a non-linear static analysis and obtains the solution with an incremental-iterative method, which is the default method in Abaqus [1]. The total applied displacement w_{sim}^* from (3.33) represents the load and is applied in load increments according to a fictitious time scale that reaches from zero at the initiation to one at the fully applied load. The size of the initial time increment is defined as 0.01, which results in an initially applied displacement of $w_{\mathrm{sim}}^*/100$. The further time increment size is defined by an empirical algorithm implemented in Abaqus [1] and may vary between a maximum size of 0.01 and minimum size of 1×10^{-22}. The analysis is limited to a maximum of 400 load increments. The selected parameters of the default convergence settings in Abaqus [1] are modified in the following manner:

- "I_0, number of equilibrium iterations (without severe discontinuities) after which the check is made whether the residuals are increasing in two consecutive iterations [. . .]"[1] is set to $I_0 = 8$,
- "I_R, number of consecutive equilibrium iterations (without severe discontinuities) at which logarithmic rate of convergence check begins [. . .]"[1] is set to $I_R = 10$,
- "I_A, maximum number of attempts allowed for an increment [. . .]"[1] is set to $I_A = 60$.

3.4.5 Load-bearing capacity

The load-bearing capacity F_{sim}^* is obtained in a postprocessing approach by a load decline criterion f_{cri} and by satisfying two energy criteria f_{cri,E_1} and f_{cri,E_2}. Here, the evaluation is done in each displacement increment k. The load decline criterion f_{cri} checks the progressing load of a relative decline d_{sim} to determine a load-bearing capacity candidate $\widetilde{F}_{\mathrm{sim}}^*$. This criterion uses the ratio of the current load $F_{\mathrm{sim},k}$ over the maximum load up to this point $F_{k,\max} = \max\left(F_{\mathrm{sim},i}\right)$ for $i \in [1,k]$ and the relative decline, which reads as:

$$f_{\mathrm{cri},k} = \left(1 - \frac{F_{\mathrm{sim},k}}{F_{k,\max}}\right) \geq d_{\mathrm{sim}} \quad \text{with} \quad F_{k,\max} = \max\left(F_{\mathrm{sim},i}\right) \quad \forall i \in [1,k] \text{ and } \forall k \in \mathcal{I}, \tag{3.38}$$

where $\mathcal{I}$ stands for the set of all analyzed displacement increments. The first displacement increment that satisfies the criterion (3.38) with the relative decline $d_{\mathrm{sim}} = 3\,\%$ is denoted as k_{c} and defines the load-bearing capacity candidate:

$$\widetilde{F}_{\mathrm{sim}}^* = F_{k_{\mathrm{c}},\max} \quad \text{with} \quad k_{\mathrm{f}} = k \quad \text{for the first } k \text{ that satisfies:} \quad f_{\mathrm{cri},k} \geq 0.03 \,. \tag{3.39}$$

Subsequently, the two energy criteria need to be satisfied for $\widetilde{F}_{\text{sim}}^*$ from (3.39) in order to determine the load-bearing capacity. Abaqus [1] defines for each increment a total energy balance E_{ETOTAL}, a total strain energy E_{ALLIE}, and the energy due to viscous regularization of cohesive material behavior in contacts E_{ALLCD} and discrete cracks that are realized with XFEM E_{ALLVD}. The first energy criterion $f_{\text{cri,E}_1}$ compares the ratio of the total energy balance over the total strain energy to a quite low threshold, compared to one, which reads as:

$$f_{\text{cri,E}_1,k_c} = \frac{E_{\text{ETOTAL},k_c}}{E_{\text{ALLIE},k_c}} \leq 0.01 \,. \tag{3.40}$$

The second criterion $f_{\text{cri,E}_2}$ considers the energies due to viscous regularization, where this serves in relation to the difference of total strain energy and energy due to viscous regularization of contact, which reads as:

$$f_{\text{cri,E}_2,k_c} = \frac{E_{\text{ALLCD},k_c} + E_{\text{ALLVD},k_c}}{E_{\text{ALLIE},k_c} - E_{\text{ALLCD},k_c}} \leq 0.05 \,. \tag{3.41}$$

The basis is the difference because the total strain energy already accounts for the energy due to viscous regularization of contact. Finally the load-bearing capacity is determined when a candidate is found in accordance to criterion (3.38) and Eq. (3.39) that satisfied the two energy criteria (3.40) and (3.41):

$$F_{\text{sim}}^* = \widetilde{F}_{\text{sim}}^* \quad \text{for} \quad f_{\text{load},k_c} \geq 0.03 \ \text{and} \ f_{\text{cri,E}_1,k_c} \leq 0.01 \ \text{and} \ f_{\text{cri,E}_2,k_c} \leq 0.05 \,. \tag{3.42}$$

For the case that no load-bearing capacity is determined for a beam in accordance to Eq. (3.42), the simulation is disregarded.

Chapter 4

Application of the modeling approach

In the following the proposed modeling approach from Chapter 3 is applied to the presented experimental setup from Section 2.1. In this thesis the four beam types, A/T14-4, B/T22-4, D/T14-10 and E/T22-10, with a total of 38 beams are examined. All beam types consist of ten individual beams with the exception of beam type E/T22-10, where only eight beams are considered due to the available data of the knot morphology. The well-known knot morphology is described by the individual stiffness profiles and the selected strength profiles SP3 and SP4 of each timber board (presented in Section 2.2). Exemplary stiffness and strength profiles are illustrated in Figs. 2.5f and 2.5g, respectively. The beam types distinguish two sizes, regarding the beam length and height, where beam types A/T14-4 and B/T22-4 are the smaller size with $\ell = 2\,700$ mm and $n = 4$ timber boards and beam types D/T14-10 and E/T22-10 are the larger size with $\ell = 5\,400$ mm and $n = 10$ timber boards (see Figs. 2.1a and 2.1c, respectively). Additionally, they cover two strength classes, beam types A/T14-4 and D/T14-10 regard to strength class T14 and beam types B/T22-4 and E/T22-10 to T22 (see Table 2.1). The beam dimensions are given in Table 2.1 and correspond to the definitions of the modeling approach in Fig. 3.6 and the experimental setup in Fig. 2.1.

The following studies use the definition of the enriched volume from Fig. 3.6a. Each section that lies within or intersects the enriched volume becomes an enriched region (see Section 3.4.2). Due to the limitation of 100 enriched regions, the two beam sizes have different enriched volumes. Further, a limitation on the stiffness and strength profile values is applied. The stiffness profiles have a lower limit of the effective longitudinal stiffness parameter $E_{\mathrm{L,min}} = 1\,000$ N/mm^2. The strength profiles have individual upper and lower limits, which are stated in each study.

For the analysis the commercial FE software Abaqus 2019 is used. The execution was carried out on a server cluster with three nodes, each consisting of 24 cores with 2.5 GHz clock speed and 256 GByte memory. The computation time of one set with a total of 38 simulations had an average computation time of about 4 h and 55 min, with each simulation using four cores. In comparison to the overall average the simulations of the smaller beam sizes had lower average computation times of about 1 h and 55 min, whereas the simulations of the larger beam size had an significantly higher average computation time of about 8 h and 15 min. All periods were rounded in 5 min steps and the simulations had three finite elements per timber board height.

4.1 Dependency on mesh size

This study aims to determine an efficient FE mesh size as a balance between sufficiently accurate results and computational time required. Here, the used computational modeling approach differs from the one presented in Chapter 3 to determine the impact of a different crack growth evaluation and a different contact enforcement method after delamination on the load-bearing capacity. The evaluation for the crack initiation due to the implementation of XFEM in Abaqus 2019 is always determined by the finite element's arithmetic mean value, the type of the crack growth evaluation can be selected. First, the stress evaluation to consider crack growth in a neighboring

Tab. 4.1: Mesh dependency sets with discrete crack parameters: tensile strength in fiber direction $f_{t,0}$, fracture energy $G_{f,cra}$ and delamination parameters: out-of-plane strength f_n^*, in-plane strengths $f_p^* = f_q^*$, fracture energy $G_{f,del}$.

Material parameters for	Sets	discrete cracks[a]		delamination[a]		
		$f_{t,0}$[b] $[\mathrm{N/mm^2}]$	$G_{f,cra}$ $[\mathrm{N\,mm/mm^2}]$	f_n^* $[\mathrm{N/mm^2}]$	$f_p^* = f_q^*$ $[\mathrm{N/mm^2}]$	$G_{f,del}$ $[\mathrm{N\,mm/mm^2}]$
Sets with 1–5 finite elements per timber board height	M1–M5	SP3	20.0	100.0	10.0	1.0

[a] Applied viscosity parameter $\mu = 1 \times 10^{-6}$ for discrete cracks and delamination.
[b] Strength profile from Section 2.2 limited by: $f_{t,0,min} = 10\,\mathrm{N/mm^2}$ and $f_{t,0,max} = 70\,\mathrm{N/mm^2}$.

finite element uses the extrapolated stress at the adjoining crack front instead of the arithmetic mean of all integration points (described in Section 3.3.1). Second, the delamination contact enforcement method is a pressure-overclosure relationship instead of the augmented Lagrange method (described in Section 3.4.2). A later comparison of set M5 with a set that uses the settings of the proposed modeling approach (Chapter 3) showed no significant impact due to the different settings.

The study consists of the sets M1 to M5 with a total number of five sets and covers coarse and continuously refined FE mesh sizes. The number of the set identification corresponds to the number of finite elements per timber board height, thus sets M1 and M5 represent the coarsest and finest FE mesh, respectively. Table 4.1 summarizes the used sets in the first two columns. The applied downsizing of the FE mesh affects all three dimensions. The following two paragraphs define the modeling parameters and the enriched volume before presenting and discussing the results.

The modeling parameters concern the initiation and evolution of discrete cracks and delamination. In this study all timber boards use the strength profile SP3 to define the strength in each section. The lower limit within a knot group section is defined by the minimum strength $f_{t,0,min} = 10\,\mathrm{N/mm^2}$. The upper limit within a clear wood or knot group section is set by the maximum strength $f_{t,0,max} = 70\,\mathrm{N/mm^2}$. The evolution of discrete cracks in timber boards is defined by a constant fracture energy $G_{f,cra} = 20.0\,\mathrm{N\,mm/mm^2}$. The parameters for the delamination of adjacent timber boards are constant. The assigned strengths of the maximum stress criterion are chosen to account for failure in-plane and exclude out-of-plane failures. Therefore, the strengths read as $f_n^* = 100\,\mathrm{N/mm^2}$ in out-of-plane direction and as $f_p^* = f_q^* = 10\,\mathrm{N/mm^2}$ in the two in-plane directions. The evolution of delamination is defined by the constant fracture energy $G_{f,del} = 1.0\,\mathrm{N\,mm/mm^2}$. Both, the evolution of discrete cracks and delamination, have a viscosity parameter $\mu = 1 \times 10^{-6}$. All parameters were established in preliminary simulations prior to the presented study and suggested promising results. The used model sets with the used material parameters are summarized in Table 4.1.

The enriched volume is assigned to the whole GLT beam for beam types A/T14-4 and B/T14-4, with $n = 4$ timber boards. Beam types D/T14-10 and E/T22-10, with $n = 10$ timber boards, use all available 100 enriched regions. The assignment starts from the top within the range of the enriched length $\ell_e = 2\,980\,\mathrm{mm}$, which results in an enriched height h_e of at least 198 mm, corresponding to at least the six upper timber boards. The enriched width is the modeled half beam width $b/2 = 45\,\mathrm{mm}$

The result of the simulations is the load-bearing capacity, which is determined according to criterion (3.42) in conjunction with a load drop of $d_{sim} = 3\,\%$. In order to evaluate the convergence behavior of the mesh sizes the load-bearing capacity of each set is normalized by the corresponding result of set M5. Figure 4.1 illustrates the convergence behavior for all four beam
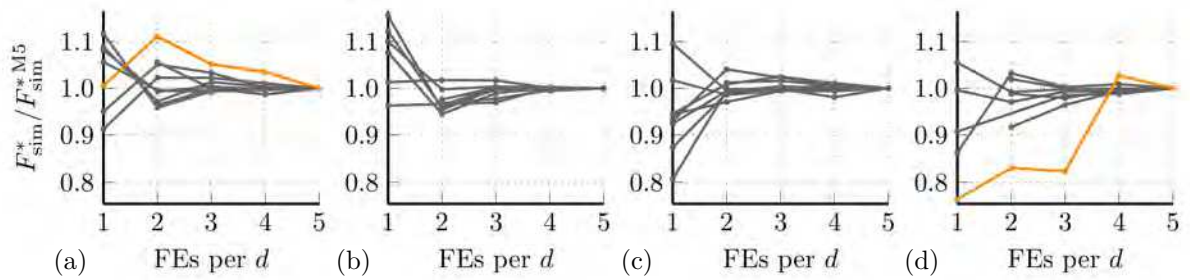
Fig. 4.1: Mesh size dependency of the load-bearing capacity normalized by set M5 for one to five finite elements per timber board height d of beam types: (a) A/T14-4, (b) B/T22-4, (c) D/T14-10, and (d) E/T22-10; *orange* color marks outliers with at least 4 % deviation in set M3.

types, where the horizontal axis shows the number of finite elements per timber board height and the vertical axis the individual load-bearing capacity that is normalized by the corresponding value in set M5. About a third of the simulated beams in set M1 fail to determine the load-bearing capacity, hence their results are omitted. Table 4.2 gives an overview for the reasons why the determination failed.

Set M3 shows good results by deviating less than 4 % for almost all simulations except for two, which identifies those simulated beams as outliers. Figures 4.1a and 4.1d show the outlier of beam type A/T14-4 and E/T22-10, respectively. Table 4.3 gives the extreme values of the normalized load-bearing capacities for each set with the distinction of two groups that include or exclude outliers. In set M3 the normalized result of the outlier of beam type A/T14-4 deviates about 6 % and the one of beam type E/T22-10 deviates about 18 %. Table 4.4 shows the statistical overview of all simulations in set M3 with the distinction of two groups that include or exclude outliers. The influence of the outliers on the arithmetic mean due to the exclusion is about 0.5 % and about 2.1 % for beam types A/T14-4 and E/T22-10, respectively. The standard deviation has an increase of about 5.4 ‰ and about 4.4 % for beam types A/T14-4 and E/T22-10, respectively. Additionally, there are three predicted load-bearing capacities in set M3 that exceeded their corresponding experimental result from Section 2.1 by more than 20 %. The outliers are discussed in detail in the next two paragraphs, followed by the discussion of the three exceeding results.

The results of the beam type A/T14-4 outlier in Fig. 4.1a show a steep increase followed by an approximate linear decline. The failure is linked to the uppermost timber board that has a continuous clear wood section in the range of the maximum bending moment and beyond with the assigned maximum tensile strength $f_{t,0,max} = 70\,\text{N/mm}^2$ (see Table 4.1). The simulations with one and two finite elements per timber board height reach their load-bearing capacities due

Tab. 4.2: Quantity of set M1 simulations (one finite element per timber board height) that failed to determine the load-bearing capacity F_{sim}^* with the differentiation of different reasons.

Beam type	A/T14-4	B/T22-4	D/T14-10	E/T22-10	$\sum$
Determining $\widetilde{F}_{sim}^*$ failed[a]	–	–	–	1	1
Exceeding f_{c,E_1} [b]	2	1	2	2	7
Exceeding f_{c,E_1} and f_{c,E_2} [c]	1	3	–	–	4
$\sum$	3	4	2	3	12

[a] According to Eq. (3.39) and criterion (3.38).
[b] According to criterion (3.40).
[c] According to criteria (3.40) and (3.41), respectively.

Tab. 4.3: All mesh dependency sets in two groups: all simulations and simulations that deviate less than 4 %; each group with the quantity of considered simulations Qty as well as the minimum and maximum values of the load-bearing capacity normalized by set M5.

	All simulations			Deviation less than 4 %		
Set	Qty[a]	Min	Max	Qty[a]	Min	Max
M1	26	0.764	1.155	24	0.807	1.155
M2	37	0.831	1.111	35	0.917	1.056
M3	38	0.824	1.052	36	0.964	1.033
M4	38	0.981	1.035	36	0.981	1.011
M5	38	1.000	1.000	36	1.000	1.000

[a] Successful determination of F_{sim}^* in accordance to (3.42).

Tab. 4.4: Mesh dependency results of all beam types in two groups: all simulations and simulations that deviate less than 4 %; each group with the quantity of considered simulations Qty as well as the minimum, arithmetic mean, maximum values, and coefficient of variation CV of the load-bearing capacity normalized by set M5; *gray* values are not influenced by outliers.

	All simulations					Deviates less than 4 %				
Beam type	Qty[a]	Min	Mean	Max	CV	Qty[a]	Min	Mean	Max	CV
A/T14-4	10	0.992	1.010	1.052	0.020	9	0.992	1.006	1.033	0.014
B/T22-4	10	0.970	0.996	1.017	0.014		No outlier			
D/T14-10	10	0.994	1.005	1.025	0.012		No outlier			
E/T22-10	8	0.824	0.968	1.003	0.062	7	0.964	0.989	1.003	0.014
All beam types	38	0.824	0.996	1.052	0.033	36	0.964	1.000	1.033	0.014

[a] Successful determination of F_{sim}^* in accordance to (3.42).

to a discrete crack in the first knot group section outside the range of maximum bending moment. The occurrence of cracks outside of the maximum bending moment mismatches the observed failure mechanisms and is therefore assessed as not plausible failure. The approximate linear decline of the load-bearing capacity for three, four, and five finite elements per timber board height are related to the stress distribution and the crack initiation criterion. In accordance to the linear elasticity theory and the assigned homogeneous stiffness of each timber board section the stress distribution in *Z*-direction of the beam cross-section is linear with jumps at the top and bottom edge of each timber board. The crack initiation criterion (3.29) uses the arithmetic mean value that needs to exceed the strength in order to be satisfied. Therefore, a small finite element situated on the top timber board's outer surface reaches the tensile strength easier than a big finite element. The system failure is observed as quite brittle with the discrete crack in the clear wood section, hence a decreasing FE size leads to a deceasing load-bearing capacity.

The results of the beam type E/T22-10 outlier in Fig. 4.1d show a jump between three and four finite elements per timber board height, which is related to the change of the discrete crack position within the same knot group section. At the lower level the crack propagates within the top timber board at a position where the timber board beneath has a weakening knot group section. At the higher level the crack is reinforced by a clear wood section of the timber board beneath. The enabled stress redistribution leads to a significant higher load-bearing capacity.

The three predicted load-bearing capacities, which exceed the experimental results by more than 20 %, show similar features of the beam setup in the range of the maximum bending moment. Two beams have top timber boards without knot groups and one beam has only one knot group that is reinforced by an adjacent continuous clear wood section, therefore the tensile side is without or at least almost without weak points. Section 2.2 states the assumption that knots

below a certain knot size lead to only minor influences on the tensile strength. This might be true for a timber board with multiple knot groups but is not suitable for long clear wood sections. The existence of minor defects, like small knots, still results in a lower tensile strength, hence a reduction of the maximum strength to account for such defects in clear wood sections is reasonable. Those simulated beams achieve suitable results with a reduced maximum strength of $f_{t,0,max} = 55\,N/mm^2$. The reduction has no significant influence on the other simulations.

For further computations a number of three finite elements per timber board height is chosen with adequate results and reasonable computation time.

4.2 Validation of the model

The computational modeling approach from Chapter 3 is validated with the experimental study and the derived material properties from Chapter 2. The study uses three finite elements per timber board height and again the strength profile SP3 to define the strength in each section. The fracture energy for the evolution of discrete cracks as well as the parameters regarding the initiation and evolution of delamination are chosen from preliminary simulations. Table 4.5 summarizes the used parameters. The sensitivity of the load-bearing capacity in regard to the implemented delamination as well as the governing initiation and evolution parameters of the delamination and discrete cracks is studied in Section 4.3. Next, the dimensions of the enriched volumes are described before the system-related as well as effective material-related results and the observed failure mechanisms are presented and discussed, in Section 4.2.1 and Section 4.2.2, respectively.

The enriched volume deviates for the beam types D/T14-10 and E/T22-10 from the volume used in the mesh dependency study (Section 4.1). For beam types D/T14-10 and E/T22-10, with $n = 10$ timber boards, the enriched length is enlarged to $\ell_e = 3\,280\,mm$ and instead of assigning all 100 available regions from the top to the bottom the enriched height is always $h_e = 198\,mm$, corresponding to the top six timber boards. The enriched width stays for all beam types unchanged and is defined as the modeled half beam width $b/2 = 45\,mm$. For beam types A/T14-4 and B/T22-4, with $n = 4$ timber boards, the enriched volume stays unchanged and is assigned to the whole GLT beam.

Tab. 4.5: Validation set with discrete crack parameters: tensile strength in fiber direction $f_{t,0}$, fracture energy $G_{f,cra}$ and delamination parameters: out-of-plane strength f_n^*, in-plane strengths $f_p^* = f_q^*$, fracture energy $G_{f,del}$.

Material parameters for	Set	discrete cracks[a]		delamination[a]		
		$f_{t,0}$[b] $[N/mm^2]$	$G_{f,cra}$ $[N\,mm/mm^2]$	f_n^* $[N/mm^2]$	$f_p^* = f_q^*$ $[N/mm^2]$	$G_{f,del}$ $[N\,mm/mm^2]$
Parameters for validation	V1	SP3	35.0	100.0	10.0	1.0

[a] Applied viscosity parameter $\mu = 1 \times 10^{-6}$ for discrete cracks and delamination.
[b] Strength profile from Section 2.2 limited by: $f_{t,0,min} = 10\,N/mm^2$ and $f_{t,0,max} = 55\,N/mm^2$.

4.2.1 System-related and effective material-related results

System-related results are the system-related stiffness k_{sim} and the load-bearing capacity F_{sim}^* of all simulations of all four beam types. The predicted system-related stiffness is determined in analogy to the experimental study (see Section 2.1) by a linear regression of the load-displacement curve in the range of $10\,\%$ and $40\,\%$ of F_{sim}^*, resulting in $k_{\text{sim}} = \Delta F_{\text{sim}}/\Delta w_{\text{sim}}$. The predicted load-bearing capacity is determined by Eq. (3.42). Material-related effective results are derived from the system-related ones in the same manner as in the experimental study (Section 2.1) with Eq. $(2.1)_2$ for the predicted material-related effective modulus of elasticity $E_{\text{GLT,sim}}$ and Eq. $(2.1)_1$ for the predicted bending strength $f_{\text{b,sim}}$. The bending strength is therefore determined under the same assumptions as discussed in Section 2.1. In the following paragraphs the system-related results are shown before the material-related results and results of modeling approaches from literature.

Figure 4.2 shows the system-related stiffness k and the load-bearing capacity F^* of the predicted vs. the experimental results. Table 4.6 gives the data for the predicted results and Table 4.7 for the predicted results normalized by the experimental results. The predicted system-related stiffness generally underestimates the experimental results, however their coefficient of determination is quite high with a value of $R^2 = 0.91$. The underestimation of the normalized predicted mean value of k is about $10\,\%$. For the load-bearing capacities, the normalized predicted mean value has an underestimation of only $1\,\%$. Additionally, the predicted results are in good agreement with the experimental results of F^*, they reach a coefficient of determination of $R^2 = 0.88$. The results are further considered on a material-related level.
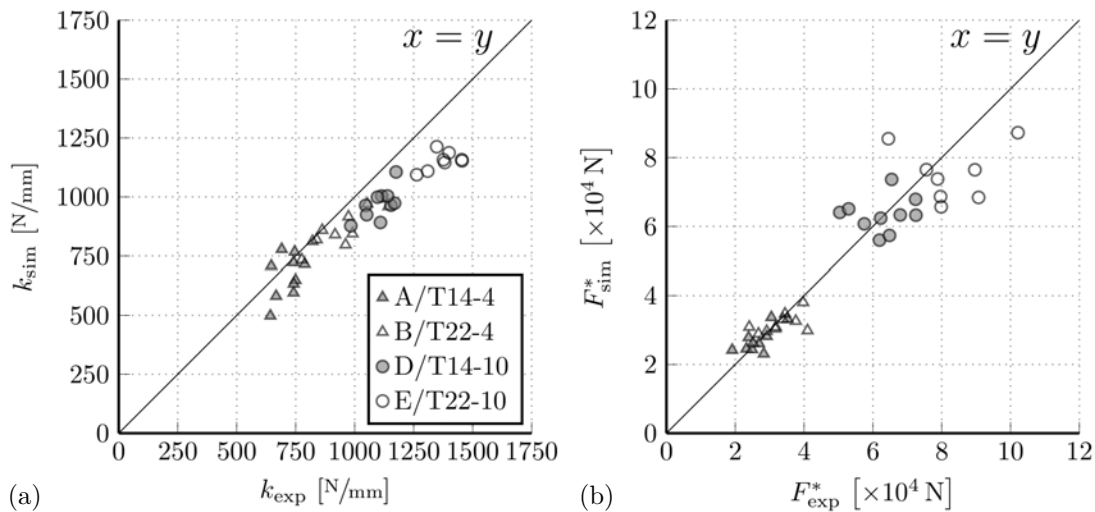

Fig. 4.2: Predicted vs. experimental results of: (a) system stiffness k and (b) load-bearing capacity F^*.

Tab. 4.6: System-related stiffness k and load-bearing capacity F^* with quantity of considered simulations Qty as well as arithmetic mean, coefficient of variation CV and difference between simulation and experiment with minimal underestimation MinU and maximum overestimation MaxO for all beam types.

Beam type	Qty[a]	k_{sim}		$k_{sim} - k_{exp}$		F^*_{sim}		$F^*_{sim} - F^*_{exp}$	
		Mean [N/mm]	CV	MinU [N/mm]	MaxO [N/mm]	Mean [N]	CV	MinU [N]	MaxO [N]
A/T14-4	10	664.8	0.13	−145.3	87.4	27 162	0.14	−5 173	5 088
B/T22-4	10	855.1	0.09	−183.6	−3.6	31 922	0.09	−11 128	6 838
D/T14-10	10	970.7	0.07	−217.8	−69.5	63 373	0.08	−9 252	13 683
E/T22-10	8	1 152.2	0.03	−302.1	−135.0	75 279	0.10	−22 294	21 001
All	38	898.0	0.21	−302.1	87.4	48 074	0.43	−22 294	21 001

[a] Successful determination of F^*_{sim} in accordance to (3.42).

Tab. 4.7: System-related stiffness k and load-bearing capacity F^* from simulations normalized by experimental results with quantity of considered simulations Qty as well as minimum, arithmetic mean, maximum values, and coefficient of variation CV as well as the coefficient of determination R^2 between predicted and experimental results for all beam types.

Beam type	Qty[a]	k_{sim} normalized by k_{exp}				R^2	F^*_{sim} normalized by F^*_{exp}				R^2
		Min	Mean	Max	CV		Min	Mean	Max	CV	
A/T14-4	10	0.77	0.93	1.13	0.13	0.15	0.82	1.03	1.27	0.12	0.54
B/T22-4	10	0.83	0.92	1.00	0.07	0.70	0.73	0.99	1.28	0.14	0.28
D/T14-10	10	0.80	0.88	0.94	0.05	0.46	0.87	1.02	1.27	0.14	0.02
E/T22-10	8	0.79	0.84	0.90	0.04	0.26	0.75	0.93	1.33	0.19	0.01
All	38	0.77	0.90	1.13	0.09	0.91	0.73	0.99	1.33	0.15	0.88

[a] Successful determination of F^*_{sim} in accordance to (3.42).

Figure 4.3 shows the material-related effective modulus of elasticity E_{GLT} and the bending strength f_{b} of the predicted vs. the experimental results. Table 4.8 gives the data for the predicted results and Table 4.9 for the predicted results normalized by the experimental results. The predicted effective moduli of elasticity inherit the previous underestimation, leading to the mean value of the normalized predicted results of 0.89. Between the predicted and experimental results of E_{GLT} the coefficient of determination reaches a value of $R^2 = 0.70$. For both strength grades, the predicted mean value of E_{GLT} from the smaller beam sizes is closer to the experimental observed mean value. The prediction of E_{GLT} has a maximum under- and overestimation of the corresponding experimental result of 23 % and 13 %, respectively, both for beams of type A/T14-4. The results of the predicted bending strength are in good agreement with the experimental results, they reach a coefficient of determination of $R^2 = 0.61$. This might be low for predicting an individual bending strength, however the mean value of all normalized predicted results reaches a value of 0.99. For f_{b}, the prediction has a maximum under- and overestimation of the corresponding experimental result of 27 % (B/T22-4) and 33 % (E/T22-10), respectively.

The greater strength class of both beam sizes has clearly a higher mean value of $E_{\mathrm{GLT,sim}}$ and $f_{\mathrm{b,sim}}$. Furthermore, for each strength class the mean value of $E_{\mathrm{GLT,sim}}$ and $f_{\mathrm{b,sim}}$ decreases for the larger beam size. The difference of $f_{\mathrm{b,sim}}$ between the two beam sizes is $9.3\,\mathrm{N/mm^2}$ for strength grade T14 and $10.5\,\mathrm{N/mm^2}$ for strength grade T22. This is a relative decrease of about 23 % and 22 % for strength grades T14 and T22, respectively. The mean values of the normalized predicted results of f_{b} are of additional interest, they show only a difference of about 1 % for beam types A/T14-4 and D/T14-10 and of about 6 % for beam types B/T22-4 and E/T22-10. This suggests that the size effect (see Section 2.1) is reasonably covered.

Now, the results are compared to other models from literature, starting with E_{GLT} and continuing with f_{b}. Kandler et al. [37] examined the GLT beams from Section 2.1 with two two-dimensional FE approaches, one that used stiffness data based on empirical dynamic stiffness measurements leading to a coefficient of determination of $R^2 = 0.88$ and the other used stiffness data based on a micro mechanical model reaching a coefficient of determination of $R^2 = 0.87$, both under consideration of all 50 GLT beams. Significant agreement was found by Fink et al. [22], who used a two-dimensional FE approach of reconstructed GLT beams with well-known knot morphology in conjunction with a regression model and consideration of uncertainties that reached a coefficient of correlation of $\rho = 0.98$ ($R^2 = 0.96$) under consideration of 24 GLT beams. Both correlations for E_{GLT} are significantly higher than the coefficient of determination of $R^2 = 0.70$ reached in the present study. Regarding the bending strength f_{b} Kandler et al. [39] examined the GLT beams from Section 2.1 with the same stiffness and strength data in a brittle two-dimensional FE approach in conjunction with a mean stress criterion and reached a coefficient of determination of $R^2 = 0.54$. In contrast, the presented quasi-brittle modeling approach shows a better agreement with a coefficient of determination of $R^2 = 0.61$, which matches the findings presented in Blank et al. [5]. However, Fink et al. [22] were able to reach a coefficient of correlation of $\rho = 0.88$ ($R^2 = 0.77$) with their approach that implemented a regression model in conjunction with considered uncertainties.
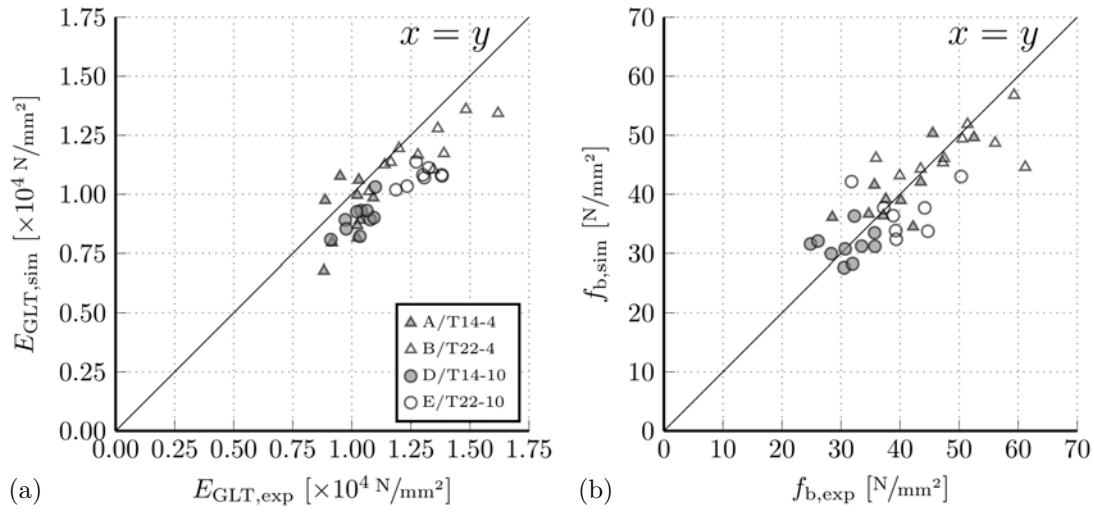
Fig. 4.3: Predicted vs. experimental results of: (a) material stiffness E_{GLT} and (b) material strength f_{b}.

Tab. 4.8: Material-related effective modulus of elasticity E_{GLT} and bending strength f_{b} with quantity of considered simulations Qty as well as arithmetic mean, coefficient of variation CV and difference between simulation and experiment with minimal underestimation MinU and maximum overestimation MaxO for all beam types.

Beam type	Qty[a]	$E_{\mathrm{GLT,sim}}$		$E_{\mathrm{GLT,sim}} - E_{\mathrm{GLT,exp}}$		$f_{\mathrm{b,sim}}$		$f_{\mathrm{b,sim}} - f_{\mathrm{b,exp}}$	
		Mean [N/mm²]	CV	MinU [N/mm²]	MaxO [N/mm²]	Mean [N/mm²]	CV	MinU [N/mm²]	MaxO [N/mm²]
A/T14-4	10	9 138	0.14	−2 081	1 262	40.5	0.14	−7.7	7.6
B/T22-4	10	11 893	0.09	−2 761	−52	47.6	0.09	−16.6	10.2
D/T14-10	10	8 986	0.07	−2 125	−689	31.2	0.08	−4.6	6.7
E/T22-10	8	10 767	0.04	−3 044	−1 357	37.1	0.10	−11.0	10.4
All	38	10 166	0.15	−3 044	1 262	39.2	0.19	−16.6	10.4

[a] Successful determination of F_{sim}^* in accordance to (3.42).

Tab. 4.9: Material-related effective modulus of elasticity E_{GLT} and bending strength f_{b} from simulations normalized by experimental results with quantity of considered simulations Qty as well as minimum, arithmetic mean, maximum values, and coefficient of variation CV as well as the coefficient of determination R^2 between predicted and experimental results for all beam types.

Beam type	Qty[a]	$E_{\mathrm{GLT,sim}}$ normalized by $E_{\mathrm{GLT,exp}}$				R^2	$f_{\mathrm{b,sim}}$ normalized by $f_{\mathrm{b,exp}}$				R^2
		Min	Mean	Max	CV		Min	Mean	Max	CV	
A/T14-4	10	0.77	0.93	1.13	0.14	0.15	0.82	1.03	1.27	0.12	0.54
B/T22-4	10	0.82	0.92	1.00	0.07	0.70	0.73	0.99	1.28	0.14	0.28
D/T14-10	10	0.79	0.87	0.94	0.05	0.46	0.87	1.02	1.27	0.14	0.02
E/T22-10	8	0.78	0.83	0.89	0.04	0.25	0.75	0.93	1.33	0.19	0.01
All	38	0.77	0.89	1.13	0.09	0.70	0.73	0.99	1.33	0.15	0.61

[a] Successful determination of F_{sim}^* in accordance to (3.42).

4.2.2 Failure mechanisms

The failure mechanisms study covers the comparison of the predicted and experimental load-displacement behavior and the fracture position of the uppermost timber board (tensile side). Furthermore, four selected simulations, one of each beam type, that show a good agreement with the corresponding experimental results are presented.

The simulated load-displacement curves are shown in Fig. 4.4. In total, 24 simulations show non-linear behavior in the load-displacement curve, whereas the experiments only showed such a behavior for nine beams. In general, the simulated non-linear load-displacement curves of the smaller beam types A/T14-4 and B/T22-4 show a more pronounced non-linear behavior than the still quite brittle failure of the larger beam types D/T14-10 and E/T22-10, this agrees with the findings of the experimental study from Section 2.1. The non-linear behavior until failure of simulations is mainly caused by the initiation and evolution of discrete cracks. An evaluation of the simulated fracture position in comparison to the documented fracture from the experimental study (Section 2.1) showed a good agreement with 30 matching simulations out of all 38 studied beams. A match is determined in regard to the topmost board when at least one section with a simulated crack corresponds to the same knot group or clear wood section with a documented crack. Table 4.10 summarizes both comparisons with the results of each beam type.
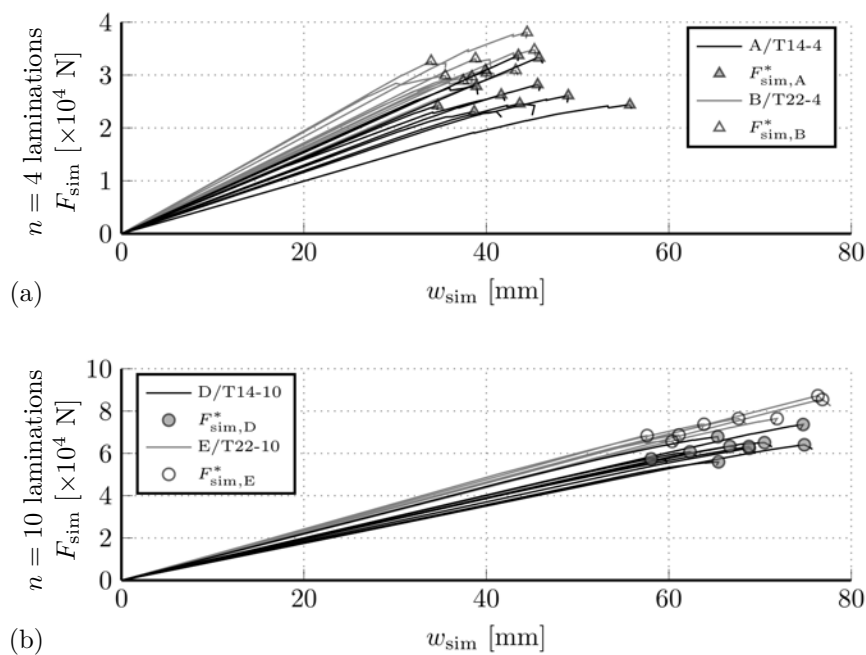

Fig. 4.4: Simulated load-displacement curve (F_{sim}-w_{sim}-curve) for beam types (a) A/T14-4 and B/T22-4 and (b) D/T14-10 and E/T22-10.

Tab. 4.10: Load-displacement (F-w) behavior of simulations and experiments and the matching fracture position of simulations and experiments for all beam types and with the quantity of considered simulations Qty.

Beam type	Qty[a]	Non-linear F-w behavior in		Matching fracture position[b]
		simulations	experiments	
A/T14-4	10	7	4	8
B/T22-4	10	7	4	9
D/T14-10	10	7	0	7
E/T22-10	8	3	1	6
All	38	24	9	30

[a] Successful determination of F_{sim}^* in accordance to (3.42).

[b] A match is considered if at least one experimental crack is located within a section that shows a simulated discrete crack in the upmost timber board.

It is important to point out that the vertical discrete cracks in the modeling approach are not able to replicate the observed fracture with horizontally propagating cracks in one timber board. Additionally, the simulated discrete cracks mainly occur at the beginning or end of a section, which is related to different stiffness properties leading to a jump in the stress field. Therefore, discrete cracks in long sections may be located in the correct knot group or clear wood section in comparison with the documented fracture, but may still significantly deviate from the exact experimental crack position.

In the following the beams A3, B5, D7, and E2 with the notation in accordance to the online supplementary material in [39] are presented more closely, where the first capital letter of each beam defines the first capital letter of the corresponding beam type. The simulations presented in the following were selected based on their good agreement between their predicted and experimental load-bearing capacities. With the determination of the load-bearing capacity, meaning after the load-bearing capacity dropped at least by 3 % and the two energy criteria (3.40) and (3.41) were satisfied, the fracture process was often still in its early stages. Therefore, the fracture patterns were examined after completion of the entire simulation.

Beam A3

Figure 4.5 shows the simulated load-displacement curve and the simulated as well as documented experimental fracture of beam A3 (A/T14-4). The slight non-linearity in the simulated load-displacement curve takes place long after the first crack initiation (see Fig. 4.5a). The experiment showed a brittle failure, which is still quite accurately described with the simulation. The predicted load-bearing capacity underestimates the experimental result by 3 %, the predicted system-related stiffness underestimates the experimental result by 13 %.

The simulated fracture gives insight into the observed failure mechanisms (see Fig. 4.5b at the point just for fracture in the load-displacement curve). The delamination allows a crack in the uppermost timber board to propagate over multiple boards, although the cracks in adjacent boards are at different horizontal positions (see Fig. 4.5c). The impact of the implementation of the delamination is further examined in Section 4.3.

Comparing the simulated fracture (Fig. 4.5b) with the documented experimental fracture (Fig. 4.5d) good agreement in the uppermost board is found. The already mentioned tendency for cracks to occur at the beginning or end of a section is observed for section marked in *beige* in the uppermost board above the load application point on the right side (see Fig. 4.5b). The described vertical crack in the *beige* knot group section corresponds to the same section of a documented experimental crack and, therefore, counts as matching crack position, although the position is different (see Figs. 4.5b and 4.5d). This illustrates the mention possible deviation of crack positions in long sections.
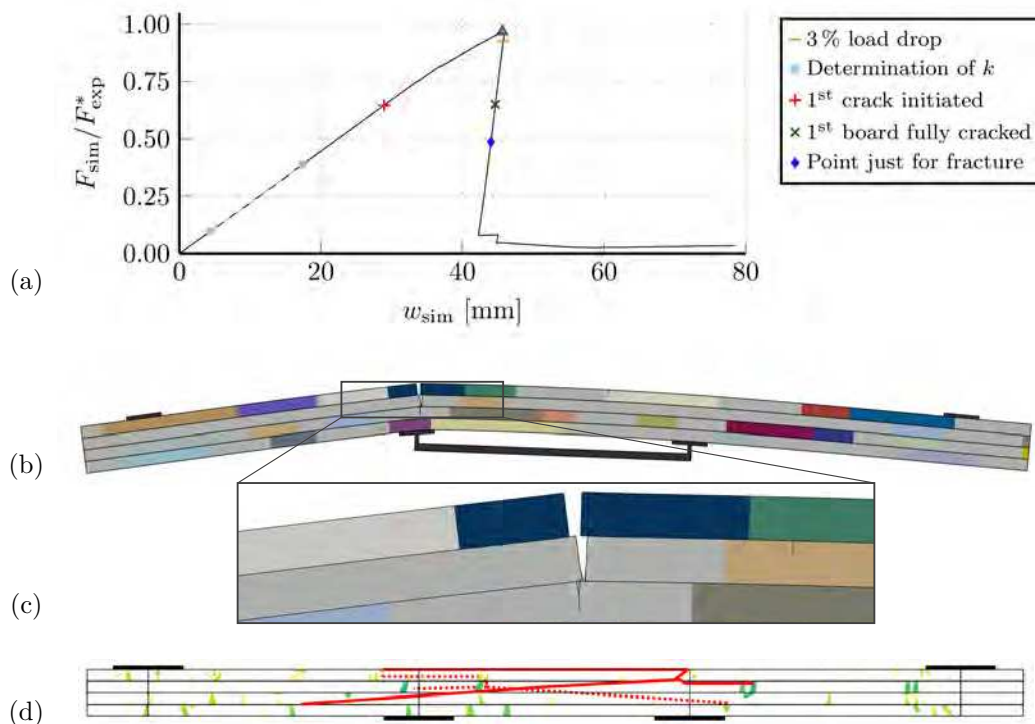

Fig. 4.5: Fracture mechanisms of beam A3 (A/T14-4): (a) load-displacement curve defining the moment of the (b) snapshot of the fracture process with (c) the enlarged detail (*light gray* and *colored* sections mark clear wood and knot groups, respectively) and (d) the documented fracture (modified from [39]; continuous and dashed *red* lines mark cracks on front and back side, respectively).

Beam B3

In the same way the findings of beam B5 (B/T22-4) are now described (see Fig. 4.6). The simulated load-displacement curve of beam B5 shows no significant influence due to the first crack initiation at the beginning (see Fig. 4.6a). Two load drops with significant reduction of the system-related stiffness follow before reaching the load-bearing capacity (see Fig. 4.6a). However, the experimental failure was brittle. The underestimation of the predicted load-bearing capacity in comparison to the experimental result is 4 % and the predicted system-related stiffness underestimates the experimental result is only 6 %.

The simulated failure mechanisms manly take place in the uppermost timber board and between the two uppermost boards (see Fig. 4.6b at the point just for fracture in the load-displacement curve). First the discrete crack in a knot group section propagates through the uppermost board until the adjacent clear wood section of the board beneath is reached. Although crack initiation in the second uppermost board takes place in close range to the discrete crack above, delamination is observed as progressing failure mechanism (see Fig. 4.6c).

The simulated fracture propagation (Fig. 4.6b) is in good agreement with the documented experimental fracture (Fig. 4.6d). It is of interest that in the uppermost board an initiated crack between the two load application points in a clear wood section corresponds quite well to a small vertical crack in the documented experimental fracture (see Figs. 4.6b and 4.6d).
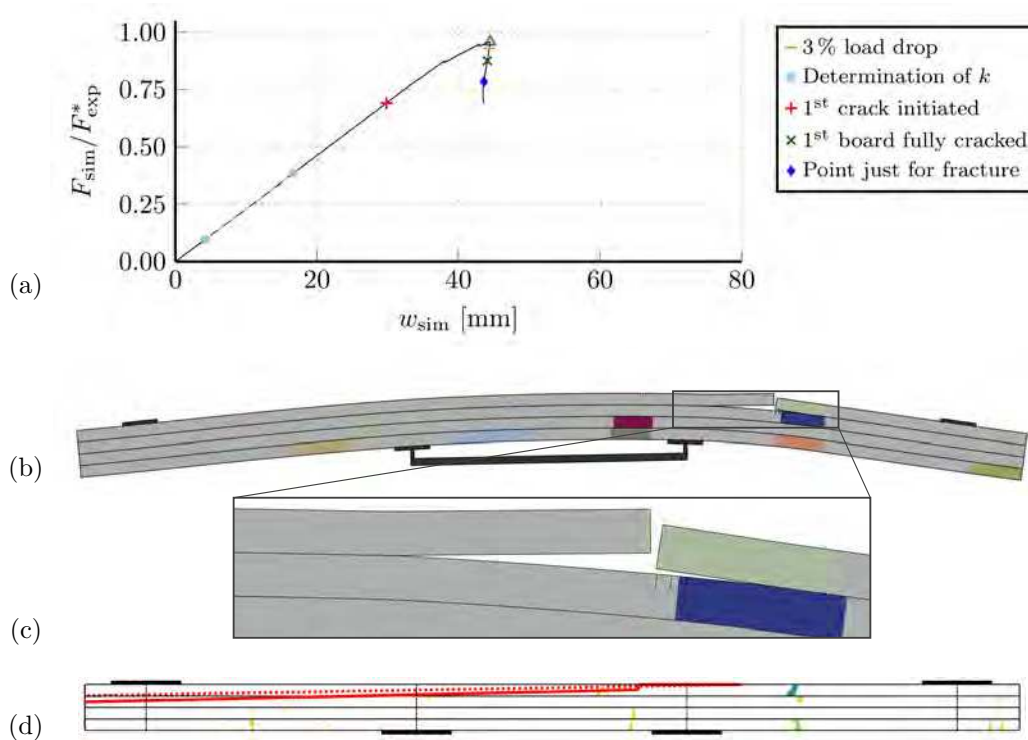

(a)

(b)

(c)

(d)

Fig. 4.6: Fracture mechanisms of beam B5 (B/T22-4): (a) load-displacement curve defining the moment of the (b) snapshot of the fracture process with (c) the enlarged detail (*light gray* and *colored* sections mark clear wood and knot groups, respectively) and (d) the documented fracture (modified from [39]; continuous and dashed *red* lines mark cracks on front and back side, respectively).

Beam D7

Now, the larger beams are described in the same way, starting with beam D7 (D/T14-10, see Fig. 4.7). Beam D7 shows a brittle failure in the simulated load-displacement curve (see Fig. 4.7a). The first crack initiation shows no significant influence on the later course of the load-displacement curve (see Fig. 4.7a). The simulated brittle failure is in good agreement with the experimental observation, which generally concurs with the findings of the experimental study for the larger beam sizes. The load-bearing capacity of the prediction matches exactly the experimental result, however the predicted system-related stiffness underestimates the experimental result by 12 %.

In Fig. 4.7b the simulated cracks are observed in the three outermost timber boards on the tensile side, at the point just for fracture in the load-displacement curve. The simulated fracture is composed by vertical discrete cracks and delamination (see Fig. 4.7c). In Fig. 4.7c two cracks are propagated over the total board height, both on one end of the knot section.

The simulated fracture (Fig. 4.7b) is in good agreement with the documented experimental fracture (Fig. 4.7d) in the uppermost board. The simulated crack in the section marked in *blue* of the uppermost board corresponds to a documented experimental crack. However, the documentation shows a second crack in this section, which emphasizes the importance of the section length for the simulated fracture (see Figs. 4.7b and 4.7d). Abaqus 2019 currently only supports the simultaneous crack initiation within a region, which is identical to the sections in this thesis (Section 3.3.1).
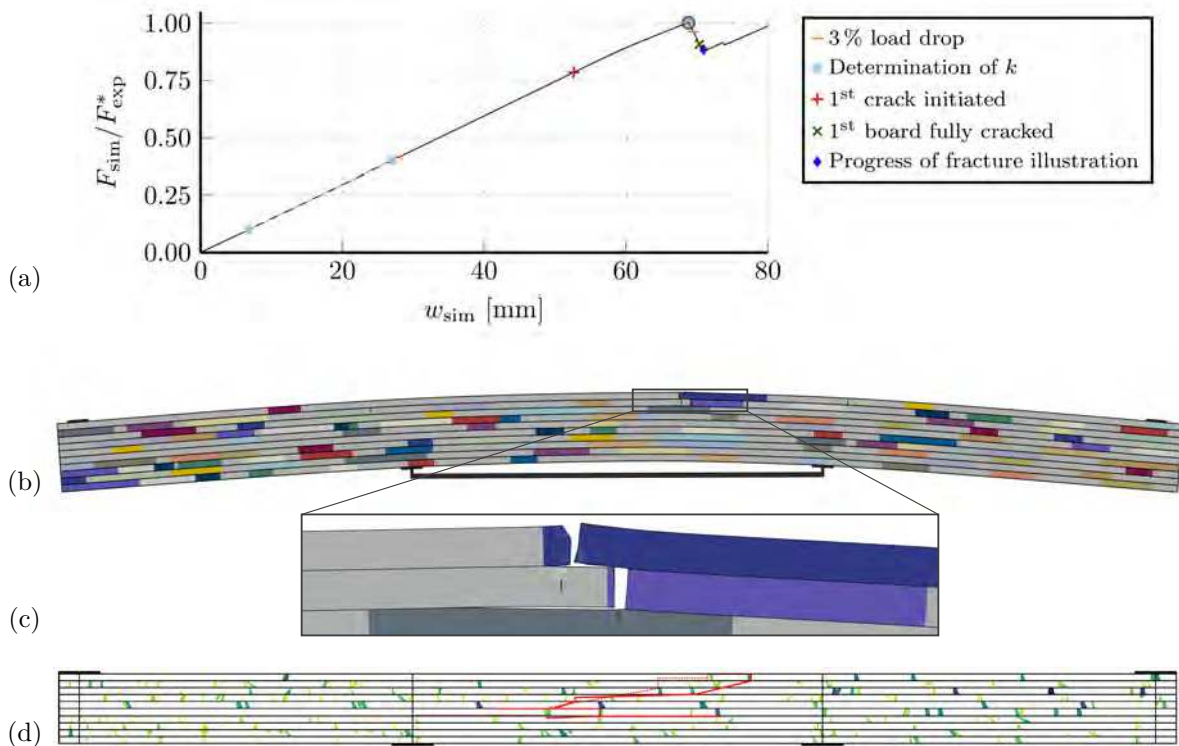

Fig. 4.7: Fracture mechanisms of beam D7 (D/T14-10): (a) load-displacement curve defining the moment of the (b) snapshot of the fracture process with (c) the enlarged detail (*light gray* and *colored* sections mark clear wood and knot groups, respectively) and (d) the documented fracture (modified from [39]; continuous and dashed *red* lines mark cracks on front and back side, respectively).

Beam E2

The findings of beam E2 (E/T22-10) are described in the following (see Fig. 4.8). Again, the simulated load-displacement curve shows brittle failure without a significant influence of the first crack initiation (see Fig. 4.8a), which is in good agreement with the experimental observation and in general with the larger beam size. The predicted load-bearing capacity overestimates the experimental result by only 1 %, however the predicted system-related stiffness underestimates the experimental result by 21 %.

In Fig. 4.8b a main fracture with quite vertical propagation in the uppermost timber boards is observed, at the point just for fracture in the load-displacement curve. The main fracture propagates through three knot group sections, which are underneath each other and reaches down to the fourth uppermost board (see Fig. 4.8c). In addition, the uppermost board shows two cracks in knot group sections on the right side of the main crack: one in the section marked in *dark gray* (see Fig. 4.8c) and one in the section marked in *purple*, even further to the right side (see Fig. 4.8b). In both cases the cracks were reinforced by a clear wood sections in the adjacent board.

A comparison between the simulated fracture (Fig. 4.8b) and the documented experimental fracture (Fig. 4.8d) shows that the position of the main crack in the uppermost timber board does not match. However, the positions with the two other mentioned cracks are in good agreement of the documented fracture (see Figs. 4.8b and 4.8d).
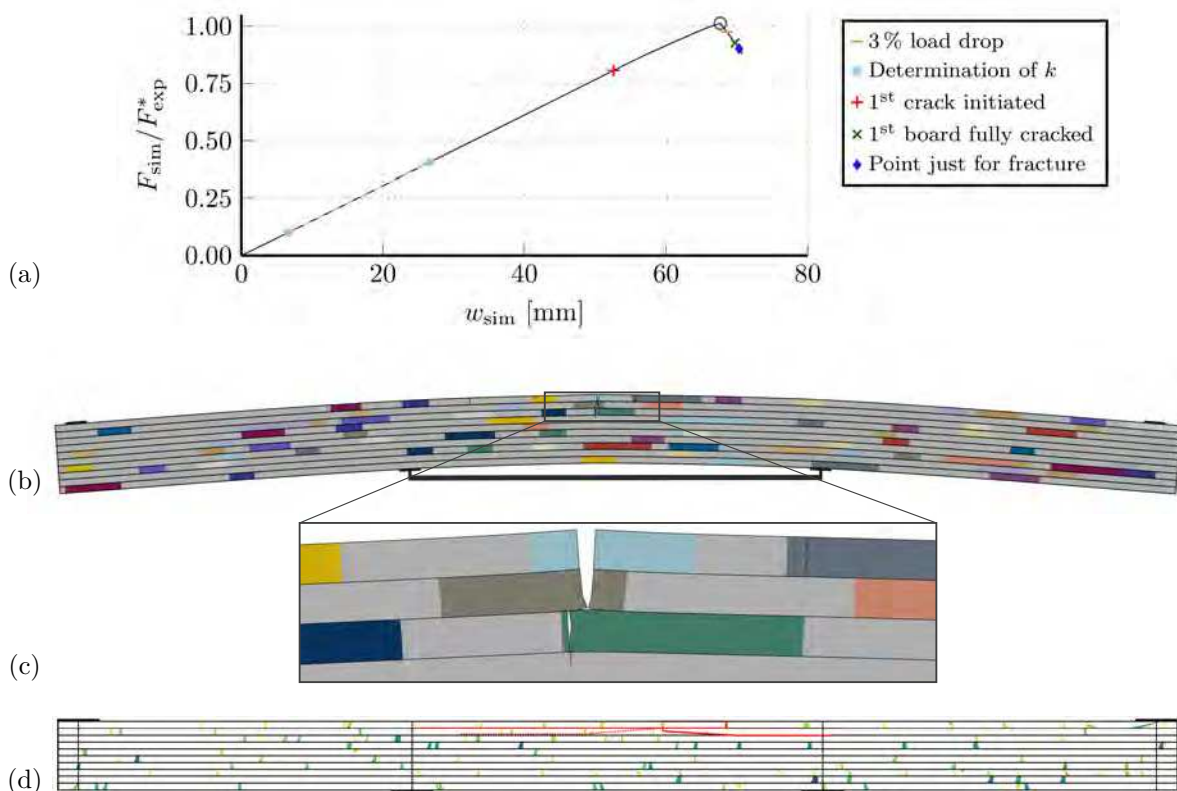

Fig. 4.8: Fracture mechanisms of beam E2 (E/T22-10): (a) load-displacement curve defining the moment of the (b) snapshot of the fracture process with (c) the enlarged detail (*light gray* and *colored* sections mark clear wood and knot groups, respectively) and (d) the documented fracture (modified from [39]; continuous and dashed *red* lines mark cracks on front and back side, respectively).

4.3 Sensitivity of material parameters

This study aims to determine the influence of parameters on the load-bearing capacity. The selected parameters cover the initiation and evolution of delamination and discrete cracks. It is important to evaluate the implementation of the delamination and to know the sensitivity of the selected parameters in order to further improve the modeling approach. In regard to delamination from Section 3.3.2 the following parameters are examined:

- the implementation of delamination,
- delamination initiation due to out-of-plane strength,
- delamination initiation due to in-plane strength, and
- delamination fracture energy, which governs the evolution.

In regard to discrete cracks from Section 3.3.1 the following parameters are examined:

- strength profiles for the crack initiation in timber boards, and
- crack fracture energy, which governs the evolution.

In this study those six parameters are covered in a total of 25 sets. As basis for the parameter values and the enriched volume serves the validated set from Section 4.2. A brief explanation of the individual parameters is given in Section 4.1. The parameters are not expected to be significantly correlated and due to the high computational cost each parameter is considered for itself. This means that only the selected parameter changes while the other parameters remain the same. Table 4.11 gives a summary of the selected parameters, where the validated set is included in multiple sets in order to compare the results of a parameter within one group. The obtained result of the simulations is the load-bearing capacity, which is determined according to criterion (3.42). Additionally, the experimental results from Section 2.1 are used. The parameters are presented in the order shown above.

Implementation of delamination

First, the influence of a suppressed delamination rather than the implemented delamination from Chapter 3 is examined. The modeling of the suppressed delamination is achieved by simply tying together all adjacent timber boards. The influence is determined for two fracture energies by a comparison between sets with suppressed and allowed delamination, the other parameters are identical. The lower fracture energy is $G_{f,cra} = 10.0 \, \mathrm{N \, mm/mm^2}$ for sets D1-no and D1-yes, with suppressed and allowed delamination, respectively. Analog, sets D2-no and D2-yes have a higher fracture energy is $G_{f,cra} = 35.0 \, \mathrm{N \, mm/mm^2}$, which corresponds to $G_{f,cra}$ of the validated model.

The results of the two comparisons are shown in Fig. 4.9 for all four beam types, where the horizontal axis distinguishes between suppressed delamination or delamination and the vertical axis gives the predicted load-bearing capacity that is normalized by the corresponding experimental result. Table 4.12 gives the statistical data of the normalized load-bearing capacity. Both sets that allow delamination are able to determine a valid load-bearing capacity for all models contrary to the two sets that suppress delamination. The reason of simulations failing to determine the load-bearing capacity for the latter is a load decline of less than 3 %, which leads to the omission of the results. All omitted results belong to simulations of beam type D/T14-10. The influence on the arithmetic mean and coefficient of variation CV is minor with about 2 % and about 3 ‰, respectively. However, influence is observed for individual load-bearing capacities: Table 4.13 compares the load-bearing capacity of sets with delamination normalized by the results of the sets suppressing delamination (ratios of D1-yes to D1-no with $G_{f,cra} = 10.0 \, \mathrm{N \, mm/mm^2}$ and D2-yes to D2-no with $G_{f,cra} = 35.0 \, \mathrm{N \, mm/mm^2}$). The greatest difference is observed for the set D2-yes normalized by D2-no (higher fracture energy), where delamination reduces the load-bearing capacity by 17.4 %. The number of influenced simulations is higher for the simulations with higher fracture energy that governs the discrete crack evolution.

Tab. 4.11: Parameter sensitivity sets with discrete crack parameters: tensile strength in fiber direction $f_{t,0}$, fracture energy $G_{f,cra}$ and delamination parameters: out-of-plane strength f_n^*, in-plane strengths $f_p^* = f_q^*$, fracture energy $G_{f,del}$; *gray* sets and parameter values determine F_{sim}^* in accordance to (3.42) for less than 35 simulations.

| Material parameters for | Set | discrete cracks[a] | | delamination[a] | | |
		$f_{t,0}$[b] [N/mm²]	$G_{f,cra}$ [N mm/mm²]	f_n^* [N/mm²]	$f_p^* = f_q^*$ [N/mm²]	$G_{f,del}$ [N mm/mm²]
Parameters of validated model	V1[c]	SP3	35.0	10.0	100.0	1.0
Sets for delamination parameters						
Implemented delamination	D1-no	SP3	10.0	–	–	–
	D1-yes[d]			10.0	100.0	1.0
	D2-no		35.0	–	–	–
	D2-yes[e]			10.0	100.0	1.0
Out-of-plane strength	D1-f_n^*	SP3	35.0	0.3	100.0	1.0
	D2-f_n^*			1.15		
	D3-f_n^*			2.0		
	D4-f_n^*			4.0		
	D5-f_n^*			8.0		
	D6-f_n^*			12.0		
	D7-f_n^*			16.0		
In-plane strength	D1-$f_{p,q}^*$	SP3	35.0	100.0	4.0	1.0
	D2-$f_{p,q}^*$				7.0	
	D3-$f_{p,q}^*$ [e]				10.0	
	D4-$f_{p,q}^*$				13.0	
	D5-$f_{p,q}^*$				16.0	
Delamination fracture energy	D1-$G_{f,del}$	SP3	35.0	100.0	10.0	0.4
	D2-$G_{f,del}$[e]					1.0
	D3-$G_{f,del}$					1.6
	D4-$G_{f,del}$					4.0
Sets for discrete crack parameters						
Strength profiles	B1-SP3[e]	SP3	35.0	100.0	10.0	1.0
	B2-SP4	SP4				
Crack fracture energy	B1-$G_{f,cra}$	SP3	10.0	100.0	10.0	1.0
	B2-$G_{f,cra}$		15.0			
	B3-$G_{f,cra}$		20.0			
	B4-$G_{f,cra}$		25.0			
	B5-$G_{f,cra}$		30.0			
	B6-$G_{f,cra}$[e]		35.0			
	B7-$G_{f,cra}$		50.0			
	B8-$G_{f,cra}$		65.0			
	B9-$G_{f,cra}$		80.0			

[a] Applied viscosity parameter $\mu = 1 \times 10^{-6}$ for discrete cracks and delamination.
[b] Strength profile from Section 2.2 limited by: $f_{t,0,min} = 10 \, N/mm^2$ and $f_{t,0,max} = 55 \, N/mm^2$.
[c] Validated parameter values from Section 4.2.
[d] Parameter values identical to set B1-$G_{f,cra}$.
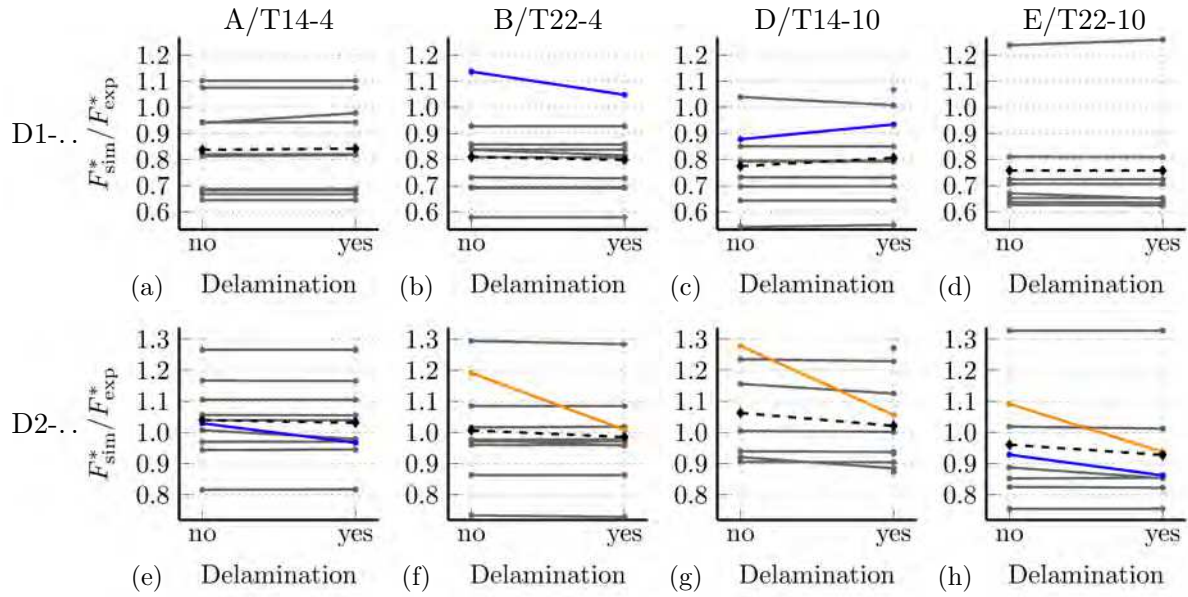[e] Parameter values identical to set V1.

Fig. 4.9: Delamination impact on the load-bearing capacity normalized by the experimental results for set (a–d) D1 with lower and (e–h) D2 with higher discrete crack fracture energy of all four beam types; *continuous* lines link individual results and *dashed* lines link arithmetic mean values of each set; *blue* and *orange* color mark deviations greater than 5 % and 10 %, respectively.

Tab. 4.12: Delamination sets for lower and higher fracture energy of discrete cracks $G_{\mathrm{f,cra}}$: each with the quantity of considered simulations Qty as well as the minimum and maximum values, and coefficient of variation CV of the load-bearing capacity normalized by experimental results.

	$G_{\mathrm{f,cra}} = 10.0\,\mathrm{N\,mm/mm^2}$					$G_{\mathrm{f,cra}} = 35.0\,\mathrm{N\,mm/mm^2}$				
Set	Qty[a]	Min	Mean	Max	CV	Set	Qty[a]	Min	Mean	Max	CV
D1-no	37	0.542	0.798	1.238	0.205	D2-no	35	0.733	1.017	1.327	0.150
D1-yes	38	0.550	0.804	1.259	0.206	D2-yes	38	0.729	0.995	1.328	0.147
Δ	1	0.008	0.006	0.021	0.001	Δ	3	0.004	0.022	0.001	0.003

[a] Successful determination of F_{sim}^* in accordance to (3.42).

Tab. 4.13: Normalized delamination sets with the discrete crack fracture energy $G_{\mathrm{f,cra}}$ and quantity of considered simulations Qty as well as minimum and maximum values of the load-bearing capacity with delamination normalized by results without delamination and the quantity of simulations with more than 5 % and 10 % deviation.

Normalized set	$G_{\mathrm{f,cra}}$ [N mm/mm²]	Qty[a]	Min	Max	deviates more than	
					5 %	10 %
D1-yes normalized by D1-no	10.0	37	0.922	1.065	2	0
D2-yes normalized by D2-no	35.0	35	0.826	1.002	5	3

[a] Successful determination of F_{sim}^* in accordance to (3.42).

All three simulations that deviate more than $10\,\%$ show a similarity in their crack pattern when reaching the load-bearing capacity. The pattern consists of vertical cracks that occur simultaneously in adjacent timber boards with a shifted position in horizontal direction. The influenced simulations from Figs. 4.9a to 4.9d with the lower fracture energy and from Figs. 4.9e to 4.9h with the higher fracture energy correspond to different beams.

The observations of the compared load-bearing capacities from simulations with and without allowed delamination lead to two suggestions. First, a higher fracture energy leads to an increase in progressing failure, where cracks reach over more than one timber board. Second, that an expansion with merging cracks over more than one board significantly impacts the load-bearing capacity, which can be accurately covered with the presented implementation of delamination.

Delamination initiation due to out-of-plane strength

The results of the out-of-plane strength values of the delamination surfaces f_n^* as delamination initiation parameter are illustrated in Fig. 4.10 and the corresponding data is given in Table 4.14. A major impact on whether the predicted load-bearing capacity is determined or not is observed, however the influence on the predicted load-bearing capacity is of minor significance. The covered range of parameter values in this study starts with the characteristic value of the tensile strength perpendicular to the fiber direction $f_{t,90,k} = 0.3\,\mathrm{N/mm^2}$, according to DIN EN 338:2016-07 [15]. The further delamination strengths are estimates in order to gain expressive results. On basis of the results it is not expected to see significant influence for f_n^* greater than $16.0\,\mathrm{N/mm^2}$. The validated set V1 uses only the following in-plane strength as initiation of delamination.
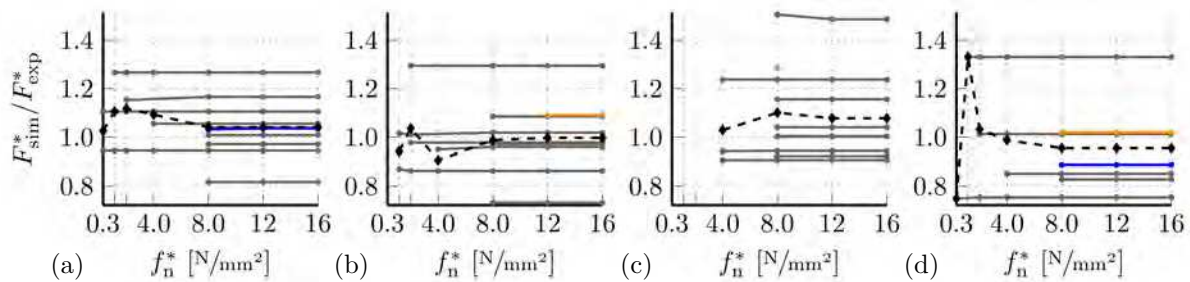

Fig. 4.10: Impact of the out-of-plane strength f_n^* as delamination initiation parameter on the load-bearing capacity normalized by the experimental results for all four beam types: (a) A/T14-4, (b) B/T22-4, (c) D/T14-10, and (d) E/T22-10; *continuous* lines link individual results and *dashed* lines link arithmetic mean values of each set; *blue* and *orange* color mark the same beams as in Fig. 4.9.

Tab. 4.14: Sets with the out-of-plane strength f_n^* as sensitivity parameter and the quantity of considered simulations Qty as well as the minimum, arithmetic mean, maximum values, and coefficient of variation CV of the load-bearing capacity normalized by experimental results.

Set	f_n^* [N/mm²]	Qty[a]	Min	Mean	Max	CV
D1-f_n^*	0.3	3	0.749	0.933	1.105	0.191
D2-f_n^*	1.2	6	0.870	1.089	1.330	0.166
D3-f_n^*	2.0	11	0.754	1.065	1.330	0.173
D4-f_n^*	4.0	13	0.754	1.017	1.330	0.172
D5-f_n^*	8.0	35	0.732	1.028	1.505	0.165
D6-f_n^*	12.0	36	0.732	1.021	1.486	0.157
D7-f_n^*	16.0	36	0.732	1.021	1.486	0.157

[a] Successful determination of F_{sim}^* in accordance to (3.42).

Delamination initiation due to in-plane strength

Next, the influence on the results of the in-plane strength values of the delamination surfaces f_p^* and f_q^* as delamination initiation parameter is studied. Figure 4.11 illustrates the results and Table 4.15 gives the corresponding data. All simulations determine the load-bearing capacity for all f_p^* and f_q^* greater than $7.0\,\text{N/mm}^2$, which corresponds to sets D2-$f_{p,q}$ to D5-$f_{p,q}$. Single beams show a tendency to reach higher load-bearing capacities with higher in-plane strength values (see Fig. 4.11), however the consideration of sets as a whole shows no significant influence (see Table 4.15). It is comprehensible that influence is observed with increasing in-plane strength especially for simulations that showed an significant impact due to the allowed delamination (see Figs. 4.11b and 4.11d). The covered range of studied parameter values starts with the characteristic shear strength $f_{v,k} = 4.0\,\text{N/mm}^2$ for strength classes greater than C24, according to DIN EN 338:2016-07 [15]. A second reference value is the mean shear strength of clear wood $f_{v,mean} = 10.0\,\text{N/mm}^2$, according to DIN 68364:2003-05 [13]. The shear strength is used in both strength directions f_p^* and f_q^*. In between those two values one set is interpolated. Further estimates of the delamination strengths are made in order to gain expressive results. Significant impact on the results for $f_p^* = f_q^*$ greater than $16.0\,\text{N/mm}^2$ is not expected. The validated in-plane strength for the initiation of delamination of set V1 is $f_p^* = f_q^* = 10.0\,\text{N/mm}^2$, which matches with the mentioned mean shear strength of clear wood $f_{v,mean} = 10.0\,\text{N/mm}^2$.
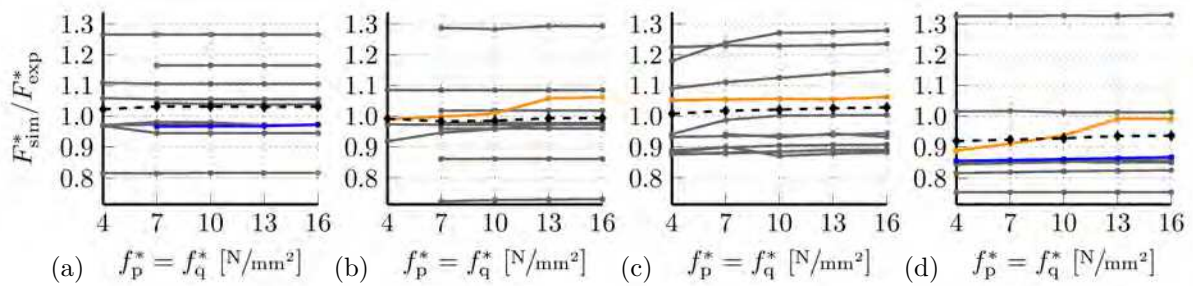

Fig. 4.11: Impact of the in-plane strengths $f_p^* = f_q^*$ as delamination initiation parameter on the load-bearing capacity normalized by the experimental results for all four beam types: (a) A/T14-4, (b) B/T22-4, (c) D/T14-10, and (d) E/T22-10; *continuous* lines link individual results and *dashed* lines link arithmetic mean values of each set; *blue* and *orange* color mark the same beams as in Fig. 4.9.

Tab. 4.15: Sets with the in-plane strength $f_p^* = f_q^*$ as sensitivity parameter and the quantity of considered simulations Qty as well as the minimum, arithmetic mean, maximum values, and coefficient of variation CV of the load-bearing capacity normalized by experimental results.

Set	$f_p^* = f_q^*$ [N/mm²]	Qty[a]	Min	Mean	Max	CV
D1-$f_{p,q}^*$	4.0	28	0.754	0.984	1.326	0.145
D2-$f_{p,q}^*$	7.0	38	0.724	0.992	1.327	0.147
D3-$f_{p,q}^*$	10.0	38	0.729	0.995	1.328	0.147
D4-$f_{p,q}^*$	13.0	38	0.730	0.999	1.327	0.147
D5-$f_{p,q}^*$	16.0	38	0.732	1.001	1.330	0.148

[a] Successful determination of F_{sim}^* in accordance to (3.42).

Delamination fracture energy

As last parameter of the delamination, the results of the fracture energy $G_{f,del}$ as evolution parameter are illustrated in Fig. 4.12 and the corresponding data is given in Table 4.16. The load-

bearing capacity shows hardly any influence for $G_{\mathrm{f,del}}$ greater than $1.0\,\mathrm{N\,mm/mm^2}$. Therefore, for values of $G_{\mathrm{f,del}}$ that are greater than $4.0\,\mathrm{N\,mm/mm^2}$ no significant influence is expected. On the lower end of the range, comparing D1-$G_{\mathrm{f,del}}$ ($G_{\mathrm{f,del}} = 0.4\,\mathrm{N\,mm/mm^2}$) to D2-$G_{\mathrm{f,del}}$ ($G_{\mathrm{f,del}} = 1.0\,\mathrm{N\,mm/mm^2}$), a small influence is observed. However, in comparison to impacts of previously discussed delamination parameters on single beams the significance is judged of minor importance, even for values of $G_{\mathrm{f,del}}$ that are smaller than $0.4\,\mathrm{N\,mm/mm^2}$. The validated set V1 uses a fracture energy for delamination of $G_{\mathrm{f,del}} = 1.0\,\mathrm{N\,mm/mm^2}$.
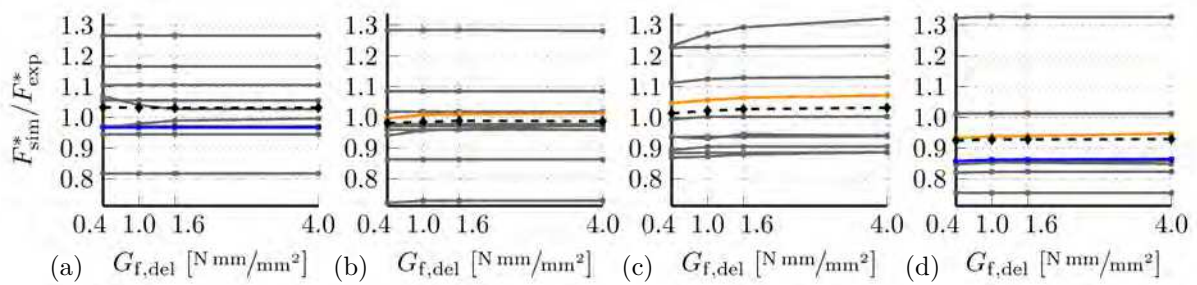

Fig. 4.12: Impact of the fracture energy $G_{\mathrm{f,del}}$ as delamination evolution parameter on the load-bearing capacity normalized by the experimental results for all four beam types: (a) A/T14-4, (b) B/T22-4, (c) D/T14-10, and (d) E/T22-10; *continuous* lines link individual results and *dashed* lines link arithmetic mean values of each set; *blue* and *orange* color mark the same beams as in Fig. 4.9.

Tab. 4.16: Sets with the delamination fracture energy $G_{\mathrm{f,del}}$ as sensitivity parameter and the quantity of considered simulations Qty as well as the minimum, arithmetic mean, maximum values, and coefficient of variation CV of the load-bearing capacity normalized by experimental results.

Set	$G_{\mathrm{f,del}}$ $[\mathrm{N\,mm/mm^2}]$	Qty[a]	Min	Mean	Max	CV
D1-$G_{\mathrm{f,del}}$	0.4	38	0.722	0.991	1.324	0.147
D2-$G_{\mathrm{f,del}}$	1.0	38	0.729	0.995	1.328	0.147
D3-$G_{\mathrm{f,del}}$	1.6	37	0.729	0.997	1.327	0.150
D4-$G_{\mathrm{f,del}}$	5.0	38	0.729	0.998	1.327	0.149

[a] Successful determination of F_{sim}^* in accordance to (3.42).

Strength profiles

Now, the results of the first material parameter are presented. Figure 4.13 illustrates the results of strength profiles SP3 and SP4 to determine crack initiation from Section 2.2 and Table 4.17 gives the corresponding data. One simulation of beam type D/T14-10 with strength profile SP4 fails to determine the load-bearing capacity in accordance to criterion (3.42) by exceeding the energy criterion (3.40). The difference of the mean and coefficient of variation is minor with about $2\,\%$ and about $1\,‰$, respectively. Table 4.18 gives the load-bearing capacity of set B2-SP4 normalized by set B1-SP3 for each beam type in order to compare the differences of both sets. The greatest difference is observed for beam type A/T14-4, where the use of strength profile SP4 leads to a load-bearing capacity that is $11.4\,\%$ higher than the result of strength profile SP3. Strength profile SP3 is used in the validated set V1. In general, cracks appear in knot group sections with low strength values that are not reinforced by adjacent clear wood sections.

The histograms of the timber board strength values for both strength grades T14 and T22 as well as both used strength profiles SP3 and SP4 are displayed in Fig. 2.6. There, the median value from strength profile SP3 to SP4 shows for strength grade T14 an increase of $3.14\,\mathrm{N/mm^2}$

(15.4 %) and for strength grade T22 an increase of $1.46 \, \text{N/mm}^2$ (5.5 %). The use of strength profile SP4 rather than SP3 leads also to a tendency of an increasing load-bearing capacities, where the increase is higher for strength grade T14 than for strength grade T22 (see Table 4.18).

The observed correlation between the timber board strength and the load-bearing capacity suggests that the used strength profile is of great importance and needs to adequately replicate the real timber boards. Furthermore, due to the observation of more likely initiated cracks in knot group sections with low strength values the allocation of such knot groups is important to adequately replicate the real crack patterns.
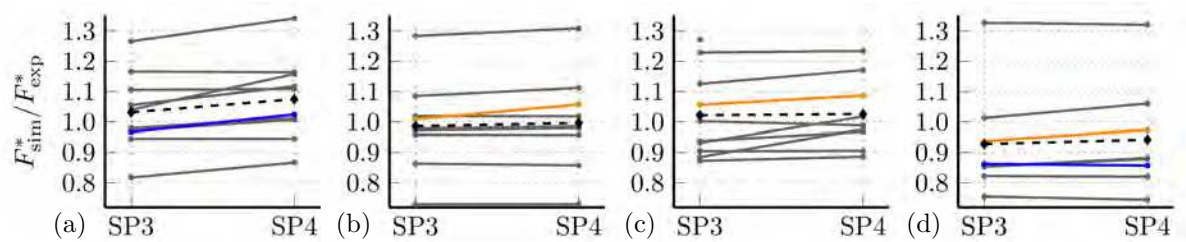

Fig. 4.13: Impact of strength profiles SP3 and SP4 as discrete crack initiation parameter on the load-bearing capacity normalized by the experimental results for all four beam types: (a) A/T14-4, (b) B/T22-4, (c) D/T14-10, and (d) E/T22-10; *continuous* lines link individual results and *dashed* lines link arithmetic mean values of each set; *blue* and *orange* color mark the same beams as in Fig. 4.9.

Tab. 4.17: Sets of strength profiles SP3 and SP4 and the quantity of considered simulations Qty as well as the minimum, arithmetic mean, maximum values, and coefficient of variation CV of the load-bearing capacity normalized by experimental results.

Set	Qty[a]	Min	Mean	Max	CV
B1-SP3	38	0.729	0.995	1.328	0.145
B2-SP4	37	0.729	1.013	1.342	0.144
Δ	1[b]	0.000	0.018	0.014	0.001

[a] Successful determination of F_{sim}^* in accordance to (3.42).
[b] Simulation exceeding energy criterion (3.40).

Tab. 4.18: All beam types with quantity of considered simulations Qty as well as minimum and maximum values of the load-bearing capacity with strength profile SP4 normalized by results wit strength profile SP3 and the quantity of simulations with more than 5 % and 10 % deviation.

Beam type	Qty[a]	Min	Max	deviates more than	
				5 %	10 %
A/T14-4	10	0.998	1.114	5	1
B/T22-4	10	0.994	1.048	0	0
D/T14-10	9	0.986	1.289	3	2
E/T22-10	8	0.986	1.047	0	0
All	37	0.986	1.289	8	3

[a] Successful determination of F_{sim}^* in accordance to (3.42).

Crack fracture energy

Finally, the results of the fracture energy $G_{f,cra}$ as crack evolution parameter are illustrated in Fig. 4.14 and the corresponding data is given in Table 4.19. The mean values of each beam type show a concave increase of the load-bearing capacity with increasing fracture energy. The range of the parameter starts with the fracture energy used in [5] and the steps expand for greater values in order to cover a wide range. The validated fracture energy for discrete cracks of set V1 is $G_{f,cra} = 35.0 \, \mathrm{N\,mm/mm^2}$. In general, the big influence of the fracture energy on the load-bearing capacities brings up the question if the assumption of a constant fracture energy is reasonable.
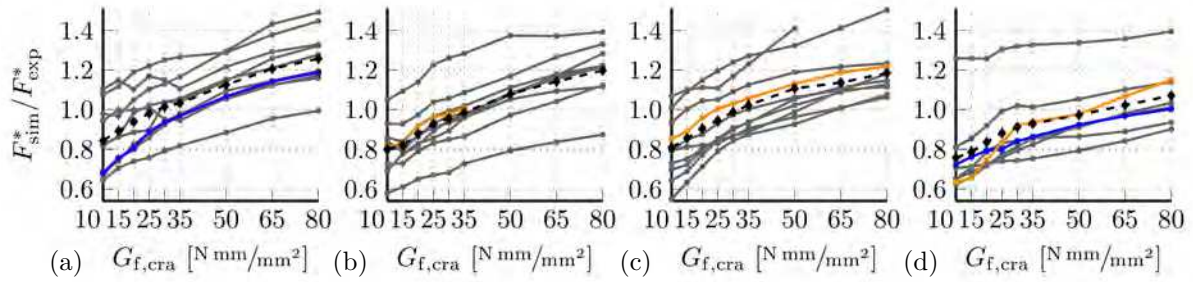

Fig. 4.14: Impact of the fracture energy $G_{f,cra}$ as discrete crack evolution parameter on the load-bearing capacity normalized by the experimental results for all four beam types: (a) A/T14-4, (b) B/T22-4, (c) D/T14-10, and (d) E/T22-10; *continuous* lines link individual results and *dashed* lines link arithmetic mean values of each set; *blue* and *orange* color mark the same beams as in Fig. 4.9.

Tab. 4.19: Sets with the discrete crack fracture energy $G_{f,cra}$ as sensitivity parameter and the quantity of considered simulations Qty as well as the minimum, arithmetic mean, maximum values, and coefficient of variation CV of the load-bearing capacity normalized by experimental results.

Set	$G_{f,cra}$ [$\mathrm{N\,mm/mm^2}$]	Qty[a]	Min	Mean	Max	CV
B1-$G_{f,cra}$	10.0	38	0.550	0.804	1.259	0.203
B2-$G_{f,cra}$	15.0	38	0.610	0.841	1.259	0.188
B3-$G_{f,cra}$	20.0	38	0.650	0.891	1.257	0.167
B4-$G_{f,cra}$	25.0	38	0.671	0.936	1.305	0.160
B5-$G_{f,cra}$	30.0	38	0.683	0.970	1.320	0.152
B6-$G_{f,cra}$	35.0	38	0.729	0.995	1.328	0.145
B7-$G_{f,cra}$	50.0	37	0.794	1.076	1.411	0.142
B8-$G_{f,cra}$	65.0	36	0.835	1.132	1.433	0.133
B9-$G_{f,cra}$	80.0	36	0.872	1.183	1.504	0.130

[a] Successful determination of F_{sim}^* in accordance to (3.42).

Chapter 5

Summary, conclusions, and outlook

Starting with proposed models from literature, the motivation was to develop a computational modeling approach to determine the bending strength as well as failure mechanisms of GLT beams taking into account knot groups and quasi-brittle material failure. In order to validate the simulations, the experimental results of GLT beams with well-known knot morphology subjected to four-point bending until failure, presented in [37, 39], were used. Additionally, the detailed knot morphology was used to derive section-wise constant effective stiffness and strength profiles of each used timber board [41], based on three-dimensional reconstructed knot geometry. In this thesis, those profiles are used to virtually reconstruct the GLT beams and to assign effective material properties without following a predefined grid pattern. Failure mechanisms are described by vertical discrete cracks, which were realized with XFEM in conjunction with a modified traction-separation law, and by delamination between timber boards to cover horizontal cracking in an simplified way, which was realized with cohesive surfaces in conjunction with a modified traction-separation law. This enabled the coverage of expanding cracks over multiple timber boards and allowed vertical cracks with a horizontal distance in adjacent boards to merge. The discrete cracks and delamination were initiated and propagated by maximum stress criteria and their evolution was governed by constant fracture energies, which were different for both cases. The approach was realized within the framework of non-linear FEM with a linear elastic, orthotropic material model for timber boards. Finally, the load-bearing capacity was identified by a 3% load drop in the load-displacement curve, which enabled progressive failure. Additionally, two energy criteria needed to be complied with. The bending strength was then determined based on the load-bearing capacity with simplifying assumptions of stress and strain fields.

The presented modeling approach is well equipped to examine the load-bearing capacity as well as the bending strength with depicted failure mechanisms. It is important to point out that many presented assumptions were necessary to derive the used effective material properties that introduced uncertainties, e.i. the quite low reliability of the strength profiles. Lukacevic et al. [48] studied the prediction of the tensile strength with different IPs, where the KAR value resulted in a coefficient of determination of $R^2 = 0.62$ for manually recorded knots. The determination of strength profile SP3 used an IP also just based on the KAR value. The proposed computational modeling approach was still able to achieve good agreement in terms of bending strength and failure mechanisms, regardless to the restrictions of the assumptions and their uncertainties in the input data.

In terms of the mesh size dependency of the model, the following conclusions can be drawn:

- A mesh size of three finite elements over the timber board height in conjunction with a shape function of linear order is in general sufficient.

- The allocation of the section-wise effective constant material properties may have a significant influence on the results and, therefore, needs to supply appropriate position as well as values of weak points. Additionally, it is important to carefully consider the section length in order to define the structure of interacting adjacent sections.

Regarding the verification of the model, the following conclusions can be drawn:

- The predicted effective moduli of elasticity show the same characteristics as the experimental results. However, the simulations underestimate the experimental results of the effective moduli of elasticity by about 11 %.

- The predicted bending strengths show the same characteristics as the experimental results, i.e. the influence of the size effect, which leads to a decrease of the bending strength of the beam types with larger beam size. The modeling approach is able to accurately predict the bending strength, however, the largest underestimation of the mean value compared to the experimental results is 7 % for beam type E/T22-10.

- The simulated load-displacement curves show the same characteristics as the experimental results, i.e. a more brittle failure for the larger beam types. Further, the simulated non-linear behavior of the load-displacement curve shares the characteristics of the experimental observations. However, the simulations lead to a more often non-linear curve, which most likely is related to the relatively high fracture energy of $G_{\mathrm{f,cra}} = 35\,\mathrm{N/mm}^2$ that is used for the discrete cracks in the approach.

- The simulated failure mechanisms, described with discrete cracks and delamination, show good agreement with the documented results from experiments, i.e. 30 of all 38 simulated beams have at least one section with a simulated crack in the topmost timber board that is related to the same corresponding knot group or clear wood section with a documented crack. The importance of the allocation and length of the section-wise effective constant material properties has to be emphasized. Vertical discrete cracks mainly occur at the start or end of a section due to the load transfer with changing stiffness properties. Additionally, they are responsible for the determination of the predicted load-bearing capacity and need to be rendered accurately.

With regard to the sensitivity of the material properties used in the model, the following conclusions can be drawn:

- The delamination influences the load-bearing capacity when failure of the GLT beam is related to crack growth over multiple timber boards. However, in the present study only a few beams show an influence on the load-bearing capacity by comparing beams with and without delamination and otherwise the same material parameters, thus, the influence is limited only to single beams. Additionally, an increase of the fracture energy of vertical discrete cracks leads to an increase of involved boards in the failure mechanisms, which can be expected due to an increase of the system's ductility.

- The initiation strength and fracture energy of delamination has a major impact on convergence behavior of the approach. However, the impact on the predicted load-bearing capacity is of less relevance.

- The fracture energy of vertical discrete cracks has a major impact on the predicted load-bearing capacity. The influence is slightly higher for the lower strength class than for the higher strength class.

- The strength profiles control the predicted load-bearing capacity of individual beams. It is clear that a more precise description of the tensile strength leads to an improved accuracy of the results.

Regarding future developments, a possible improvement would be to assign section-wise constant but varying fracture energies to vertical discrete cracks, derived from fracture simulations of knot groups with an appropriate phase field approach. Such concept are currently being intensively researched.

Bibliography

[1] Abaqus. *Documentation Version 2019 FD02 (FP.1914)*. Digital medium from software installation. Vélizy–Villacoublay, France: Dassault Systèmes Simulia Corp., 2019.

[2] G. Balduzzi, G. Kandler, and J. Füssl. "Estimation of GLT beam stiffness based on homogenized board mechanical properties and composite beam theroy". In: VI European Conference on Computational Mechanics (Glasgow, United Kingdom, June 11–15, 2018). 2018.

[3] T. Belytschko and T. Black. "Elastic crack growth in finite elements with minimal remeshing". In: *International Journal for Numerical Methods in Engineering* 45.5 (1999), pp. 601–620.

[4] D. A. Bender, F. E. Woeste, E. L. Schaffer, and C. M. Marx. *Reliability formulation for the strength and fire endurance of glued-laminated beams*. Res. Pap. FPL 460. Wisconsin, USA: US Department of Agriculture, Forest Service, Forest Products Laboratory, 1985.

[5] L. Blank, G. Fink, R. Jockwer, and A. Frangi. "Quasi-brittle fracture and size effect of glued laminated timber beams". In: *European Journal of Wood and Wood Products* 75.5 (2017), pp. 667–681.

[6] H. J. Blaß, M. Frese, P. Glos, J. K. Denzler, P. Linsenmann, and A. Ranta-Maunus. *Zuverlässigkeit von Fichten-Brettschichtholz mit modifiziertem Aufbau (German) [Reliability of spruce glulam with modified structure]*. Band 11 der Reihe Karlsruher Berichte zum Ingenieurholzbau. In German. Wisconsin, Germany: Lehrstuhl für Ingenieurholzbau und Baukonstruktionen, 1985.

[7] R. Brandner and G. Schickhofer. "Glued laminated timber in bending: new aspects concerning modelling". In: *Wood Science and Technology* 42.5 (2008), pp. 401–425.

[8] A. Briggert, A. Olsson, and J. Oscarsson. "Three-dimensional modelling of knots and pith location in Norway spruce boards using tracheid-effect scanning". In: *European Journal of Wood and Wood Products* 74.5 (2016), pp. 725–739.

[9] A. G. Burk and D. A. Bender. "Simulating finger-joint performance based on localized constituent lumber properties". In: *Forest Products Journal* 39.3 (1989), pp. 45–50.

[10] P. P. Camanho and C. G. Dávila. "Mixed-mode decohesion finite elements for the simulation of delamination in composit materials". In: *NASA/TM-2002–211737* (2002), pp. 1–37.

[11] F. Colling. "Tragfähigkeit von Biegeträgern aus Brettschichtholz in Abhängigkeit von den festigkeitsrelevanten Einflussgrößen (German) [Load-bearing capacity of bending beams made of glued laminated timber depending on the strength-relevant parameters]". In German. PhD thesis. Karlsruhe, Germany: Fakultät für Bauingenieur- und Vermessungswesen, Universität Karlsruhe, 1990.

[12] F. Colling, J. Ehlbeck, and R. Görlacher. "Glued laminated timber. Contribution to the determination of the bending strength of glulam beams". In: Proceedings of the International Council for Research and Innovation in Building and Construction (Oxford, United Kingdom, Sept. 7–9, 1991), CIB-W18/24-12–2.

[13] DIN 68364:2003-05. *Kennwerte von Holzarten - Rohdichte, Elastizitätsmodul und Festigkeiten (German) [Properties of wood species – Density, modulus of elasticity and strength].* Standard. In German. Berlin, Germany: DIN Deutsches Institut für Normung e. V., May 2003.

[14] DIN EN 14080:2013-09. *Holzbauwerke – Brettschichtholz und Balkenschichtholz – Anforderungen; Deutsche Fassung EN 14080:2013 (German) [Timber structures – Glued laminated timber and glued solid timber – Requirements; German version EN 14080:2013].* Standard. In German. Berlin, Germany: DIN Deutsches Institut für Normung e. V., Sept. 2013.

[15] DIN EN 338:2016-07. *Bauholz für tragende Zwecke – Festigkeitsklassen; Deutsche Fassung EN 338:2016 (German) [Structural timber - Strength classes; German version EN 338:2016].* Standard. In German. Berlin, Germany: DIN Deutsches Institut für Normung e. V., July 2016.

[16] DIN EN 408:2010-12. *Holzbauwerke – Bauholz für tragende Zwecke und Brettschichtholz – Bestimmung einiger physikalischer und mechanischer Eigenschaften;Deutsche Fassung EN 408:2010 (German) [Timber structures – Structural timber and glued laminated timber – Determination of some physical and mechanical properties; German version EN 408:2010].* Standard. In German. Berlin, Germany: DIN Deutsches Institut für Normung e. V., Dec. 2010.

[17] J. Ehlbeck, F. Colling, and R. Görlacher. "Einfluß keilgezinkter Lamellen auf die Biegefestigkeit von Brettschichtholzträgern. Teil 1: Entwicklung eines Rechenmodells (German) [Influence of finger-jointed lamellas on the bending strength of glulam beams. Part 1: Development of a computer model]". In: *Holz als Roh- und Werkstoff* 43.8 (1985). In German, pp. 333–337.

[18] J. Ehlbeck, F. Colling, and R. Görlacher. "Einfluß keilgezinkter Lamellen auf die Biegefestigkeit von Brettschichtholzträgern. Teil 2: Eingangsdaten für das Rechenmodell (German) [Influence of finger-jointed lamellas on the bending strength of glulam beams. Part 2: Input data for the computer model]". In: *Holz als Roh- und Werkstoff* 43.9 (1985). In German, pp. 369–373.

[19] J. Ehlbeck, F. Colling, and R. Görlacher. "Einfluß keilgezinkter Lamellen auf die Biegefestigkeit von Brettschichtholzträgern. Teil 3: Überprüfung des Rechenmodells mit Hilfe von Trägerversuchen (German) [Influence of finger-jointed lamellas on the bending strength of glulam beams. Part 3: Verification of the computer model by bending tests]". In: *Holz als Roh- und Werkstoff* 43.10 (1985). In German, pp. 439–442.

[20] R. H. Falk, K. H. Solli, and E. Aasheim. *The performance of glued laminated beams manufactured from machine stress graded norwegian spruce.* Meddelelse (Norwegian) [Announcement] 77. Oslo, Norway: Norsk Treteknisk Institutt, 1992.

[21] G. Fink. "Influence of varying material properties on the load-bearing capacity of glued laminated timber". PhD thesis. Zurich, Switzerland: Institute of Structural Engineering (IBK), ETH Zürich, 2014.

[22] G. Fink, A. Frangi, and J. Kohler. "Modelling the bending strength of glued laminated timber – considering the natural growth caracteristics of timber". In: Proceedings of the International Council for Research and Innovation in Building and Construction (Vancouver, Canada, Aug. 26–29, 2013), CIB-W18/46-12–1.

[23] G. Fink, J. Kohler, and A. Frangi. *Bending Tests on Glued Laminated Timber Beams with Well-Known Material Properties.* Bericht Nr. (German) [Report No.] 350. Zurich, Switzerland: IBK Institut für Baustatik und Konstruktion, ETH Zürich, 2013.

[24] C. Foley. "Modeling the effects of knots in structural timber". PhD thesis. Lund, Sweden: Division of Structural Engineering, Lund University, 2003.

[25] R. O. Foschi and J. D. Barrett. "Glued-laminated beam strength: a model". In: *Journal of the Structural Division, ASCE* 106.8 (1980), pp. 1735–1754.

[26] M. Frese. *Die Biegefestigkeit von Brettschichtholz aus Buche: Experimentelle und numerische Untersuchungen zum Laminierungseffekt (German) [The bending strength of beech glulam: Experimental and numerical investigations on the lamination effect].* PhD thesis. In German. Karlsruhe, Germany: Fakultät für Bauingenieur-, Geo- und Umweltwissenschaften, Universität Karlsruhe, 2006.

[27] M. Frese and H. J. Blaß. "Bending strength of spruce glulam". In: *European Journal of Wood and Wood Products* 67.3 (2009), pp. 277–286.

[28] M. Frese, F. Hunger, and H. J. Blaß. "Verifikation von Festigkeitsmodellen für die Brettschichtholz-Biegefestigkeit (German) [Validation of strength models for softwood glulam]". In: *European Journal of Wood and Wood Products* 68.1 (2010). In German, pp. 99–108.

[29] E. Gehri. "Determination of characteristic bending strength of glued laminated timber". In: Proceedings of the International Council for Research and Innovation in Building and Construction (Copenhagen, Denmark, Apr. 18–21, 1995), CIB-W18/28-12–1.

[30] E. Gehri. "Determination of characteristic bending values of glued laminated timber – EN-approach and reality". In: Proceedings of the International Council for Research and Innovation in Building and Construction (Åhus, Sweden, Aug. 24–27, 1992), CIB-W18/25-12–1.

[31] P. Glos. *Zur Bestimmung des Festigkeitsverhaltens von Brettschichtholz bei Druckbeanspruchung aus Werkstoff- und Einwirkungskenngrößen (German) [Determination of the strength behaviour of glued laminated timber under compressive stress from material and action parameters].* Berichte zur Zuverlässigkeitstheorie der Bauwerke (German) [Reports on the reliability theory of structures] 35. Munich, Germany: SFB 96, Technische Universität München, 1978.

[32] R. Görlacher. "Klassifizierung von Brettschichtholzlamellen durch Messung von Longitudinalschwingungen (German) [Classification of glulam lamellas by measuring longitudinal vibrations]". In German. PhD thesis. Karlsruhe, Germany: Fakultät für Bauingenieur- und Vermessungswesen, Universität Karlsruhe, 1990.

[33] C. Hackspiel, K. de Borst, and M. Lukacevic. "A numerical simulation tool for wood grading model development". In: *Wood Science and Technology* 48.3 (2014), pp. 633–649.

[34] R. Hernandez, D. A. Bender, and B. A. Richburg. "Probabilistic modeling of glued-laminated timber beams". In: *Wood and Fiber Science* 24.3 (1992), pp. 294–306.

[35] K. Hofstetter, C. Hellmich, and J. Eberhardsteiner. "Development and experimental validation of a continuum micromechanics model for the elasticity of wood". In: *European Journal of Mechanics – A/Solids* 24.6 (2005), pp. 1030–1053.

[36] C. Hu, C. Tanaka, and T. Ohtani. "On-line determination of the grain angle using ellipse analysis of the laser light scattering pattern image". In: *Journal of Wood Science* 50.569 (2004), pp. 321–326.

[37] G. Kandler, J. Füssl, E. Serrano, and J. Eberhardsteiner. "Effective stiffness prediction of GLT beams based on stiffness distributions of individual lamellas". In: *Wood Science and Technology* 49.6 (2015), pp. 1101–1121.

[38] G. Kandler, M. Lukacevic, and J. Füssl. "An algorithm for the geometric reconstruction of knots within timber boards based on fibre angle measurements". In: *Construction and Building Materials* 124 (2016), pp. 945–960.

[39] G. Kandler, M. Lukacevic, and J. Füssl. "Experimental study on glued laminated timber beams with well-known knot morphology". In: *European Journal of Wood and Wood Products* 76.5 (2018), pp. 1435–1452.

[40] G. Kandler, M. Lukacevic, and J. Füssl. "From the knot morphology of individual timber boards to the machanical properties of glued laminated timber". In: Proceedings of the 2016 World Conference on Timber Engineering (WCTE 2016) (Vienna, Austria, Aug. 22–25, 2016). 2016.

[41] G. Kandler, M. Lukacevic, C. Zechmeister, S. Wolff, and J. Füssl. "Stochastic engineering framework for timber structural elements and its application to glued laminated timber beams". In: *Construction and Building Materials* 190 (2018), pp. 573–592.

[42] R. Keylwerth. *Die anisotrope Elastizität des Holzes und der Lagenhölzer (German) [The anisotropic elastisity of timber and laminated wood].* VDI-Forschungsheft 430. In German. Düsseldorf, Germany: Deutscher Ingenieur-Verlag, 1951.

[43] D. Kline, F. Woeste, and B. Bendtsen. "Stochastic model for modulus of elasticity of lumber". In: *Wood and Fiber Science* 18.2 (1986), pp. 228–238.

[44] F. Kollmann. *Technologie des Holzes und der Holzwerkstoffe (German) [Technology of timber and wood products].* In German. Springer-Verlag Berlin Heidelberg, 1982.

[45] M. Lukacevic. "Numerical simulation of wooden boards considering morphological characteristics and complex failure processes". PhD thesis. Vienna, Austria: Fakultät für Bauingenieurwesen, Technische Universität Wien, 2014.

[46] M. Lukacevic. "Validation and optimization of a numerical simulation tool for wood grading". mastersthesis. Vienna, Austria: Fakultät für Bauingenieurwesen, Technische Universität Wien, 2009.

[47] M. Lukacevic and J. Füssl. "Numerical simulation tool for wooden boards with a physically based approach to identify structural failure". In: *European Journal of Wood and Wood Products* 72.4 (2014), pp. 497–508.

[48] M. Lukacevic, J. Füssl, and J. Eberhardsteiner. "Discussion of common and new indicating properties for the strength grading of wooden boards". In: *Wood Science and Technology* 49.3 (2015), pp. 551–576.

[49] M. Lukacevic, G. Kandler, M. Hu, A. Olsson, and J. Füssl. "A 3D model for knots and related fiber deviations in sawn timber for prediction of mechanical properties of boards". In: *Materials and Design* 166 (2019), pp. 1–18.

[50] H. A. Mang and G. Hofstetter. *Festigkeitslehre (German) [Strength of materials].* 5th ed. In German. Springer Vieweg, 2018.

[51] J. M. Melenk and I. Babuška. *The partition of unity finite element method basic theory and applications.* Research Report No. 96-01. Zurich, Switzerland: SAM Seminar für Angewandte Mathematik, ETH Zürich, 1996.

[52]   J. Nyström. "Automatic measurement of fiber orientation in softwoods by using the tracheid effect". In: *Computers and Electronics in Agriculture* 41.1–3 (2003), pp. 91–99.

[53]   A. Olsson and J. Oscarsson. "Three dimensional fibre orientation models for wood based on laser scanning utilizing the tracheid effect". In: Proceedings of the 2014 World Conference on Timber Engineering (WCTE 2014) (Quebec City, Canada, Aug. 10–14, 2014). 2014.

[54]   H. Riberholt, J. Ehlbeck, and A. Fewell. "Glued laminated timber – strength classes and determination of characteristic properties". In: Proceedings of the International Council for Research and Innovation in Building and Construction (Lisbon, Portugal, Sept. 10–14, 1990), CIB-W18A/23-12–4.

[55]   G. Schickhofer. "From the knot morphology of individual timber boards to the machanical properties of glued laminated timber". In: Proceedings of the International Council for Research and Innovation in Building and Construction (Bordeaux, France, Aug. 26–29, 1996). 1996, CIB-W18/29-12–1.

[56]   E. Serrano. *Finger-joints for laminated beams. Experimental and numerical studies of mechanical behavior.* Report TVSM-3021. Lund, Sweden: Division of Structural Mechanics, Lund University, 1997.

[57]   E. Serrano and P. J. Gustafsson. "Fracture mechanics in timber engineering – Strength analyses of components and joints". In: *Materials and Structures* 40.1 (2015), pp. 87–96.

[58]   J.-H. Song, M. A. A. Pedro, and T. Belytschko. "A method for dynamic crack and shear band propagation with phantom nodes". In: *International Journal for Numerical Methods in Engineering* 67.6 (2006), pp. 868–893.

[59]   G. Stapf. "Energiedissipationsfähigkeit und Ermüdungsverhalten von geklebten Holzverbindungen (German) [Energy dissipation capacity and fatigue behavior of glued wood joints]". In German. Diploma thesis. Kassel, Germany: Fachgebiet Holzbau, Universität Kassel, 2010.

[60]   C. Tapia Camú and S. Aicher. "A stochastic finite element model for glulam beams of hardwoods". In: Proceedings of the 2018 World Conference on Timber Engineering (WCTE 2018) (Seoul, Republic of Korea, Aug. 20–23, 2018). 2018.

[61]   S. E. Taylor and D. A. Bender. "Stochastic model for localized tensile strength and modulus of elasticity in lumber". In: *Wood and Fiber Science* 23.4 (1991), pp. 501–519.

[62]   G. Ventura and E. Benvenuti. "Equivalent polynomials for quadrature in Heaviside function enriched elements". In: *International Journal for Numerical Methods in Engineering* 102.3–4 (2015), pp. 688–710.

[63]   W. Weibull. *A statistical theory of the strength of materials.* Handlingar Nr. (Swedish) [Report No.] 151. Stockholm, Sweden: Ingeniörsvetenskapsakademiens, Generalstabens litografiska anstalts förlag, 1939.

[64]   H. Werkle. *Finite Elemente in der Baustatik (German) [Finite elements in structural analysis].* Vieweg+Teubner Verlag, 2008.

[65]   J. Zhou and J. Shen. "Ellipse detection and phase demodulation for wood grain orientation measurement based on the tracheid effect". In: *Optics and Lasers in Engineering* 39.1 (2003), pp. 73–89.